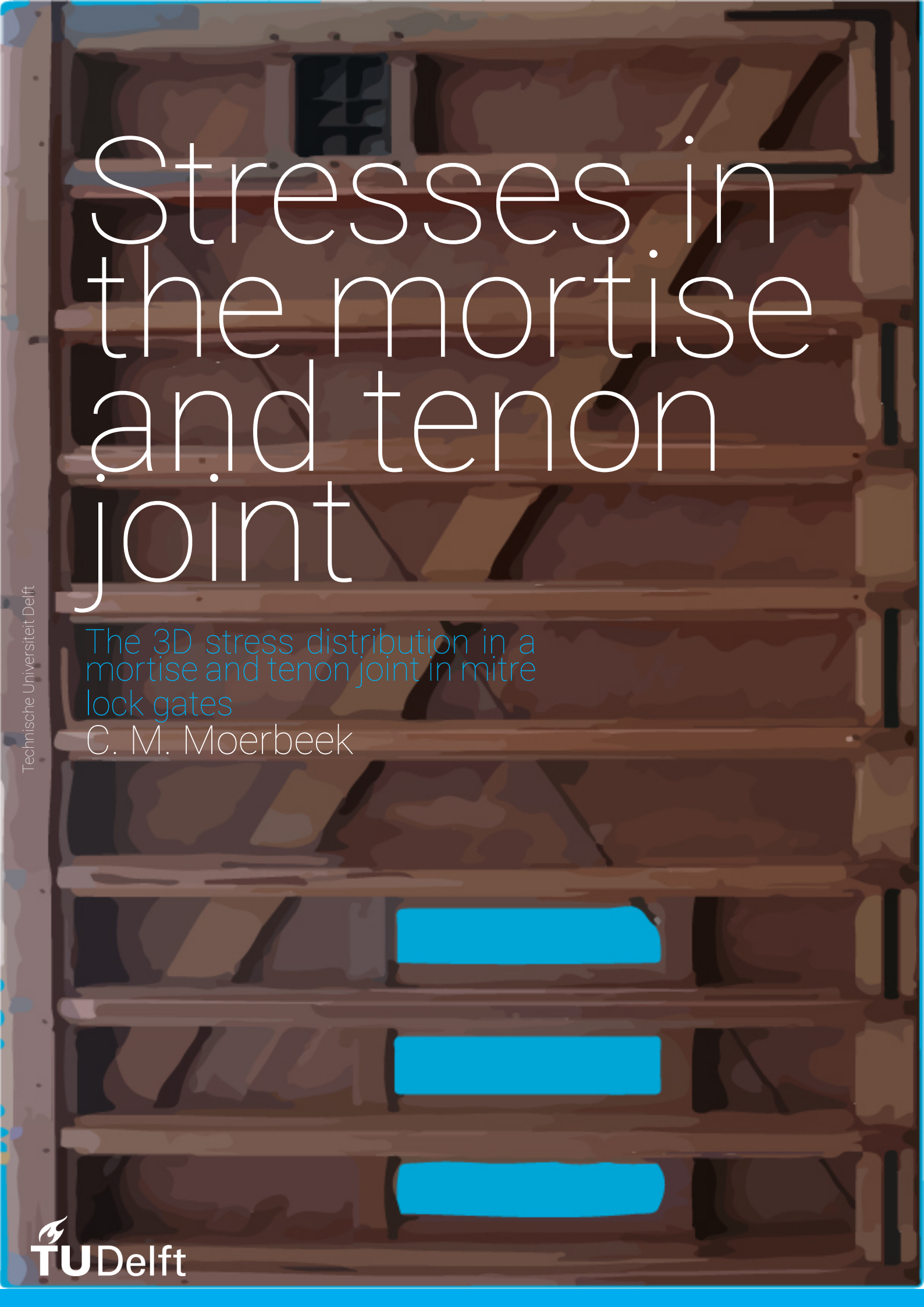

Stresses in the mortise and tenon joint

The 3D stress distribution in a mortise and tenon joint in mitre lock gates

C. M. Moerbeek

Technische Universiteit Delft

TU Delft

Stresses in the mortise and tenon joint

The 3D stress distribution in a mortise and tenon joint in mitre lock gates

by

C. M. Moerbeek

to obtain the degree of Master of Science
at the Delft University of Technology,
to be defended publicly on 3 July 2017.

Student number:	1504657	
Project duration:	March, 2016 – July, 2017	
Thesis committee:	Prof. dr. ir. J. W. G. van de Kuilen,	TU Delft, Civil Engineering and Geosiences, SBE supervisor
	Dr. ir. G. J. P. Ravenshorst,	TU Delft Civil Engineering and Geosiences, SBE
	Dr. ir. M. A. N. Hendriks,	TU Delft Civil Engineering and Geosiences, SM

TU Delft

Preface

This report is written as the concluding piece of my Master Civil Engineering at the University of Technology in Delft. In this master thesis "Stresses in the mortise and tenon joint" joints of a timber lock gate are studied. This study is done by using a 3D computer model and a theoretical derivation for a theory on tenon beams. Previous tests are used in this report to test, the derived theory against existing lab results. The cause for this report is, that construction companies are not able to verify the mortise and tenon joints that are used.

My interest in old constructions, is combined with the use of technology to find out how the construction works. I found it remarkable to see, that the working of a seemingly simple geometric connection is still unknown. While in the mean time this connection is widely used and likely safe. I liked expending the knowledge of this connection in this research and explaining why this connection is safe, even without completely understanding this connection.

In doing this research and writing this report I had help from many people whom I like to thank. At first I like to thank my thesis committee for the support during my research. It was always possible to visit and discus the difficulties I encountered during my research. I would like to thank Wijma Kampen B.V. for the possibility to ask them questions about the different facets of lock gate building. I like to thank Per-Johan Gustafsson of the University of Lunds for helping me to understand his study in the strength of notched beams Gustafsson (1988). At last I like to thank my friends and family for their support and help during my research.

I would like to end with a poem about the remarkable product. This mathematical operation was used in obtaining the value for the compliance spring stiffness of the notch. Finding out how this spring stiffness was found costed me lot of effort, while this mathematical operation is well known. The remarkable product that is used in this thesis is: $A(\beta d+B)^3 = A\left((\beta d)^3 + 3B(\beta d)^2 + 3B^2(\beta d) + B^3\right)$.

A plus B

The bells of the tower,
sounded for an hour,
they ringed abundant, because A married B.
It was her ex-lovers fate
that they were a bit late.
It's hard to swallow, especially for C.

A and B all alone
possessed of each others moan,
in that night it all happened A plus B squared.
Cheerfully, time passed soon
during the honeymoon
a baby saw the light. When the bed was shared.

The couple watched and thought,
'Whose looks dose ours child got?'
'Look, at A-squared! Yes, she has got it from me.'
'Take a look at the bent,
that is your B descent
and then two-A-B from both of use, see.'

Prosperous times passed by,
but they both seem quite shy,
they were extremely offended and dismayed.
Because C walked along,
looked at the kid and song
'What a remarkable product did you made!'.

English translation by me of "A plus B" by Drs. P & Marjolein Kool (2000:135) .

C. M. Moerbeek
Delft, July 2017

Symbol list

The symbol list contains frequently used symbols in this thesis.

A	Area of the cross section of the beam
A_1	Area of the cross section 1 of the beam
A_2	Area of the cross section 2 of the beam
A_3	Area of the cross section 3 of the beam
$C_{e,t}$	Bending displacement notch to tenon transformation factor
$C_{r,t}$	Rotation displacement notch to tenon transformation factor
$C_{v,t}$	Shear displacement notch to tenon transformation factor
E	Modulus of elasticity
E_x	Modulus of elasticity in the x direction
F	Force
$F_{ax,Rk}$	Characteristic withdrawal capacity of the bolt
F_d	Force in the chest
F_{di}	Force in the inside chest
F_{do}	Force in the outside chest
F_f	Share force at the inside and outside chest
F_{fb}	Friction force between mortise and tenon bottom
F_h	Tension force at the back of the mortise
F_r	Clamping force in the tenon
F_{ten}	Force in the tenon
$F_{v,Rk}$	Characteristic strength of the bolted joint
G_c	Fracture energy
$G_{f,x}$	Fracture energy in pure tensile splitting parallel to the fibre
$G_{f,y}$	Fracture energy in pure tensile splitting perpendicular to the fibre
G	Shear modulus
G_{xy}	Shear modulus in the xy direction
H_a	Horizontal force at support A
H_c	Horizontal force at support C
I	The second moment of areas
I_1	The second moment of area 1 of the beam
I_2	The second moment of area 2 of the beam
I_3	The second moment of area 3 of the beam
K	Material factor dependent on multiple material properties
L	Length of the beam
M	Moment
M_{max}	Maximum moment in the mitre gate
M_{ten}	Moment in the tenon
M_{th}	Moment at the heel joint
M_{tm}	Moment at the mitre joint
$M_{y,Rk}$	Characteristic fastener yield moment
S_c	Diagonal support force at support C
V	Shear force
V_c	Vertical force at support C
V_b	Vertical force at support B
V_f	Shear force
W_P	Potential energy

a	Distance between two points
b	With of the beam
c	Compliance spring stiffness
d	Height of the beam
d	Bolt diameter
$f_{c,0,d}$	Design compression strength parallel to the fibre
$f_{c,90,d}$	Design compression strength perpendicular to the fibre
$f_{h,d}$	Characteristic embedment strength
$f_{m,d}$	Design bending strength
$f_{t,0,d}$	Design tension strength parallel to the fibre
$f_{t,90,d}$	Design tension strength perpendicular to the fibre
$f_{u,k}$	Characteristic tensile strength
f_v	Shear strength
$f_{v,d}$	Design shear strength
$f_{v,k}$	Characteristic shear strength
$f_{v,r,d}$	Characteristic rolling shear strength
h	Height of the beam
h_e	Height of the tenon or notch
i	Inclination of the notch
k	Scale factor
k_{mod}	Modification factor for duration of load and moisture content
k_n	Solid timber factor
k_v	Reduction factor
l_{ef}	Effective length
t	Thickness
u	Displacement
ur	Rotation displacement
v	Displacement
x	Distance from line of action of the support reaction to the corner of the notch

α	Tenon or notch height factor
α_1	Tenon height factor
α_2	Tenon location factor
α_g	Angle of the mortise gate
β	Support cantilever length factor
γ	Top tenon length factor
γ_m	Partial factor for material properties, also accounting for model uncertainties and dimensional variations
δ	Deflection of the beam at the load
δ_e	Deflection of the beam at the load due to bending
δ_l	Deflection of the beam at the load due to local deformation
δ_r	Deflection of the beam at the load due to rotation
δ_t	Total deflection of the beam at the load
δ_v	Deflection of the beam at the load due to shear
μ	Friction coefficient
υ	Poison ration
π	Mathematical constant of the circle's circumference
ρ	Density of the material
σ_c	Acting compression stress
σ_t	Acting tension stress
τ_d	Acting shear stress
φ	Rotation
ω	Moisture content

Summary

Cause for the research

Many locks are used in the Netherlands to control water levels. Locks contain timber gates to maintain the water levels. A mitre lock gate contains two lock gates assembled in a point. This type of lock gates have been constructed for centuries. These days the gates needs to comply with the prescribed verification methods. The existing verification method calculates whether the gate is safe or might fail. The mortise and tenon joint in the gate, are according the verification method not safe. However this connection in the gate is used for centuries, without there ever having been a recorded failure. So this is in conflict with the verification method.

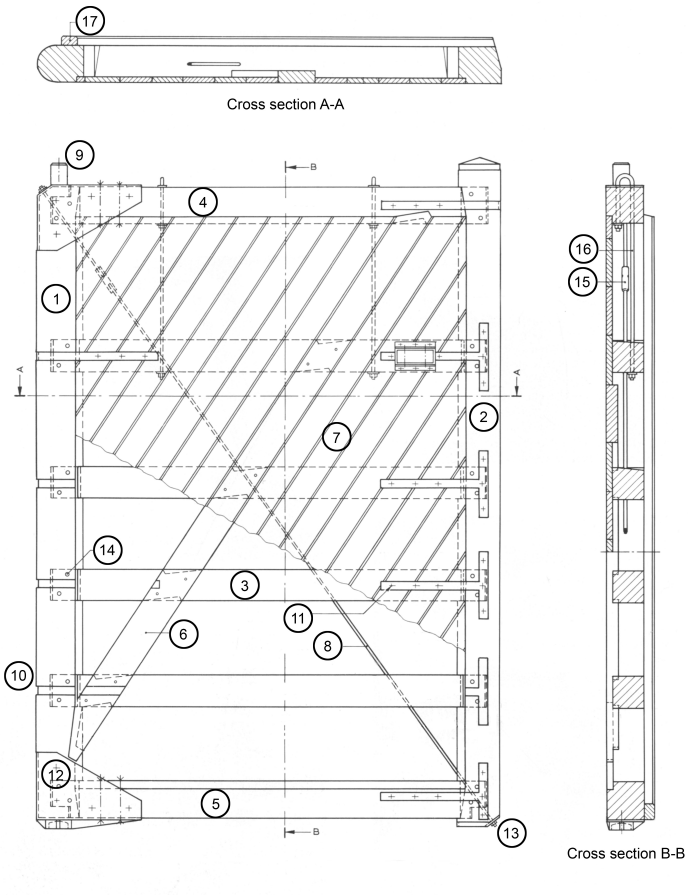

Figure 1: Drawing of a mitre lock gate (edited form [25], fig. 63.1)

A mitre gate works trough the diagonal sheathing (7), that transfer the load to the girders (3) by bending. The girders will carry the forces to the post (1 and 2) by bending. The heel post (1) will transfer the shear force via the seal strip (17) to the lock. The mitre post (2) will transfer the shear force to the other gate, as a normal force. Due to the angle of the mitre gate, a normal force develops in the gate. This normal force is transferred via the girders to the heel post. The heel post transfers the normal force to the embedment in the lock. The complete detailed understanding of the mortise and tenon joint shown in figure 2 remains unknown. The contact stress distribution due to water pressure, between the tenon and mortise is unknown. This contact stress distribution, is likely to differ between the mortise and tenon joints due to the geometrical and support differences

The verification method is written in paragraph 6.5.2 in the Eurocode 5 (NEN-EN 1995-1-1, 2005). This is the reduced shear stress in a notch beam. This is calculated according equation 1 with equation 2 with $k_n = 5$ for solid timber, i is zero because there is a straight corner with $a = \frac{h_e}{h}$. Where h_e is the height of the tenon and h is the height of the beam as

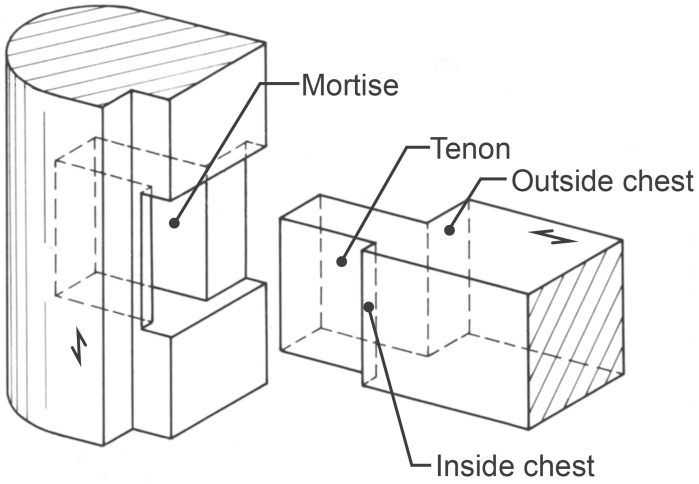

Figure 2: Inside view of the mortise and tenon joint (edited from [25], fig. 63.16)

shown in figure 3.

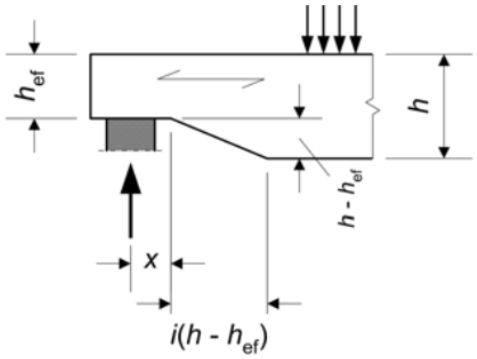

Figure 3: End-notched beam (obtained from [3], fig. 6.11 a)

$$\tau_d = \frac{1,5V}{bh_e} \leq k_v f_{v,k} \frac{k_{mod}}{\gamma_m} = k_v f_{v,d} \tag{1}$$

$$k_v = min \begin{cases} 1,0 \\ \dfrac{k_n\left(1+\frac{1,1i^{1,5}}{\sqrt{h}}\right)}{\sqrt{h}\left(\sqrt{\alpha(1-\alpha)}+0,8\frac{x}{h}\sqrt{\frac{1}{\alpha}+\alpha^2}\right)} \end{cases} \tag{2}$$

According this verification method the mortise and tenon joint are not safe. This implies that the construction company needs to adjust the connection to a connection that is safe according the verification method.

Research method

The goal of this thesis is to obtain a greater knowledge in the stresses in the mortise and tenon joint, for a hardwood mitre gate. Also the strength of the tenon is important in the verification of the mortise and tenon joint. In this thesis the knowledge of a tenon beam is theoretical explained. The main question of this thesis is:

- How is the water pressure on a closed mitre gate, transferred to the supports and how can this be verified?

In this thesis previous studies are studied for the design and constructing method of mitre gates. Previous studies are also used for studding the background of the verifications in the Eurocode 5. A finite element model is used to study the stress distribution in the joint. An analytical derivation is done on tenon beams. This derivation is compared with tests done on different tenon geometries, to obtain a possible theoretical tenon strength.

Results of the research

The main question is split in two parts. Part one is the contact stress distribution in the mortise and tenon joint and tension stresses perpendicular to the fibre. The second part is the theoretical strength of the tenon beam subjected to a point load.

Stress distribution

There are two kind of contact stresses. The friction stress and the contact pressure. Friction stress is only present when there is a contact pressure. The result is that the friction stresses locations are dependent on the locations of the contact pressures.

The normal stress in the girder is highly dependant on the angle of the gate. With a small angle the normal stress is big, while with a big angle the normal stress is small. Almost all of the normal stress is transferred via the outside chest. The normal stress also varies over the width of the girder. The sides of the girder are subjected to the biggest normal stress.

The shear stress in the tenon is transferred according three different mechanisms:

- Seal strip support
- Clamping of the tenon in the mortise.
- 3D effect, the transfer via the sides of the mortise.

The seal strip support in the heel joint carries a part of the shear stress. This stress is evenly distributed over the width of the tenon. Clamping occurs in the heel joint and in the mitre joint when the gate is used at a big angle. The clamping results in a pressure distribution on the top end the tenon as shown in figure 4. The 3D effect is present in both the heel and mitre joint. The stress distribution varies over the width of the tenon. The sides of the tenon will be subjected to higher stresses than the middle of the tenon. Combining these results show that the contact pressure distribution is biggest at the edge corners of the mortise and tenon shown in figure 4 and 5.

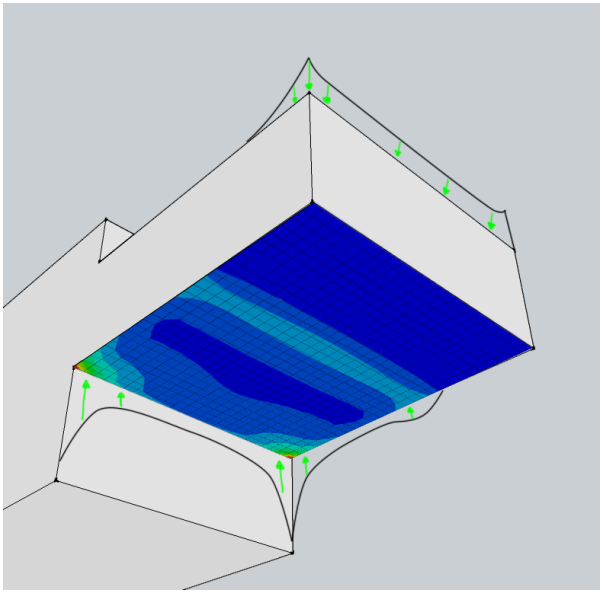

Figure 4: Contact pressure at the tenon at the heel post

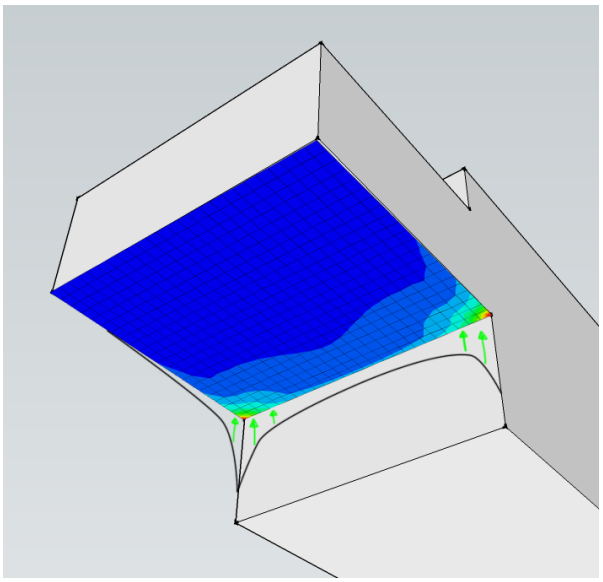

Figure 5: Contact pressure at the tenon at the mitre post

The contact pressures on the top and the bottom of the tenon, results in stresses perpendicular to the grain. The tension stresses perpendicular to the grain are imported because the low strength in this direction. Highly localized tension stresses are present at the corners and this coincides with the high contact pressure in figure 4 and 5. These local tension stresses spread out along the length of the post next to the mortise shown in figure 2. The stresses in this areas are

of greater importance than the highly local stresses, because of the large area it is acting on. Conclusions regarding the stress distribution are present at the end of the summary.

Theoretical strength of the tenon beam

The verification method for the reduced shear force for notched beams is equation 1 with equation 2. The notched beam expression is used for a tenon beam using an assumption of Ehlbeck and Krommer (1996) this assumption assumes a notch equivalent of a tenon beam shown in figure 6. Some material properties for softwoods are already included in this verification method. This makes this verification method not suitable for hardwoods. The basis of this method is derived from the theoretical notched beam expression obtained by Gustafsson (1988).

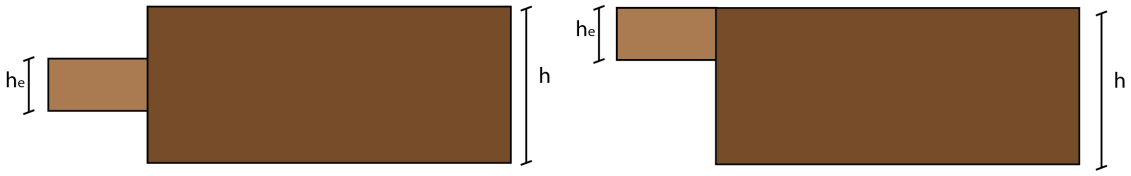

Figure 6: Ehlbeck and Kromer (1995) [9] assumption for notch to tenon beams. The real configuration (left). The assumed equivalent (right)

The expression of Gustafsson (1988) is obtained using the deflection of the notch. This deflection is a summation of the bending and shear displacement with the displacement of a fictional rotational spring at the notch beam interface. The fictional spring is used, because tests shown that including an extra displacement resulted in better results. This fictional rotational spring stiffness is calculated mathematical to obtain a simpler expression. The expression of Gustafsson (1988) is equation 3 that includes the mathematical obtained spring stiffness with the equation $c = \frac{12}{b\alpha^2 d^2}\sqrt{\frac{(1-\alpha)(1-\alpha^3)}{10G_{xy}E_x}}$ $[1/Nm]$.

$$\frac{V_f}{b\alpha d} = \frac{\sqrt{\frac{G_{f,y}}{d}}}{\sqrt{\frac{0{,}6(\alpha-\alpha^2)}{G_{xy}}} + \beta\sqrt{\frac{6\left(\frac{1}{\alpha}-\alpha^2\right)}{E_x}}} \tag{3}$$

where V_f $[N]$ is the shear force, $G_{f,y}$ $[N/mm]$ is the fracture energy in pure tensile splitting perpendicular to the fibre, G_{xy} $[N/mm^2]$ is he shear modulus, E_x $[N/mm^2]$ is the modulus of elasticity parallel to the grain b $[mm]$ is the width of the beam and d $[mm]$ the height of the beam. α $[-]$ and β $[-]$ are shown in figure 7.

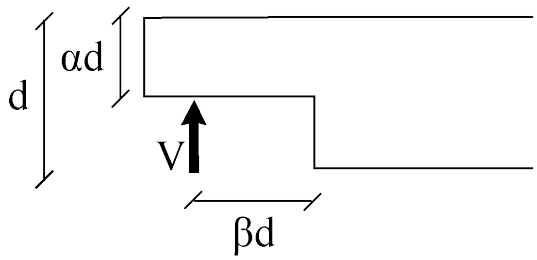

Figure 7: Geometric properties of a notch beam

The method of Gustafsson (1988) is used to obtain a theoretical tenon strength. In the case of the tenon beam two different strength equations are found. Equation 4 is obtained using the bending and the shear displacement and a fictional rotational spring flowing equation 5. that is mathematically obtained for a simpler equation (TTS). While equation 6 is obtained using only the bending and the shear displacement (TTS $c = 0$).

The fracture energy of hardwood is unknown. The expression for the fracture energy of hardwood is modelled using test data, this is obtained by Van Otterloo (2013). The fracture energy for hardwood follows from equation 7.

The expression of Gustafsson (1988), TTS and TTS $c = 0$ are compared with test results from different tenon geometries. The conclusions from these comparisons are in the final part of this summary.

Conclusions and recommendations

The conclusions regarding the mortise and tenon joint, in hardwood mitre lock gates are:

- Almost half of the shear force due to the water pressure is transferred to the heel post and the other half trough mitre post. The biggest part of the shear force is transferred via contact pressure in the tenon. This shear force is transferred via three mechanisms: the seal strip support, the clamping of the tenon in the mortise and the 3D effect (the transfer via the sides of the mortise). In the heel joint are all three mechanisms present. In the mitre joint is the 3D effect present and clamping when the gate is used at a big angle.
- The three transfer mechanisms spread the shear force over a bigger area than the existing calculations assumed. This results in lower contact stresses.
- The stresses found in the model do not exceed the ultimate assumed strength.

The conclusions regarding the contact stress and the tension stress perpendicular to the fibre are:

- Friction stress is present but has a small contribution in the stress transfer.
- The normal contact pressure is, for the biggest part transferred via the outside chests.
- The normal contact pressure is unevenly distributed along the height and width of the outside chest. The contact pressure is the highest at the edges of the chest.
- The tension stresses perpendicular to the fibre, from big to small are: at the mortise side in the mitre joint, at the mortise side in the heel joint, at the tenon pit at the mitre side and at the tenon pit at the heel side. They do not not exceed the ultimate assumed strength.
- Due to the different geometries and supports is the stress distributions different between the heel and mitre joint.

The conclusions on the notch and tenon beam from this thesis are:

- The reduced shear stress method in paragraph 6.5.2 of Eurocode 5 (2005) is not suitable for tenon beams.
- This method is based on the theoretic notch strength found by Gustafsson (1988) that is derived trough bending and shear displacement and displacement from a fictional spring stiffness $c = \frac{12}{b\alpha^2 d^2}\sqrt{\frac{(1-\alpha)(1-\alpha^3)}{10G_{xy}E_x}}$ $[1/Nm]$ of the notch beam.
- Two theoretic tenon strength equations are found. The first one with a mathematical obtained c equation 5 this is equation 4 (TTS). The second one with $c = 0$ this is equation 6 (TTS $c = 0$)

$$\begin{aligned} \frac{V_f}{b\alpha_1 d} &= \frac{\sqrt{\frac{G_{f,y}}{d}}}{\sqrt{\frac{0{,}6C_{v,t}\left(\alpha_1-\alpha_1^2\right)}{G_{xy}}}+\beta\sqrt{\frac{6C_{e,t}\left(\frac{1}{\alpha_1}-\alpha_1^2\right)}{E_x}}} \\ C_{v,t} &= \frac{(\alpha_1+\alpha_2-1)\alpha_1}{(\alpha_1+\alpha_2)(\alpha_1-1)} \\ C_{e,t} &= \frac{\left((\alpha_1+\alpha_2)^3-1\right)\alpha_1^3}{(\alpha_1+\alpha_2)^3\left(\alpha_1^3-1\right)} \end{aligned} \tag{4}$$

$$c = \frac{12}{b\alpha^2 d^2}\sqrt{C_{v,t}C_{e,t}}\sqrt{\frac{(1-\alpha_1)\left(1-\alpha_1^3\right)}{10G_{xy}E_x}} \tag{5}$$

$$\begin{aligned} \frac{V_f}{b\alpha_1 d} &= \sqrt{\frac{5G_{f,y}}{3d\left(\frac{C_{v,t}\left(\alpha_1-\alpha_1^2\right)}{G_{xy}}+10\beta^2\frac{C_{e,t}\left(1/\alpha_1-\alpha_1^2\right)}{E_x}\right)}} \\ C_{v,t} &= \frac{(\alpha_1+\alpha_2-1)\alpha_1}{(\alpha_1+\alpha_2)(\alpha_1-1)} \\ C_{e,t} &= \frac{\left((\alpha_1+\alpha_2)^3-1\right)\alpha_1^3}{(\alpha_1+\alpha_2)^3\left(\alpha_1^3-1\right)} \end{aligned} \tag{6}$$

where V_f $[m]$ is the shear force, $G_{f,y}$ $[N/mm]$ is the fracture energy in pure tensile splitting perpendicular to the fibre, G_{xy} $[N/m^2]$ is he shear modulus, E_x $[N/m^2]$ is the modulus of elasticity parallel to the grain b $[m]$ is the width of the beam and d $[m]$ the height of the beam. α_1 $[-]$, α_2 $[-]$ and β $[-]$ are shown in figure 8.

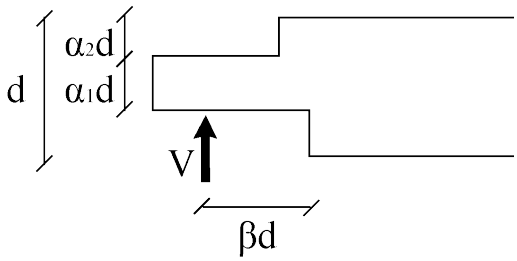

Figure 8: Geometric properties of a tenon beam

- The used fracture energy of hardwood equation 7 is obtain by van Otterloo (2013). This is an improvement over the equation used for softwood.

$$G_{f,y} = 5.36 \cdot 10^{-4} \rho + 4.15 \cdot 10^{-5} E_x \tag{7}$$

  with ρ $[kg/m^3]$ and E_x $[N/mm^2]$ both obtained for individual test specimen.

- TTS equation 4 corresponds the best with a tenon beam, where $\alpha_1 = \alpha_2 = 1/3$. TTS $c = 0$ equation 6 corresponds the best with an tenon beam where $\alpha_1 = 2/5$ and $\alpha_2 = 1/5$.

The recommendations for further research are:

- In the Eurocode 5 should be added that the existing equation for the reduced shear strength for a notched beams is only valid for softwood. This equation should be expanded to include hardwood notched beams.
- A bigger understanding of the material is needed. Important material properties are unknown. More specific material tests will lead to more knowledge of this material.
- Large scale tests on the strength of softwood and hardwood notch and tenon beams should be performed. The tests in this thesis are small scale tests that can only be used as an indication of the strength. Final conclusions regarding the strength can only be made after large scale tests.
- A study in the transition conditions, between the beam and notch or tenon interface will be valuable. To research the existing c value's.
- A finite element model that includes the behaviour of all the connection methods with the real support conditions will probably result in a more realistic stress distribution between the mortise and tenon joint.
- A more realistic material model with the possibility of cracking and using plasticity, can be used for research on possible failure mechanisms.
- Different load cases and parametric research can be used to gain more knowledge on the stress distribution and the influence of differed parameters.

Contents

1

Introduction

Many waterways in the Netherlands have different water levels. To control the water difference and to keep the waterways navigable, locks are built. Lock building in the Netherlands is done since the Middle Ages.

Drawings and pictures of the type of lock gate that is used in this thesis are shown in figure 1.1. The locks in figure 1.1 contains eight gates. The point shape of two lock gates make it a mitre lock gate. The point of the mitre gate points toward the front where the water level is the highest. The mitre gate at the back in the "Monstersche Sluis" points in the different direction. This to maintain the water level when it drops at the front of the lock. This type of lock is called an pond lock because the water between the two pair of gates acts as a pond where the height of the water is variable.

A mitre lock gate is build with a timber framework, covert with diagonal timber sheeting. The horizontal beams of the framework are connected via a mortise and tenon joint to the vertical post. The mortise and tenon joint in a mitre lock gate contains several timber and steel connection elements in one joint.

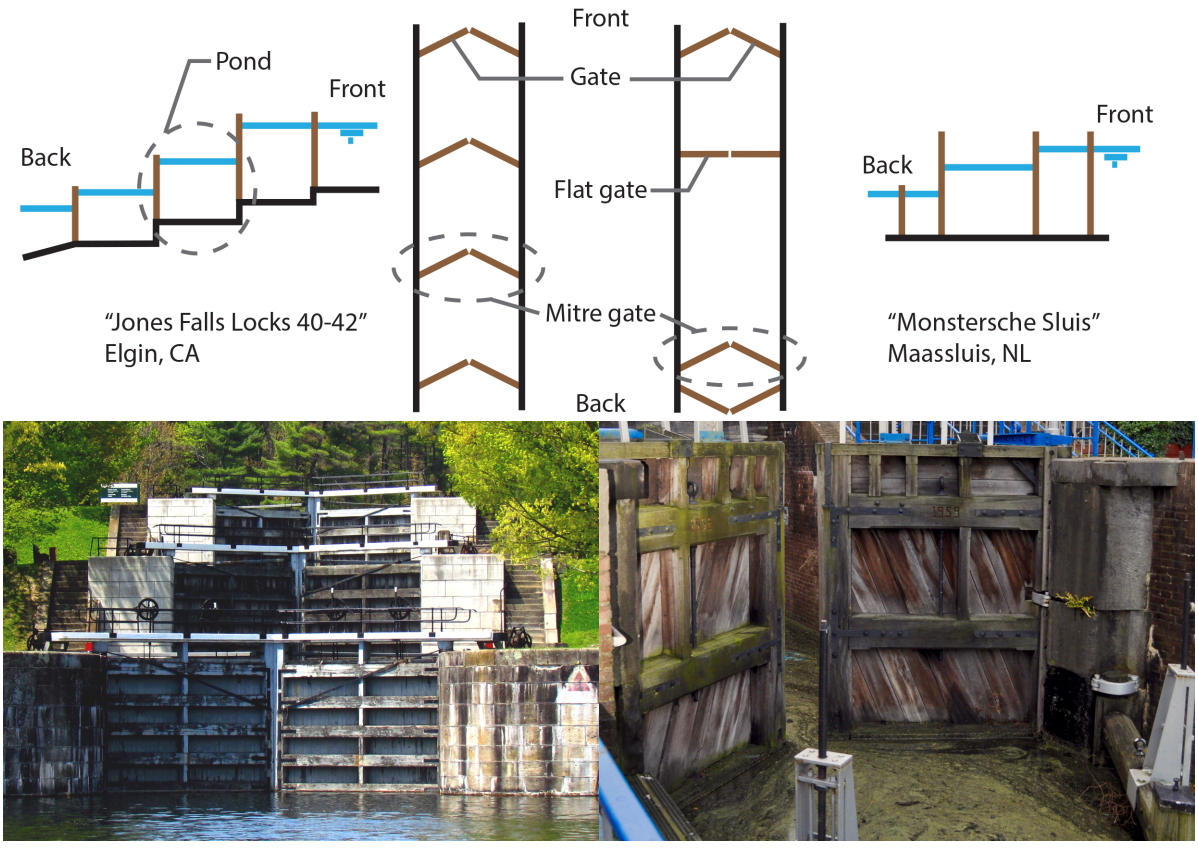

Figure 1.1: Mitre gate in use, "Jones Falls Locks" [1] (left) and "Monstersche Sluis" (right) with the drawn the top and side views.

1.1. Problem definition

Hardwood mitre gates are still in useful today, they can be used for decades with the low maintenance cost in comparisons with lock gates of other materials. The gate design is based on years of practical experiences. Today some of the traditional hand craft building methods are replaced by modern day fabrication techniques.

The hardwood mitre gates need to comply with the requirements in the Eurocode. The traditional designed gates would fail according the prescribed verification method, but in practice this failures has not been experienced. The problematic areas according the Eurocode are the mortise and tenon joints (mt joints) shown in figure 1.2. The calculations according the Eurocode 5 show, that the strength for the joint is not sufficient strong enough. This means that according de EC 5 the mt joint design is not valid. This implies that maybe the EC 5 calculation is not accurate for the mt joint.

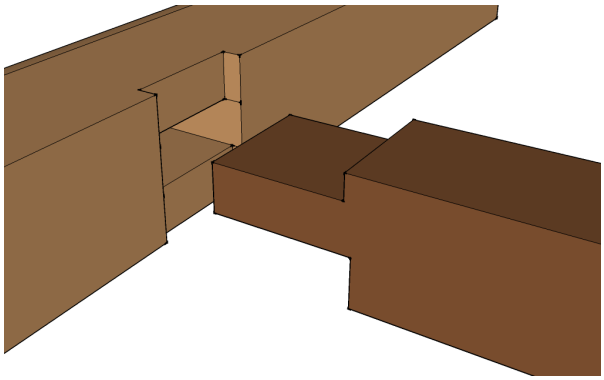

Figure 1.2: 3D drawing of the mortise and tenon joint in a lock gate

There is a differences between the heel and mitre joints shown in figure 1.3, how will this influence the strength is unknown. The mt joint contains different connections methods shown in figure 1.3 the bolted steel parts (red), the timber peg (yellow), the timber mortise and tenon (light brown and dark brown) joint. How these different connections methods work together and how they influence the strength of the total joint is unknown. The stresses acting on the connections needs to be know for verification according the EC 5. How the stress acts in the gate, remains unknown this makes it hard to do a validation. The theoretic strength of the hardwood mt joints remains unknown. As a result of this, it is not known how safe de mitre gates are.

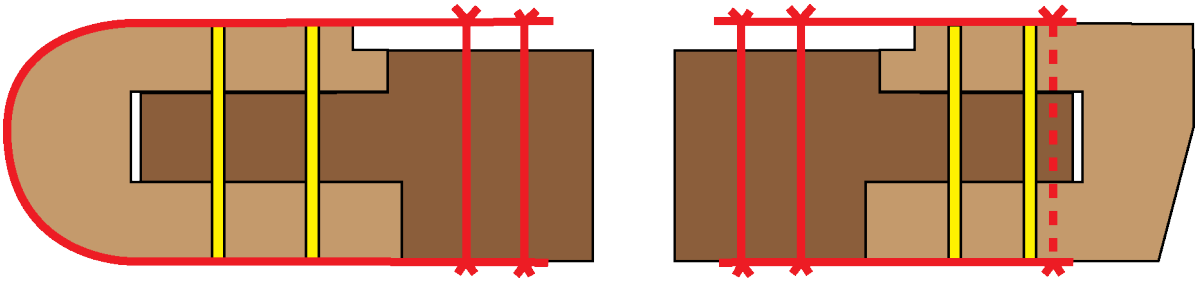

Figure 1.3: Cross section of the heel joint (left), cross section of the mitre joint (right)

The geometries of the connection are changed in practice to fulfill the existing requirements of the Eurocode 5. This change is posibly not necessary, because the actual strength of the joint is maybe safe. In previous studies Vermeij (2011) and van Otterloo (2013) stated that the problem is that the prescribed calculation methode in the Eurocode 5 for the notched beam is not suitable for the mt joints. Van Otterloo (2013) used a elastic 2D finite element model (FEM) to find the stress distribution in the joint. This thesis will continue to get a greater understanding of the hardwood mt joint.

An elastic 3D model of the timber part of the mt joint is modelled and then calculated with a final element method (FEM). The results from the FEM models will be studied an compared with the research from van Otterloo (2013) . This will result in more knowledge of the stress distribution in the joint. An analytical study is done on the tenon beam strength, to obtain the mechanical differences with a notch beam. Both Vermeij (2011) and van Otterloo (2013) did tests on tenon beams, they are used to test this analytical study.

The goal of this thesis is to get a better understanding in the stresses in the mt joint. The mt joint is split in the three different connections methods with the main focus on the timber joint part. The timber part is studied with a FEM model and an analytical study on the tenon beam strength. Table 1.1 shows previous studies and shows how they relate to this thesis. The method is written down in italic.

Table 1.1: Overview of previous studies

	Notch strength	**Tenon strength**	**Mortise and tenon joint strength**
Finite element method		Van Otterloo (2013)	Van Otterloo (2013) *2D model* Moerbeek (2017) *3D model*
Theoretic theory	Gustafsson (1988) *2 area differential equation*	Van Otterloo (2013) *fictive tenon length and 2 area differential equation* Moerbeek (2017) *3 area differential equation*	
Tests	Gustafsson (1988) Vermeij (2011) *Notch and tenon compairison*	Van Otterloo (2013) Vermeij (2011) *Notch and tenon compairison*	Judd (2004) *Tension on timber pegs in mt joints*

1.2. Research questions

The main question is:

- How is the water pressure on a closed mitre gate, transferred to the supports and how can this be verified?

The background question for this thesis is:

- What is the background of the existing verifications in the Eurocode 5 NEN-EN 1995-1-1 (2005) , mitre gate made of hardwood?

The research questions in this thesis are:

- How are the results of the FEM calculation valid?
- What do the results from the FEM calculation tell us about the stress distribution?
  - What are the differences between the heel joint and mitre joint in the gate?
  - What happens with the normal and shear forces in the mortise and tenon joint?
  - How can the two other connection methods (the peg and the steel strip and blots) influence the stresses?
- How do the notch beam and the tenon beam differ?
- What is the theoretic strength of a tenon beam?
- Why is there no observed failure of the mortise and tenon joint?

1.3. Chapters of the report

This report is divided into the following chapters:

Chapter 2 The design, the construction and the calculation method for a mitre gate.

Chapter 3 Rough calculations of the forces, stress distribution and strength.

Chapter 4 The explanation of the used finite element method model.

Chapter 5 The results of the finite element method.

Chapter 6 An analytic derivation of the shear strength of a tenon beam.

Chapter 7 A comparison of the theoretic tenon strength with test results.

Chapter 8 The conclusion of this thesis and recommendations.

2

The design and construction of a mitre lock gate

The oldest known mention of a mitre gate is by Leonardo da Vinci in the last decade of the fifteenth century, a drawing is shown in 2.1. The first known used mitre gate in the Netherlands was at Spaarndam (Grote Harelemmer Sluyse) in 1567 [28]. According to Simon Stevin in 1617, the mitre gate pond lock 'has been in use for a long time.' [21] As written by Porter, H (2000).

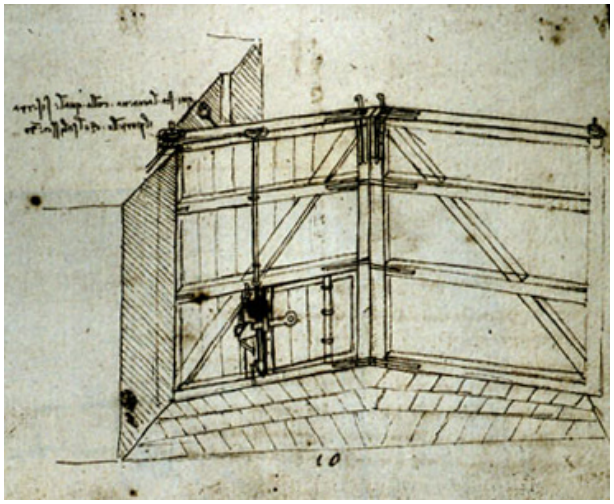

Figure 2.1: Mitre lock gate drawn by Leonardo da Vinci [8]

This illustrates the long tradition of mitre gate building in the Netherlands. Over centuries a traditional building method developed. This method is based on an iterative design process driven by experience. Van Leusen (1989:97) calls the mitre gate "an almost perfect construction". The traditional mitre lock gate designs are nowadays still the base for the design of gates.

The main difference with the traditional mitre gate is the wood species used. Old Dutch timber lock gates are made of oak while new timber lock gates are made from azobé. Today azobé is used over oak because of the good durability and strength properties of azobé.

The initial gate designs are calculated and subjected to the strength verifications according the Eurocode 5 (2015) for timber structures. When the calculations do not meet the requirements, changes in the design have to be made to fulfill the EC 5. In this chapter the design, the method of building and the prescribed verifications are explained. This chapter also contains an explanation of the different calculations and verification methods. This chapter ends with a paragraph explaining the unknowns concerning the strength of the mortise and tenon joint.

2.1. Mitre lock gate components

A mitre lock gate is build with multiple components. Figure 2.2 shows a single mitre gate with its components. This figure is obtained from van Leusen (1989) [25] and compared with drawings of recent mitre lock gates of the timber company Wijma.
A mitre gate is a timber framework; of two vertical members, the heel post (1) and the mitre post (2) with in between horizontal cross members, the girders (3,4,5). The girders are connected to the posts via mortise and tenon joints (mt joints). The joints are fastened by the use of timber pegs (14), steel straps (10) and steel T straps (11) slotted-in in the timber. These fasteners connect the girders and the posts. The straps and pegs are present in the gate to maintain a good connection between the timber elements.

Two diagonals are present in the framework for the rigidity; the timber compression stud (6) and the steel tension rods (8). The tension in the tension rod can increase by turning the swivel (15). The steel rod is fixed on the bottom corner of the gate with a through bolt (13).

The framework is covered by diagonal sheeting to make the lock gate watertight and maintain the water levels (7). To ensure a watertight fit at the heel post a strip of timber is fixed, the seal strip (17).

The gate is fitted in a metal pivot shoe (12). This ensures the connection between the timber and the bottom pivot. The gate is connected to the lock with the top pivot (9) and the bottom pivot and socket (12).

To get the gate at the location the gate is hoisted in position. The hoisting equipment is fixed to the gate at the hoisting bolts (16).

2.2. The Individual connections

Mitre gates contain several different kinds of connections. The girder post connections are described at the heel post (the joint between the the girder and the heel post), the same kind of connections are also present at the mitre post (the joint between the the girder and the mitre post). There are small dimensional differences between the heel post joint and the mitre post joint as shown in figure 2.7 and 2.8.

The in between girder and posts connection are analysed and modelled in this thesis. Other connections and imported elements of the gate are also explained in this paragraph, to obtain a complete overview in the mitre gate construction.

In between girder post connection
The mortise and tenon joint connects the girder to the post, this is shown in figure 2.3. The tenon has a thickness of 1/3 of the gate thickness. The thickness of the outside chest is 1/3 of the gate thickness. The last 1/3 of the thickness is a summation of the thickness of the sheeting and the inside chest. The length from the end of the tenon to the end of the post is 1/3 of the thickness of the gate. The length of the tenon is 2/3 of the width of the post. The depth of the mortise is made 10 mm deeper than the length of the tenon. This results in a cavity behind the tenon.

To secure the joint, timber pegs are inserted in the holes in the mortise and tenon. The holes in the mortise and tenon are not aligned, this results in pre-tensioning of the joint. The thickness of the dowel is tapered for a close fit. The timber peg is used to tighten the connection.

The joints are also fastened with steel strips and steel T-strips slotted-in and bolted to the timber frame.

Top and bottom girder post connection
The top and bottom connection are based on the normal mortise and tenon joint from the in between girder. This joint has some changes to make it suitable for the use as a top and bottom girder.

A corner of the tenon is cut along the height. This cut is in the top girder on the top, in the bottom girder on the bottom. This makes the connection stiffer and better resistant to shear deformation perpendicular to the post and torsion in the top girder according Van Leusen (1989) . Torsion occurs in the top girder because of the jack-screw or because of motion of the gate.

Figure 2.4 shows the top girder post joint. The inside chests are oblique bevelled while the outside chests are strait. On the inside chests there is a notch of 10 mm to accommodate the sheeting.

The timber pegs are used in the same way as in the in between joint. The joints on the heel side of the gate are enclosed in the steel shoes. The joints on the mitre side are fastened with steel t-strips bolted to the timber frame.

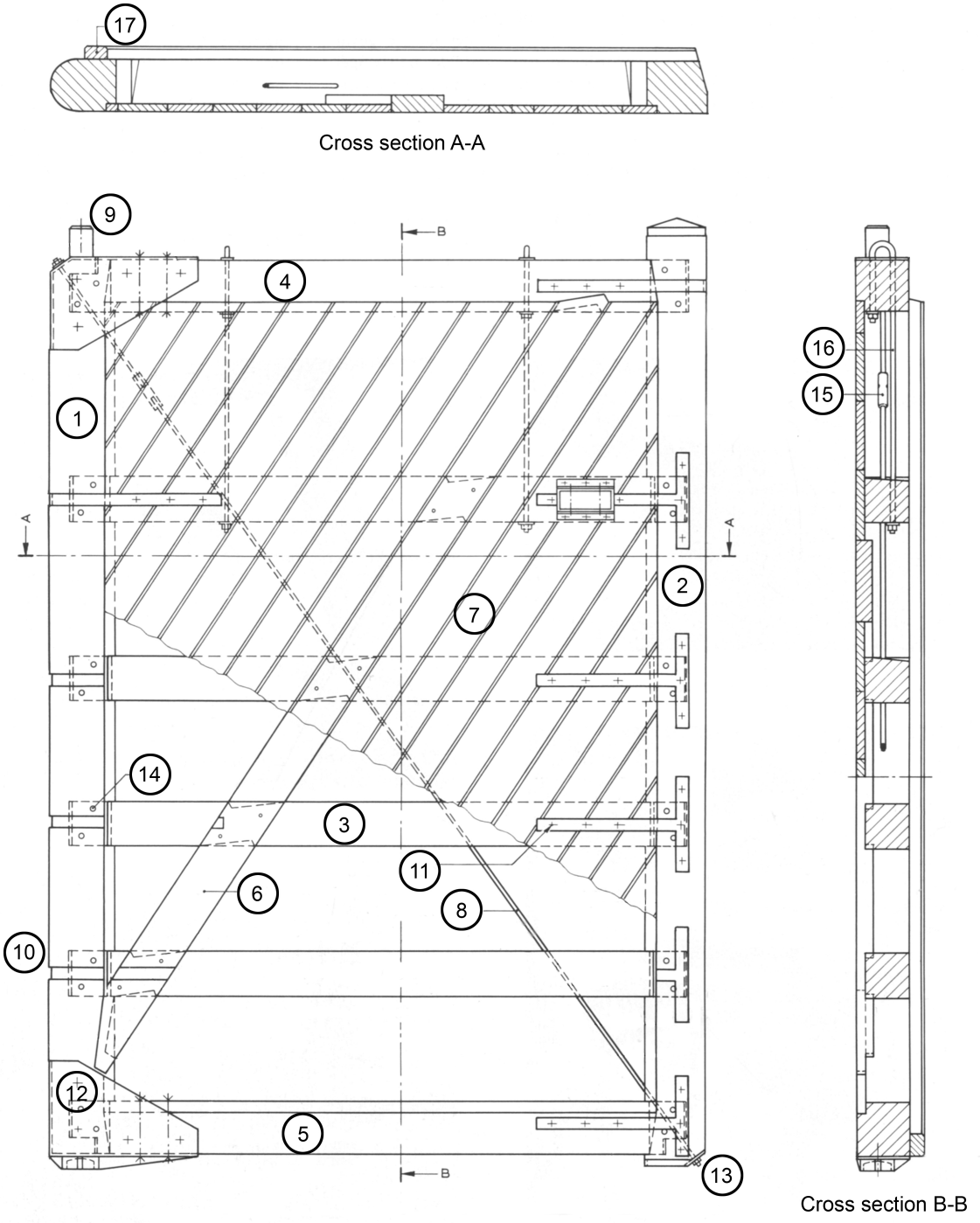

Figure 2.2: Outside overview of a lock gate (edited from [25], fig. 63.1)

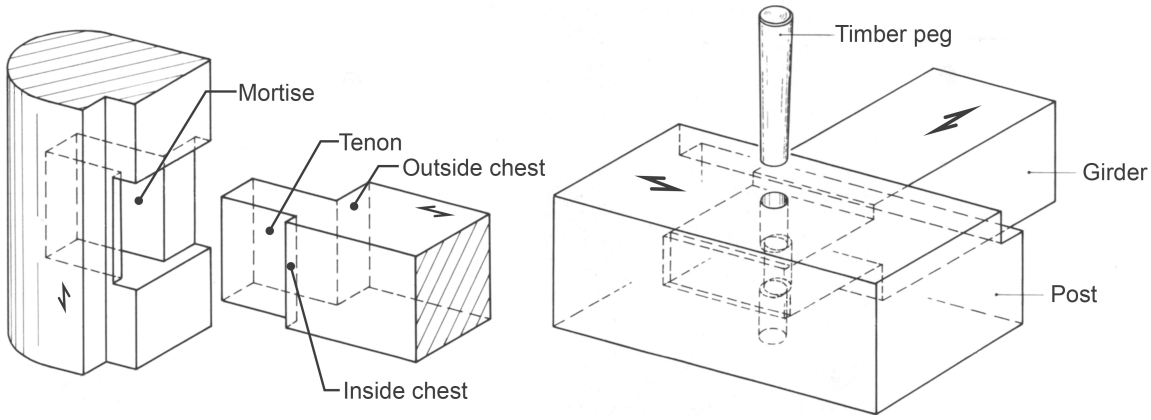

Figure 2.3: Inside view of the in-between girder (left) and the use of the timber peg (right) (edited from [25], fig. 63.16 and 63.5)

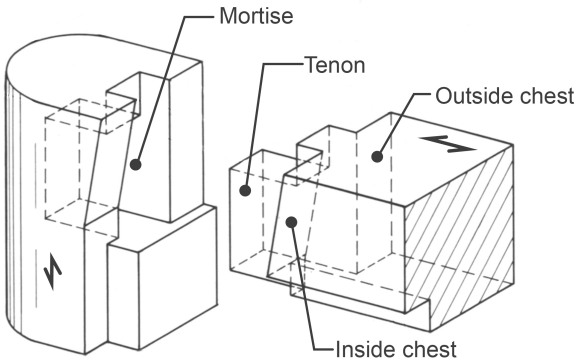

Figure 2.4: Inside view of the top girder (edited from [25], fig. 63.12)

The diagonal stud, girder and post connection

The diagonal stud is connected to the post, by a tooth and concealed teeth joints. The teeth slide in notches made in the post. This is shown in figure 2.5

When the diagonal stud cross the girder, notches are made in the stud. At this crossing the stud is slimmed to half its depth. At the top and the bottom of the girder teeth are used to ensure a connection. The fabricated notches in the girder are as small as possible to have minimal weakening of the girder. To ensure a tight connection bolts are used to connect the stud to the girders.

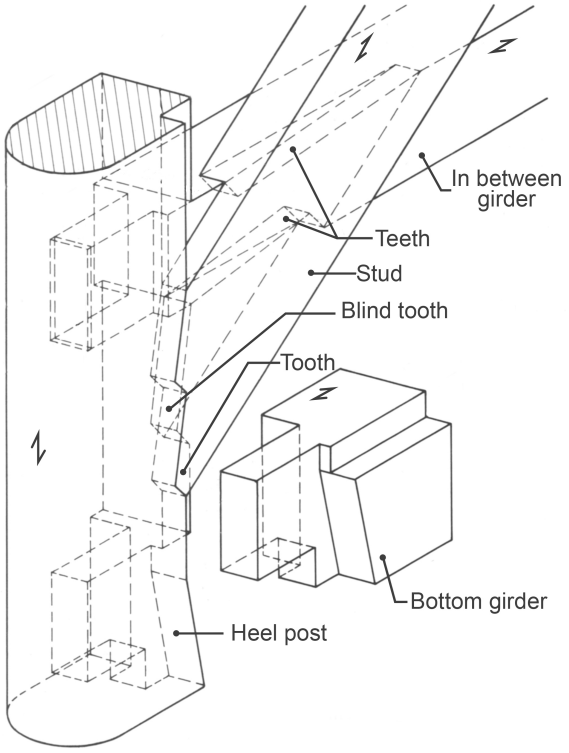

Figure 2.5: Inside view of the diagonal stud, girder and post connection (edited from [25], fig. 63.25)

Sheeting

The sheeting is connected to the framework by using galvanized steel nails. The nails are put in pre drilled holes to prevent the splitting of the timber. The distance between the nails is around 100 mm. The gaps between the sheets are filed up with a filler to ensure the water resistance.

The pivot shoe

The pivot shoe is made out of casted steel or welded steel. The shoe is horizontal connected by bolting it to the timber frame, vertically it is also bolted to the timber. There are holes in the shoe reserved for the seal strip, this strip is located outside the shoe. The steel shoe is slotted-in in the timber this makes it flush along height of the gate.

The shoes are responsible for the rotation of the gate. The rotation is only possible when the rotation points of the pivots are exactly aligned with the top and bottom. The rotation point of the gate is not in the middle of the post M in figure 2.6. This would lead to sanding in the embedment of the gate. The rotation point is located at a distances outside of the middle point R, this way free rotation is possible as shown in figure 2.6.

The seal strip

The seal strip is located along the heel post and is made out of a strip of azobé. The strip is fixed to the post by coach screws. The screws are recessed in the stripe to ensure straight surface, to retain the water tightness.

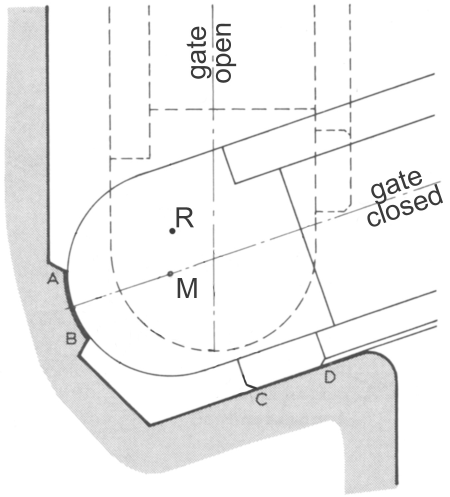

Figure 2.6: Top view of the rotational point R of the pivot shoe (edited from [25], fig. 61.10a)

2.2.1. The dimensions of the mitre gate

In van Leusen (1989) member sizes are given depending on the thickness of the gate, this thickness is obtained according traditional building experience. This results in that, there are only small variations between different mitre gates. Table 2.1 and figure 2.7 and 2.8 shows common dimension formulas for member sizes and the dimensions used in this thesis.

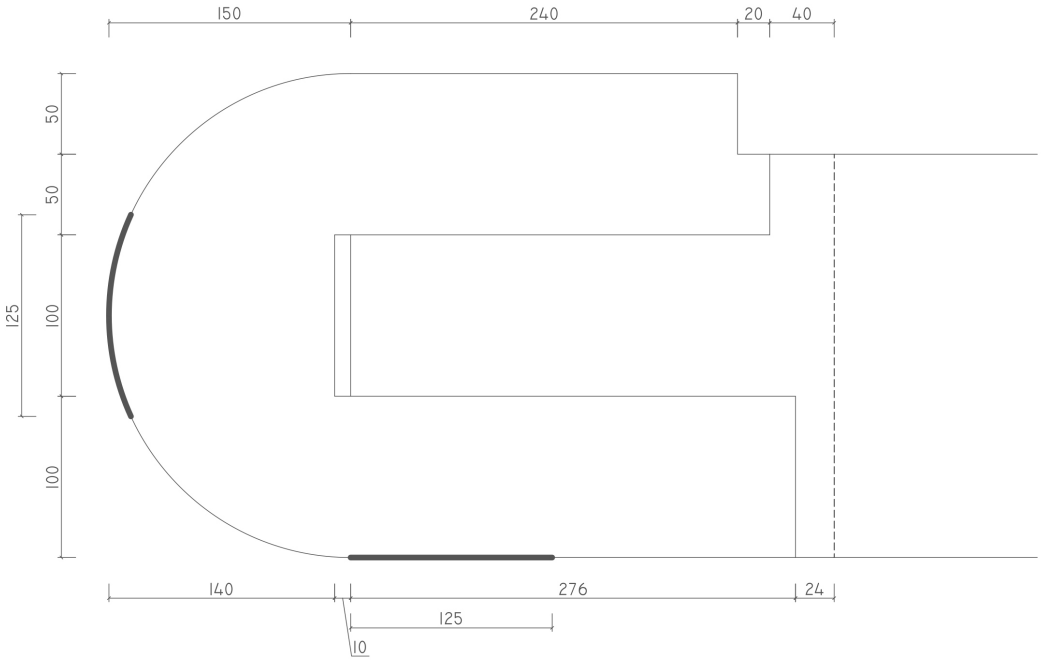

Figure 2.7: Dimensions [mm] of the of the used heel joint.

2.3. Strength verification

To calculate the structural safety of a structure, the strength of the structure is an important property. The strength is used in an analysis with the design stress to provide the safety of the construction. Due to the centuries of development of the mortise and tenon joint design, design rules where found empirically. This empirical approach leads to an apparently safe connection while the strength of individual connections are unknown. Nowadays the structural safety of a construction

Table 2.1: Member dimensions according van Leusen (1989) [25]

Assumed parameter	**Character**	**Value**
Total depth mitre gate	d	300 mm
Length girder between posts	l_g	3000 mm
Depth sheeting	s	50 mm
Angle of the gate when closed	α_g	$15^\circ - 30^\circ$ deg
Depth girder	d_g	250 mm
Height girder	h_g	250 mm
Derived parameter	**Relation**	**Value**
Width heel post (w_d)	$1,5d$	450 mm
Width mitre post (w_m)	$1,2d$	360 mm
Chamfer length mitre post (l_c)	$d/2$	150 mm
Total length gate (L)	$w_d + w_m + l_g$	3810 mm
Length heel tenon (l_{ht})	$2w_d/3$	300 mm
Length mitre tenon (l_{mt})	$2w_m/3$	240 mm
Length inside chest (l_{ic})		40 mm
Length outside chest (l_{oc})		24 mm
Length heel mortise (l_{hm})	$l_{ht} + 10$ mm	310 mm
Length mitre mortise (l_{mm})	$l_{mt} + 10$ mm	250 mm
Depth inside chest (d_{ic})	$d/3 - s$	50 mm
Depth tenon (d_t)	$d/3$	100 mm
Depth outside chest (d_{oc})	$d/3$	100 mm
Rebate depth	s	50 mm
Rebate width (s_w)	$s + 10$	60 mm
Seal strip		75x125 mm
Heel support length		125 mm

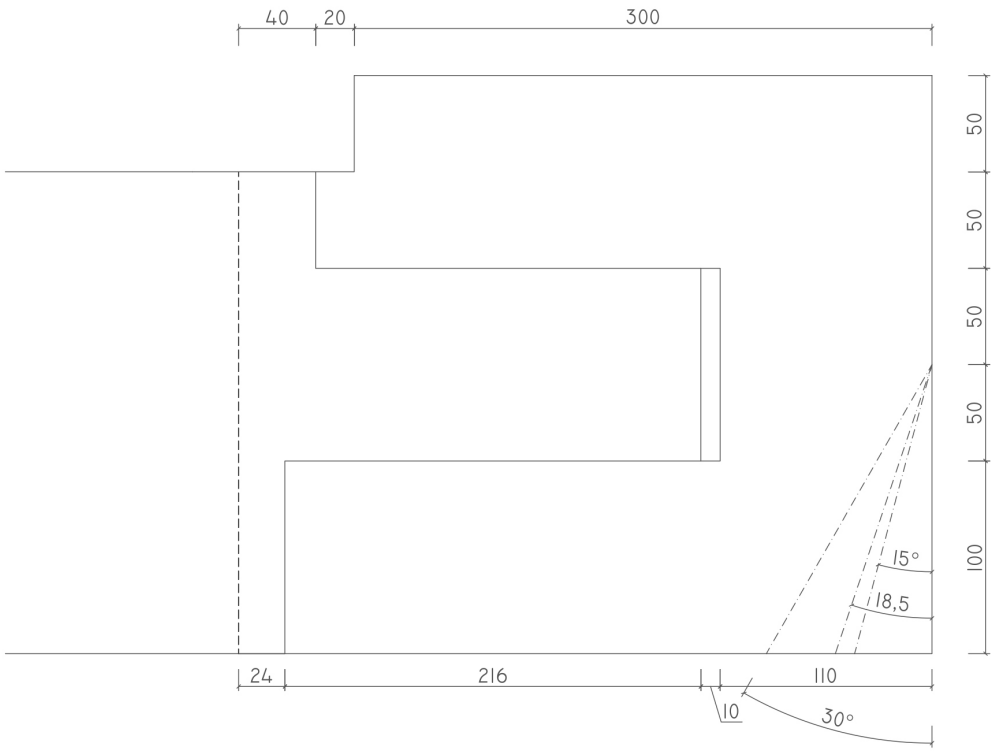

Figure 2.8: Dimensions [mm] of the of the used mitre joint.

needs to be known to fulfil the building regulations. For the mt joint the strength is unknown, this makes it complicated for construction firms to use the mt joint.

Dimensions of the gate are deduced from the thickness of the gate. The thickness of the gate was determined by the use of building experience. Al new timber structures should be verified according Eurocode 5. The EC 5 has no special section on lock gates. This means that the constructor needs to verify the gate using the different verification methods. The verification is based on the acting stress compared to the maximum strength. The EC 5 provides the maximum strength equations while the constructor provides the acting stresses. The acting stress distribution in the mt joints are unknown. Without knowing the stress distribution verification is based on assumed stress and not acting stresses.

The four common used verifications (unity checks) for the mt joint in the Eurocode 5 are the combined pressure, the bending check, the shear and the reduced shear verification for the tenon. The first three unity checks are okay and still under the value of 1,0, for the assumed stress. The reduced shear stress for notch reduction is done according to paragraph 6.5.2 of Eurocode 5 NEN-EN 1995-1-1 (2005). This verification will lead to too high unity checks. This implies that the mt joint will fail in tension splitting parallel to the fibre of the timber, although this failure has not occur in existing gates. Thus the problem is two folded the acting stresses are unknown and the reduced shear verification indicates splitting failure.

Example reduced shear verification

In table 2.2 an example reduced shear verification is made to illustrate the problem. The calculation uses the equations 2.1 and 2.2. In the next paragraph a closer look is taken, at the background of the reduced shear calculation in the EC 5.

$$\tau_d = \frac{1,5V}{bh_e} \leq k_v f_{v,k} \frac{k_{mod}}{\gamma_m} = k_v f_{v,d} \tag{2.1}$$

The reduction factor k_v is calculated with dimensions from the mt joint in table 2.1 using the equation 2.2. In equation 2.2 $k_n = 5$ for solid timber, i is zero because there is a straight corner with $a = \frac{h_e}{h}$.

$$k_v = min \begin{cases} 1,0 \\ \frac{k_n\left(1+\frac{1,1i^{1,5}}{\sqrt{h}}\right)}{\sqrt{h}\left(\sqrt{\alpha(1-\alpha)}+0,8\frac{x}{h}\sqrt{\frac{1}{\alpha}+\alpha^2}\right)} \end{cases} \tag{2.2}$$

Verification 2.1 is suitable for notched beams. To make it possible to verify an tenon beam acording the EC 5, Ehlbeck and Kromer (1995) did an assumption. Ehlbeck and Kromer assumed that the tenon height is the same as the notch height h_e. This is done by moving the tenon to the top of the beam shown in figure 2.9 an equvalent notch beam according Ehlbeck and Kromer (1995) is found and can be used for verification.

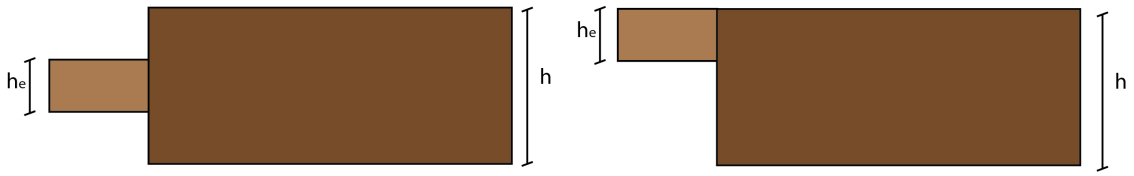

Figure 2.9: Ehlbeck and Kromer (1995) [9] assumption for notch to tenon beams. The real configuration (left). The assumed equivalent (right)

The example calculation shows, how the calculation method works. In this calculation the shear stress is verified for the heel joint. This is done for service class 3 with load duration long-term. Service class 3 is characterised by a wet climate conditions this is appropriat for a lock gate that is permanantly exposed to water. The long-term load duration class is for loads durations of 6 monthes to 10 years. This results in $k_{mod} = 0,55$ for solid timber. Acording NEN-EN 338 (2016) the shear strength for D70 of $f_{v,k} = 5\ N/mm^2$ should be used. The shear strenght value of tropical hardwood timber given in NEN-EN 338 (2016) is questionable according Ravenshorst and Gamper (2016), because no large scale test have been preformed on tropical hardwood acording the NEN-EN 408 (2012). The value of the shear strenght is changed to $f_{v,k} = 13.5\ N/mm^2$ according van de Kuilen and Blass (2005) , this is explained in paragraph 2.5.3. The shear force is obtained by a calculation shown in paragraph 3.3.1 with a angle of the gate of 18,5° degrees and a distributed load of 35 kN/m. The force 35 kN/m corresponds with a water level difference of 2,33 m and a distance of 1,5 m between the girders.

Table 2.2: Example calculation for the heel joint

Parameter	size	dimension
b	250	mm
h	250	mm
h_e	100	mm
x	213,5	mm
$\alpha = h_e/h$	0,4	–
k_n	5	–
k_v	0,21	–
γ_m	1,3	–
k_{mod}	0,55	–
V_d	53,93	Kn
$f_{v,k}$	13,5	N/mm^2
t_d	3,24	N/mm^2
$k_v f_{v,d}$	1,18	N/mm^2
$t_d/k_v f_{v,d}$	$2,75 \geq 1,0$	Not okay

As the calculation shows this mt joint is not safe according the Eurocode 5, if the prescribed shear strength is used with $f_{v,k} = 5\ N/mm^2$ the unity check becomes 7,43 this is even higher. After this calculation the construction firm will change the geometry of the mt joint to fulfil to this verification, as illustrated in figure 2.10. This change is done to meet this verification method, while possibly this verification method based on a notch beam it not valid for mt joints. Paragraph 2.5 explains the issues with the reduced shear strength verification method.

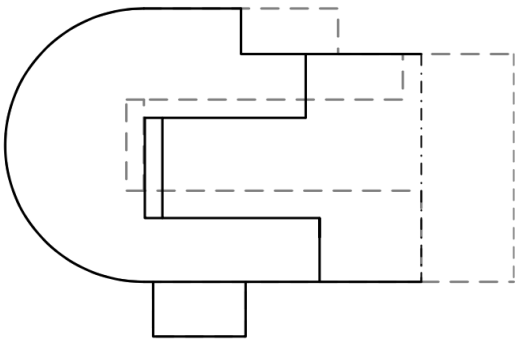

Figure 2.10: The original mt joint geometry (doted line) the new geometry (closed line). (obtaind from [26], fig. 26)

2.4. The background, of the strength of the notched beam as prescribed by Eurocode 5

The background of this calculation method for the strength of a notched beam is explained in this paragraph. The strength according the Eurocode 5, is based on a theoretical expression for reduced strength of a notched beam with the use of linear fracture mechanics by Gustafsson (1988) . Larsen and Gustafsson (1990) did extensive tests to determine the fracture energy perpendicular to the grain of softwood. Both studies are used in the reduction factor k_v of the shear strength check in the Eurocode 5.

2.4.1. Assumptions for the derivation for the notch strength

It is difficult to formulate a maximum stress strain criterion at the tip of the notch. Linear elastic stress analysis estimate a stress that approach infinity in sharp concave corners. This is not possible in reality, due to the material strength and brittle cracking. Also local initial cracks will influence the possible stress distribution. Those initial cracks can propagate as a result of the stress. A possible way to analyse crack propagation is by using fracture mechanics.

When a member has homogeneous tension or bending stresses, conventional stress calculations can be used for fractures

verification. When the stresses are local, with high concentrations, as in corners of a notched beam, a different approach is needed. The derivation by Gustafsson (1988) uses the energy release rate for the fracture mechanics.

Assumptions for the linear elastic fracture mechanics are: the timber is assumed orthotropic and a linear elastic material. The fractures theory assumes an initial crack. This is an appropriate assumption because of the production, the handling and shrinkage and swelling due to moisture differences in the timber. This can lead to initial cracks.

2.4.2. Derivation of the theoretical notched strength

The beam is split in its symmetric half according figure 2.11 and 2.12. The potential energy W $[Nm]$ of half of the system subjected to the external load is: $W = (-V\delta)/2$. With the shear force V $[N]$ and the deflection δ $[m]$ at the load point.

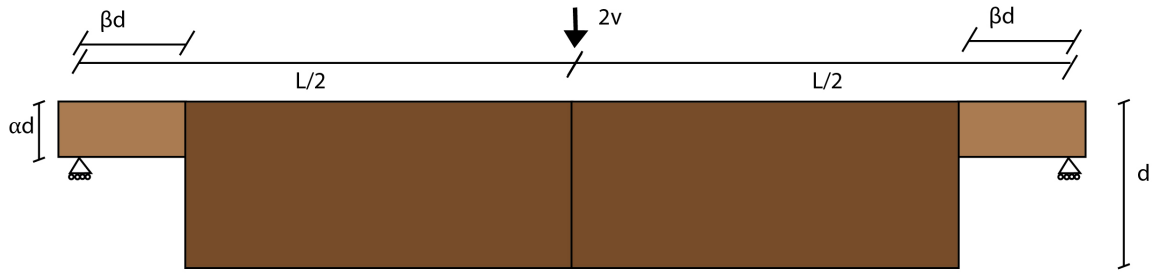

Figure 2.11: Notched beam subjected to a point load

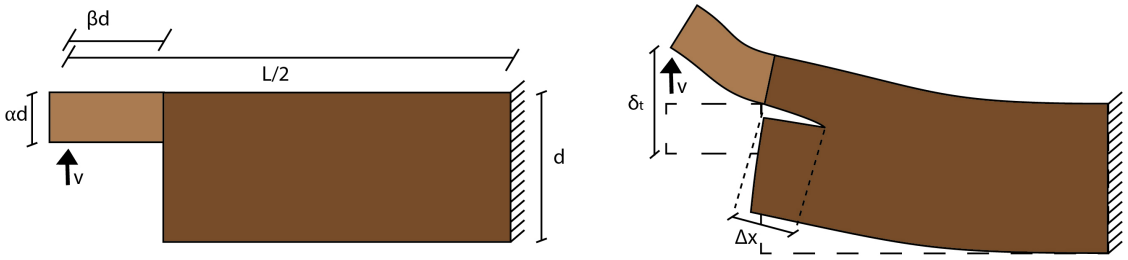

Figure 2.12: Half of notched beam subjected to a point load

The potential energy changes with ΔW_p $[Nm]$, due tot the increased crack length Δx $[m]$ lead to an extra deflection $\Delta\delta$ $[m]$. A constant shear force V $[N]$ will changes in to the included equation 2.3 with the potential energy shown in graph 2.13.

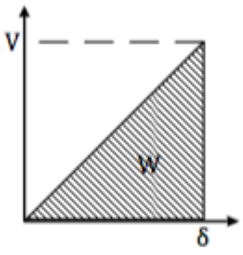

Figure 2.13: Increase of the energy dependent on δ $[m]$ and V $[N]$

$$\Delta W_p = \frac{-V\Delta\delta}{2} = -\frac{V^2}{2}\Delta\left(\frac{\delta}{V}\right) \tag{2.3}$$

The crack develops when the shear force is $V = V_f$ $[N]$. This will lead to loss of potential energy of $-\Delta W_p$. This loss equals the energy required to form a crack. This is described by formula 2.4

$$\frac{V_f^2}{2}\Delta\left(\frac{\delta}{V}\right) = G_c b \Delta x \tag{2.4}$$

Here G_c $[J/m^2] = [Nm/m^2] = [N/m]$ is the material dependent fracture energy per crack area. The depth of the beam is b $[m]$.

The crack part of the beam will decrease the height of the beam, this will lead to a lengthening of the notch by $\Delta x = d\Delta\beta$. Using this in equation 2.4, introducing α^2 on both sides and taking the limit of $\Delta\beta \to 0$, will lead to equation 2.7

$$\frac{V_f^2}{2\alpha^2}\Delta\left(\frac{\delta}{V}\right) = \frac{G_c}{\alpha^2} bd\Delta\beta \tag{2.5}$$

$$\frac{V_f^2}{b^2\alpha^2 d^2} = \frac{2G_c\Delta\beta}{\alpha^2 bd\Delta\left(\frac{\delta}{V}\right)} \tag{2.6}$$

$$\frac{V_f}{b\alpha d} = \sqrt{\frac{2G_c}{b\alpha^2 d} / \frac{\Delta\left(\frac{\delta}{V}\right)}{\Delta\beta}} \tag{2.7}$$

An important part of this equation is the beam deflection at the location of the shear force. This deflection can be described by a summation of 4 deflections 2.8 as shown in figure 2.14.

$$\delta = \delta_t = \delta_l + \delta_v + \delta_e + \delta_r \tag{2.8}$$

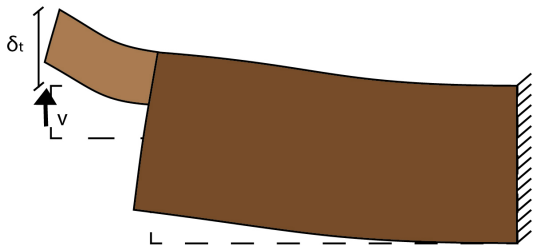

Figure 2.14: Total displacement of the notch

The local deformation δ_l, is the deformation of the material at the support due to the loading, like indentation. The local deformation is independent of β, and therefore not needed.

The shear deflection δ_v, is the deflection as a result of the shear modulus from the material. The shear deformation is obtained by using the differential equation for a shear beam. The differential equations and the used boundary conditions are present in the appendix A. The shear beam is divided in two fields to obtain the following deflection: $d = \frac{V}{G_{xy}}\left(\frac{\beta d}{b\alpha d} + \frac{L/2-\beta d}{bd}\right)$ also displayed in figure 2.15. The found shear deflection is multiplied with 1,2 to get the used shear deflection. This is done because of the parabolic shear stress, while the found deflection assumes a constant shear. The final deflection is equation 2.9

$$\delta_v = \frac{1,2V}{G_{xy}}\left(\frac{\beta d}{b\alpha d} + \frac{L/2-\beta d}{bd}\right) \tag{2.9}$$

The bending deflection δ_e, is the deflection as a result of the Young's modules of the material. The bending deformation is obtained by using the differential equation for an Euler beam. The differential equations and the used boundary conditions are present in the appendix A. The Euler beam is divided in two fields to obtain the following deflection 2.10 this is also displayed in figure 2.16.

$$\delta_e = \frac{V}{E_x bd^3/12}\left(\frac{L^3}{24} + \frac{(\beta d)^3}{3}\left(\frac{1}{\alpha^3} - 1\right)\right) \tag{2.10}$$

The rotational deflection δ_r, is a deflection the result of the elastic clamping of the cantilever βd. At βd the height of the beam increases. The stresses are not directly transferred over the full height d. It takes the length of x_t to use the full height d of the beam, shown in figure 2.17. This results in elastic clamping. This clamping is modelled with a compliance rotational spring c $[1/Nm]$. This will lead to the rotational deflection 2.11 shown in figure 2.18.

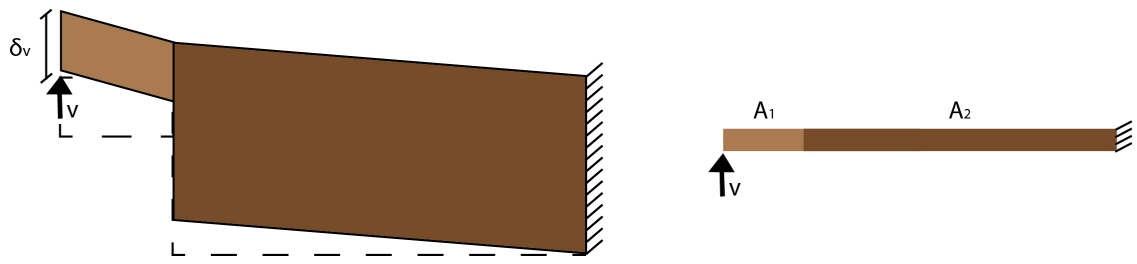

Figure 2.15: Shear displacement of the notch

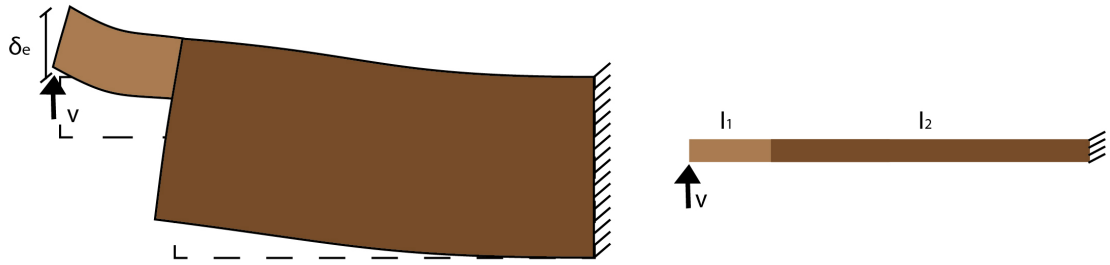

Figure 2.16: Bending displacement of the notch

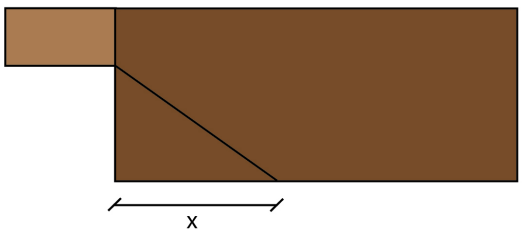

Figure 2.17: Transition length of the notch

$$\delta_r = cV\beta^2 d^2 \tag{2.11}$$

Gustafsson (1988) used equation 2.12 for the rotational spring c $[1/Nm]$. This c value was mathematical obtained, to made it possible to write it in the a equation 2.13. There is no mechanics or beam theory to support this but according the test of Gustafsson (1988) equation 2.12 it gave better results than $c = 0$. How the equation 2.12 was obtained is shown in the paragraph 2.4.3.

$$c = \frac{12}{b\alpha^2 d^2}\sqrt{\frac{(1-\alpha)\left(1-\alpha^3\right)}{10G_{xy}E_x}} \tag{2.12}$$

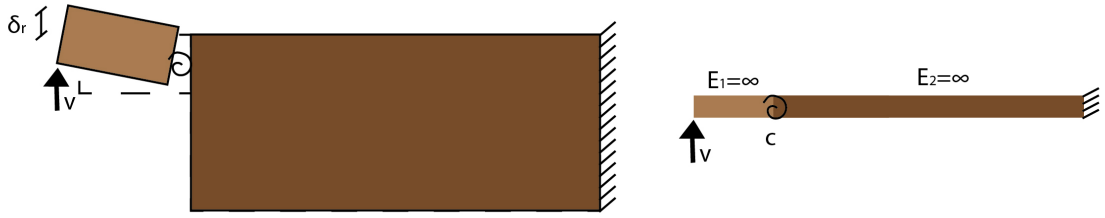

Figure 2.18: Rotation displacement of the notch

Gustafsson chose to writes the total deflection as equation 2.13. How this total displacement equation is obtained is shown in paragraph 2.4.3.

$$\begin{aligned} \delta_t &= A\left(B+\beta d\right)^3 + constant \\ A &= \frac{V}{3E_x bd^3/12}\left(\frac{1}{\alpha^3}-1\right) \\ B &= d\sqrt{\frac{E_x}{10G_{xy}}\frac{(1/\alpha-1)}{(1/\alpha^3-1)}} \end{aligned} \tag{2.13}$$

Differentiating the deflection 2.13 results in 2.14. The differentiated deflection is assumed positive, this will result in 2.15. Multiplying the numerator and denominator with $\sqrt{\frac{b\alpha^2}{2}}$ results in 2.16. Filing in A and B will result in the final equation 2.17.

$$\frac{\Delta\frac{\delta}{V}}{\Delta\beta} = 3Ad\left(B+\beta d\right)^2 = \left(\sqrt{3dAB^2}+\beta\sqrt{3d^3A}\right)^2 \tag{2.14}$$

$$\frac{V_f}{b\alpha d} = \sqrt{\frac{2G_c}{b\alpha^2 d}}\cdot\frac{1}{\sqrt{3dAB^2}+\beta\sqrt{3d^3A}} \tag{2.15}$$

$$\frac{V_f}{b\alpha d} = \frac{\sqrt{G_c/d}}{\sqrt{1,5b\alpha^2 dAB^2}+\beta\sqrt{1,5b\alpha^2 d^3A}} \tag{2.16}$$

$$\frac{V_f}{b\alpha d} = \frac{\sqrt{\frac{G_c}{d}}}{\sqrt{\frac{0,6(\alpha-\alpha^2)}{G_{xy}}}+\beta\sqrt{\frac{6\left(\frac{1}{\alpha}-\alpha^2\right)}{E_x}}} \tag{2.17}$$

2.4.3. Derivation of the compliance elastic clamping spring for a notch beam

The equation for c equation 2.12 is mathematically obtained to make it possible to write the total displacement of the notch as equation 2.13. With $c = 0$ the total displacement equation 2.13 will be a more complex equation. An other important reason why this c $[1/Nm]$ value is used is because it corresponds better with tests.

The equation 2.12 from Gustafsson (1988) is obtained via the following steps. Using mathematics an approximation for the rotational displacement is found, there is no mechanics theory to support this displacement. The displacements will be differentiated to β when inserted in equation 2.7, this means that only the part of the equation dependent on β will be included in this derivation. The other parts are the constants and will disappear when differentiating the displacement to β. Rewriting the shear 2.9 and bending 2.10 displacements equations dependent of β are 2.18 and 2.19. Expending equation 2.13 will lead to equation 2.20.

$$\delta_v = \frac{1{,}2V\beta d}{G_{xy}bd}\left(\frac{1}{\alpha}-1\right)+constant \tag{2.18}$$

$$\delta_e = \frac{V(\beta d)^3}{3E_x bd^3/12}\left(\frac{1}{\alpha^3}-1\right)+constant \tag{2.19}$$

$$\delta_t = A(B+\beta d)^3+constant = A(\beta d)^3+3AB(\beta d)^2+3AB^2(\beta d)+AB^3+constant \tag{2.20}$$

The total displacement equation 2.20 is a polynomial of βd. The shear displacement 2.18 is dependent on βd. The bending displacement 2.18 is dependent on $(\beta d)^3$. Matching the βd's of the shear and bending displacement to the total displacement shows how the values for A and B are obtained. This is shown in equation 2.21 and 2.22.

$$\begin{aligned} A(\beta d)^3 &= \delta_e \\ A &= \frac{\delta_e}{(\beta d)^3} = \frac{V}{3E_x bd^3/12}\left(\frac{1}{\alpha^3}-1\right) \end{aligned} \tag{2.21}$$

$$\begin{aligned} 3AB^2(\beta d) &= \delta_v \\ B &= \sqrt{\frac{\delta v}{3A(\beta d)}} = d\sqrt{\frac{E_x}{10G_{xy}}\frac{(1/\alpha-1)}{(1/\alpha^3-1)}} \end{aligned} \tag{2.22}$$

The rotational deflection equation 2.11 is dependent of $(\beta d)^2$ this is corresponds with the second term in equation 2.20. With the previous calculated A and B is it possible to calculate the c value.

$$\begin{aligned} \delta_r &= cV(\beta d)^2 = 3AB(\beta d)^2 \\ c &= \frac{3AB}{V} = \frac{12}{b\alpha^2 d^2}\sqrt{\frac{(1-\alpha)(1-\alpha^3)}{10G_{xy}E_x}} \end{aligned} \tag{2.23}$$

The equation for c equation 2.23 shows that this is equal to the equation for c presented in Gustafsson (1988). When c has a diverend value than equation 2.23 it is not posible to write it as equation 2.13 this is the matamatical motivation for the c value. With the found c value in equation 2.23 Gustafsson (1988) continues to obtain equation 2.17.

In Smith and Springer (1993) is written that $c = 0$ is consistent with the theoretical behaviour of an elastic notched beam, this means only concidering the displacement due to shear and bending. Houwever the assumption of $c = 0$ leads to worse predictions in tests, than when equation 2.12 is used. Smith and Springer (1993) did a function fitting on test results. There was found that the clamping effect is $c \neq 0$ and that $1/\alpha^3$ instead of $1/\alpha^2$ in the elastic clamping equation 2.12 lead to a more coherent prediction. More research in the rotational deflection behaver is needed. In this thesis the mathematical obtained c value is used for the rotational deflection.

The influence of the c value equation 2.12 on the theoretical deflection is shown in table 2.3. The value's are obtained by $\frac{\delta_r}{\delta_v+\delta_e}$ with the deflection equations 2.9, 2.10 and 2.11. The value's that are used are: $V = 50\ Kn$, $E_x = 20000\ N/mm^2$, $G_{xy} = 1250\ N/mm^2$, $b = 250\ mm$, $d = 250\ mm$ and $L = 3\ m$. As an indication on the size of the displacement $\alpha = 0.25\%$ and $\beta = 0.75\%$ leads to displacements of $\delta_v = 1{,}6\ mm$, $\delta_e = 9{,}7\ mm$ and $\delta_r = 1{,}2\ mm$

Table 2.3: The influence of α and β on $\frac{\delta_r}{\delta_v+\delta_e}$

	$\beta = 0{,}10\%$	$\beta = 0{,}25\%$	$\beta = 0{,}50\%$	$\beta = 0{,}75\%$	$\beta = 1{,}00\%$	$\beta = 1{,}25\%$	$\beta = 1{,}50\%$
$\alpha = 0{,}20\%$	0,3%	2,1%	7,8%	15,3%	21,8%	25,8%	27,5%
$\alpha = 0{,}25\%$	0,2%	1,3%	5,0%	10,4%	16,2%	21,1%	24,5%
$\alpha = 0{,}33\%$	0,1%	0,7%	2,7%	5,9%	9,8%	13,9%	17,7%
$\alpha = 0{,}50\%$	0,0%	0,3%	1,0%	2,2%	3,9%	5,9%	8,2%

2.4.4. Conclusions regarding Gustafsson (1988)

The conclusions from the research and experimental results found by Gustafsson (1988) are:

1. The material properties: shear stiffness, bending stiffness and the fracture energy are present in the reduction of the strength in equation 2.17.
2. The theoretical analysis with fracture mechanics obtained a closed-form expression for the notch strength. Tests of Gustafsson (1988) give results in line with the expression.
3. The assumption regarding the splitting energy is correct. The test results in Gustafsson (1988) show, no statistical correlation between the notch strength and tensile strength perpendicular to the grain writen in Gustafsson and Enquist (1988).

4. The length βd the distance of the force to the tenon pit, is imported for the notch strength.

Smith and Springer (1993) add extra conclusions and remarks regarding the article of Gustafsson (1988). Smith and Springer (1993) end with remarks regarding the Eurocode 5 design formula.

1. The equation 2.17 is not valid for: different support conditions, differed load distributions and differed notch arrangements than shown in 2.11.
2. At the base of equation 2.7 is the assumed a constant shear force over the beam, thus it is only valid for constant shear force.
3. With $c = 0$ there is a match with beam theory: shear displacement plus bending displacement is the total displacement. Tests show that $c \neq 0$. Mathematical c is obtained to make it possible to write it as 2.8.
4. It is unknown whether the fracture energy G_c is independent of the direction of the crack growth compared to the grain and possible failure mode.

2.4.5. Fracture energy

The fracture energy for splitting G_c can be in multiple modes: tension stress perpendicular to the grain mode 1, pure shear stress mode 2 and a possible combination of shear stress and tension stress perpendicular to the grain. Mode 1 and mode 2 are shown in figure 2.19. With the notches on the tension height of the beam, it is reasonable to assume, that the fracture energy is pure tensile splitting perpendicular to the grain $G_c = G_{f,y}$ $[Nmm/mm^2]$, this leads to equation 2.24. The other parameters in the equation 2.24 are: the splitting shear force V_f $[N]$, the depth of the beam b $[mm]$, the shear modulus G_{xy} $[N/mm^2]$, the modulus of elasticity E_x $[N/mm^2]$. The geometric parameters are shown in figure 2.12, α $[-]$, β $[-]$ and d $[m]$.

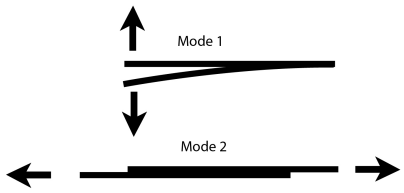

Figure 2.19: Possible spiting mode 1 and mode 2

$$\frac{V_f}{b\alpha d} = \frac{\sqrt{\frac{G_{f,y}}{d}}}{\sqrt{\frac{0{,}6(\alpha-\alpha^2)}{G_{xy}}} + \beta\sqrt{\frac{6\left(\frac{1}{\alpha}-\alpha^2\right)}{E_x}}} \tag{2.24}$$

2.4.6. Obtained fracture energy perpendicular to the grain for softwood

An extensive experimental program at several institutes obtained the fracture energy for softwood (mainly Picea abies and Pinus sylvestris), Larsen and Gustafsson (1990) reported the results. In this program all the European softwood are considered as one population. This leads to a relation between the fracture energy in pure tensile splitting perpendicular to the grain as shown in figure 2.20. The relation that is found is dependant on the density of the timber. $G_{f,y} = 1.04\rho - 146$ The correlation coefficient for this relation is $R = 0,78$ this is $R^2 = 0,61$. Figure 2.20 shows the data points and the regression line. With the fracture energy $G_{f,y}$ $[Nm/m2]$ and the mean density ρ $[kg/m3]$.

The conclusion of Larsen and Gustafsson (1990) is that the fracture energy in mode 1 of combined European softwood increases linearly with the density. Individual species or grouped species can lead to more precise relationships.

2.4.7. The derivation of the design formula for reduced notch strength

The expression 2.17 found in the paragraph 2.4.2 is the base for the design formula for the reduced notch strength. Larsen et al. (1992) reformulated the expression 2.24 to get the design formula. This is done by rewriting it to equation 2.25 to 2.30.

$$\tau_d = \frac{3}{2}\frac{V_f}{b\alpha d} \leq k_v f_v \tag{2.25}$$

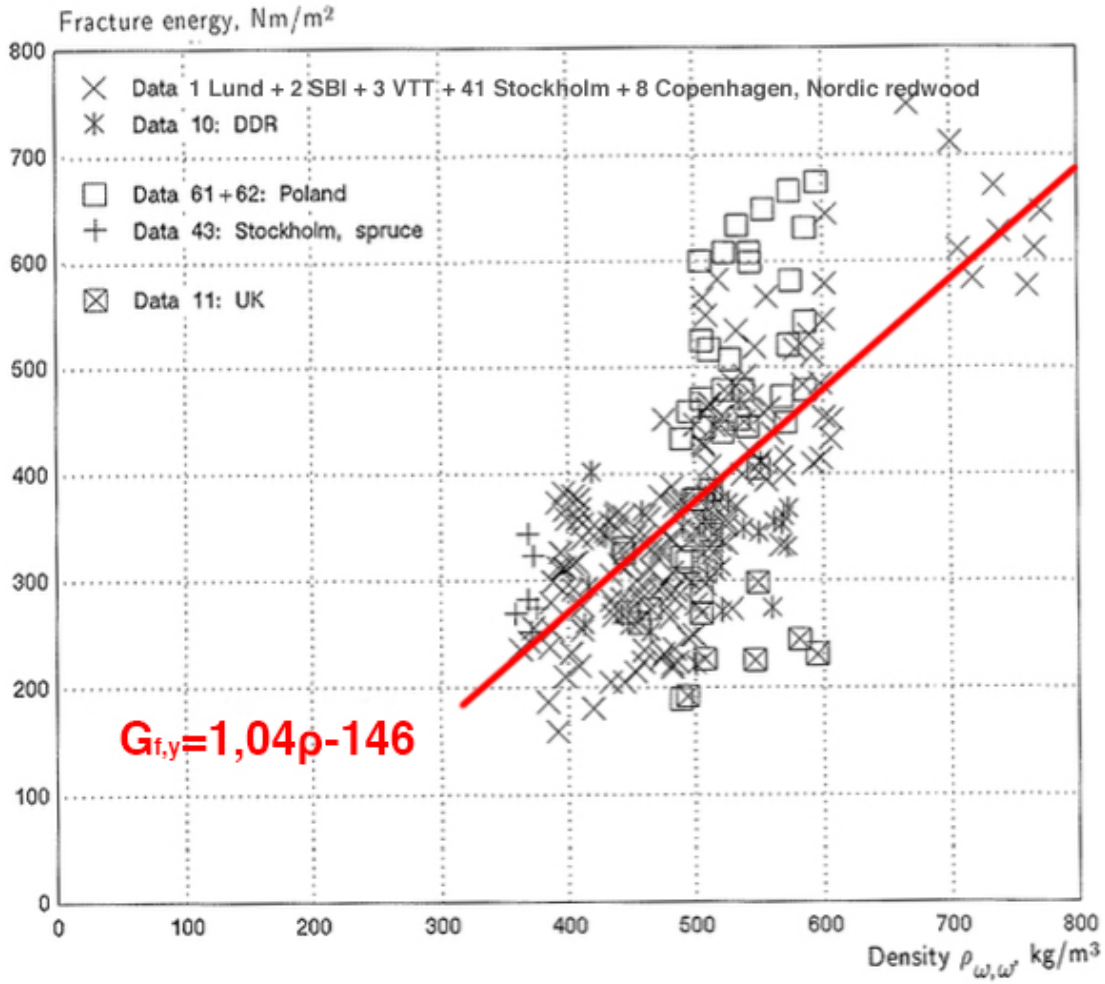

Figure 2.20: Density against the fracture energy for European softwoods (edited from Larsen and Gustafsson (1990) [13] fig. 5)

$$k_v = \frac{k\sqrt{\frac{E_x G_{f,y}}{f_v^2 d}}}{\sqrt{\frac{0{,}6(\alpha-\alpha^2)E_x}{G_{xy}}} + \beta\sqrt{6\left(\frac{1}{\alpha}-\alpha^2\right)}} \tag{2.26}$$

Rewriting equation 2.25 with 2.26 from equation 2.24 is done by introducing the factors k [−], and moving E_x, introducing $\frac{f_v}{f_v}\left[\frac{N/mm^2}{N/mm^2}\right]$ and adding value 1.5 for the parabolic shear stress. To obtain equation 2.27 and 2.28 the assumption $E_x/G_{xy} = 16$ from NEN-EN 338 (2016) is substituted in the denominator, this leads to the 1/3 in K and to $\sqrt{6}/\sqrt{0{,}6\dot{1}\dot{6}} = 0{,}8$ in front of β. The last rewrite is done to move the d to the denominator and introducing factor K [$\sqrt{m}$] in the numerator. K is a factor depended of multiple material properties shown is equation 2.27. k_v will than become equation 2.28.

$$K = \frac{1}{3}\sqrt{\frac{E_x G_{f,y}}{f_v^2}} \tag{2.27}$$

$$k_v = \frac{kK}{\sqrt{d}\left(\sqrt{\alpha-\alpha^2} + 0{,}8\beta\sqrt{\frac{1}{\alpha}-\alpha^2}\right)} \tag{2.28}$$

In the factor k_v parameter k is present to fit this theoretical expression on experimental results of test on notched beams.

The factor K is calculated by Larsen and Gustafsson (1992) with the use of material values from NEN-EN 338 (2016) and additional tests. Nine test series were done, the average value found in these nine test series is $K = 5.18\sqrt{mm}$. For solid timber a K value of 5 is used with $k = 1$.

To make this expression also useful for tapered beam ends, the factor $k_i = 1.1i^{1.5}/\sqrt{d}$ from Larsen et al. (1992) is introduced. This will lead to the expression 2.29 and 2.30 found in the Eurocode 5.

$$\tau_d = \frac{1{,}5V}{bh_e} \leq k_v f_{v,k}\frac{k_{mod}}{\gamma_m} = k_v f_{v,d} \tag{2.29}$$

$$k_v = min\begin{cases} 1{,}0 \\ \frac{k_n\left(1+\frac{1{,}1i^{1{,}5}}{\sqrt{h}}\right)}{\sqrt{h}\left(\sqrt{\alpha(1-\alpha)}+0{,}8\frac{x}{h}\sqrt{\frac{1}{\alpha}+\alpha^2}\right)} \end{cases} \tag{2.30}$$

This expression contains the shear stress τ_d [N/mm^2], the shear force V_f [N] the depth of the beam b [mm] the height of the beam d [mm] the shear strength $f_{v,d}$ [N/mm^2] the inclination of the notch slope i [−] and the geometric factors α [−] and x [mm] shown in figure 2.12.

This expression makes it possible to do a unity check on the reduced shear strength. The reduction factor k_v accounts for splitting in the corner at the notch at the end of a notched beam.

2.5. The issues with the reduced shear verification in the Eurocode 5 for hardwood mortise and tenon calculation

The seemingly simple mortise tenon joint of the in between girder has multiple issues regarding the existing reduced shear strength calculation according Eurocode 5. The reduced shear calculation when used for the strength of the mortise tenon joint, has several problems. In this paragraph the problems are split in three subjects: the stress distribution in the joint, the problems surrounding the reduced shear Eurocode 5 method and the properties of the timber.

2.5.1. The stress distribution

The water pressure acting on the gate results in a shear force in the girder. The example calculation in paragraph 2.3 assumes a simple 2D force distribution to get the stress distribution. The shear stress is transmitted via the mt joint to the posts. In the mt joint the biggest part of this shear stress will be transmitted via the timber mt joint. Depending on the normal force in the beam, a part of the shear stress can also be transmitted via friction of the chests. The steel parts and the pegs are not used to transfer shear stress. Figure 2.21 shows an overview of some possible stresses in the mt joint due to water pressure.

As stated before the stresses in the gate are unknown this results in a number of assumptions. It is assumed that the chests will transfer the normal compression forces. If the mt joint is in tension it is assumed that the steel fastening will transfer these forces. The mt joint are pre stressed due to the use of the timber pegs in fastening as explained in paragraph 3.2.2.

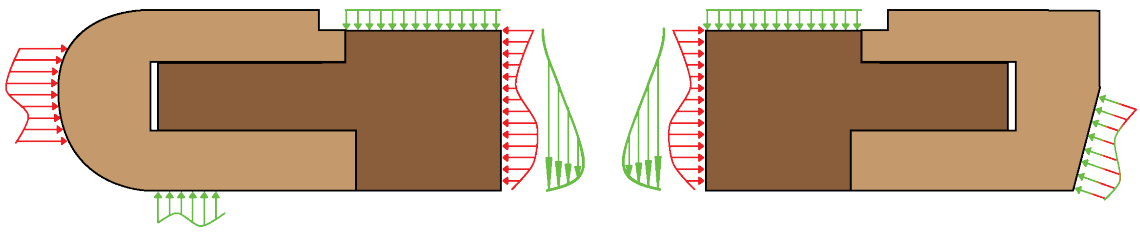

Figure 2.21: A fictional stresses distribution of the mt joint where only the water pressure is known

This pre stressing of the mt joint is not included in the stress calculations.

There is a small moment present at the tenon this is included in the existing code via the reaction force. How this moment is transferred: via the chests, tenon or both remains unknown.

How the different connection techniques transfer the different stresses due to the normal force, shear force and moment is unknown due to the complexity of the mt joint. Depending on the transfer, different stresses are present in the connection. How the normal stress is transferred in the mt joint, will have an influence on possible friction in the joint.

There is a difference between the geometry of the heel and mortise joint and the posts also have different supports. Those difference will have an influence on how the stresses in the beam are transferred to the post. How this influence occurs remains unknown.

The 3D behaviour of the mortise tenon joint is unknown. Van Otterloo (2013) made a 2D model that included 3D behaviour. He assumed that the mortise will bend under the pressure of the tenon. This bending is used to assume a unevenly distributed pressure in the mortise. If this 3D behaviour is the exact behaviour remains unknown but some kind of 3D behaviour seems possible. How the bending of the mortise, affects the tenon and the stresses in the girder is also unknown. Possible other 3D effects of post are unknown.

More knowledge of the local stresses are needed and are important for the strength verification. Without the knowledge of the stresses it is not possible to do the right verification calculations at the critical locations. How the transfer of the external forces to the supports go, remains unknown this makes it hard to make a reliable strength verification.

2.5.2. Remarks on the reduced shear verification in Eurocode 5 for hardwood mortise and tenon joint

In previews studies from Vermeij (2011) and van Otterloo (2013), is already stated that the calculation method for notched beams is not valid for tenon beams. In the explanation of the calculation method in paragraph 2.4 assumptions are made conflicting with the properties of the mt joint in mitre gates. The differences between the calculation method and used mt joints can be split in two parts. Part one use of hardwood instead of softwood. The second part explains the difference between a notched and a tenon beam.

In paragraph 2.4.5 is explained how Larsen and Gustafsson (1990) found the fracture energy perpendicular to the grain on softwood. A linear relation is assumed with the use of a linear regression in a scatter plot shown in graph 2.19. This study treats different European softwood species as if they are one species. This made it possible to find one linear relation. The graph 2.20 already show de boundaries of the linear relation of 300 kg/m^3 to 800 kg/m^3. The assumptions made in this study are not valid for the azobé timber (D70) used in the gate. The mean density of D70 is 900 kg/m^3 this is outside of the boundaries of the graph and azobé is a non European hardwood. This means that this assumed linear relation for European softwood should not be used to obtain the fracture energy of azobé, this makes the fracture energy an unknown material property.

To derive the exact equation in the Eurocode 5 factor K is introduced. This factor K is dependent on the $G_{f,y}$, E_x and f_v where $G_{f,y}$ is found with the linear equation from Larsen and Gustafsson (1990). The Eurocode 5 prescribes the value of $K = 5\sqrt{mm}$. This value is for softwood. This value should not be used in the case of a hardwood.

As explained in paragraph 2.4. The Eurocode 5 reduced shear verification is based on Gustafsson (1988). The strength of

the notched beam is found with linear crack behaviour. The geometry of a tenon beam differs from a notch beam. If a tenon is used, an assumed equivalent notch geometry is used this is shown in figure 2.9.

The study of Gustafsson (1988) is based on fracture energy. The fracture energy uses the displacements to calculate the strength; those displacements are based on the geometry of the notch. The displacement is found, using two differential equations for shear and bending and the displacement due to a fictional rotational spring. The two differential equations, use the geometry of a notched beam to obtain the shear and bending displacement. This is not correct for a tenon beam. Equation 2.7 is only valid for a constant shear force along the beam. In the case of a lock gate a distributed force due to the water pressure is present on the tenon beam, this will change the outcome of the differential equation.

The stress distribution of the tenon on the mortise is unknown. The Eurocode 5 assumes a point load at the notch, it is highly unlikely that the pressure distribution between the tenon and the mortise will be so local that is can be simplified as a point load. The other connection methods, the bolts and pegs in the mt joint are not included in existing verifications how this will have an influence on the strength of the joint remains unknown.

The fracture mode assumed for a notched beam is based on the fact that the notch is on the tension height of the beam. In a tenon beam there are chests present on both highs of the beam. The tenon in the tenon beam can be on the tension and compression height of the beam. For a tenon beam both modes and combined modes should be investigated. What kind of fracture mode to use, remains unknown. The reduced shear calculation method in the Eurocode 5 assumes fracture in the notch, only considering fracture mechanics 1 as in figure 2.19.

2.5.3. Unknown material properties of hardwood

The material properties of hardwood are given in NEN-EN 338 (2016). Not al the material properties that are needed for the calculation of mortise tenon joint are given by this standard. There are some doubts on properties given in this standard for D70. Some properties are doubtful or missing: shear strength, rolling shear strength, fracture energy perpendicular to the grain and fracture energy parallel to the grain.

According the Eurocode 5 NEN-EN 1995-1-1 (2005) rolling shear strength is twice the tensile strength perpendicular to the grain. This is based on Blass and Görlacher (2000) . This is for European spruce, not for hardwood.

Already in the example calculation 2.2 the shear strength value from NEN-EN 338 is changed to $f_{v,k} = 13,5\ N/mm^2$. This shear strength value follows from van de Kuilen and Leijten (2002). In Ravenshorst and Gamper (2016) is written that no tests according the NEN-EN 408 (2012) have been preformed on tropical hardwood. Ravenshorst and Gamper (2016) did tests according NEN-EN 408 (2012) on massaranduba, a tropical hardwood. There was found that the values given in NEN-EN 338 are an underestimation of tropical hardwood shear strength. The value of $f_{v,k} = 13,5\ N/mm^2$ of van de Kuilen and Leijten (2002) is obtained via a 5-point bending test on azobé and not via NEN-EN 338 (2016). The value $f_{v,k} = 13,5\ N/mm^2$ is used because, the value $f_{v,k} = 5\ N/mm^2$ from the NEN-EN 338 (2016) is an underestimation and not obtained from azobé.

2.5.4. Observations on the reduced shear notch verification for a hardwood mortise and tenon joint

All the previous remarks show that the verification method in the Eurocode 5 is not suitable for hardwood mortise and tenon joints. When the notched beam verification is used for the mt joint an oversimplification of this connection is made that is not correct. A simple strength verification for a mt joint in a mitre gate does not exist. How exactly the mt joint works is unknown and this makes it impossible to calculate the strength. With centuries of building experience and no recorded failure of mt joints in lock gates, it is assumed that this constructing practise is probably safe, without completely understanding the joint. In the next chapters there is an attempt to to extend the knowledge of the inner workings of a hardwood mortise and tenon joint in a mitre gate.

3

Force distribution and strength

At first an analytical analysis is done before starting the finite element modelling. Rough calculations are done to get an idea and a feeling for the force distribution in the joint. The joint is made up of several different connection methods. A total view is only possible when understanding each connection method on its own and understanding how they influence each other. In this chapter, after discussing the overall force distribution, the joint is split into three individual connection methods: the bolted steel connection, the peg connection and the mortise and tenon joint (mt joint). The bolted steel connection and the peg are studied, explained and calculated. The behaviour of the timber mt joint is the focus of this thesis, this will get an in depth study in the next chapters, via a final element model and an analytical study on a tenon beam.

3.1. Global force distribution

External forces on the gate as well as the angle of the gate determine the reaction forces as depicted in figure 3.1. A mortise gate is subjected to different kinds of forces: its own weight, forces resulting from static water pressure, waves, collisions, forces resulting from ice formation and forces resulting from moving and installing the gates and possible clamping of foreign material between the gates and the lock in open and closed position. To simplify the forces in this thesis only static water pressure is studied. The characteristic water pressure for a gate is depending on different factors such as: location, extreme water levels and waves. The different factors are combined with different load combinations to obtain a characteristic water pressures along the height of the gate. In this thesis a constant water pressure on the girder is assumed. The forces from the static water pressure will be 35 kN/m. The force 35 kN/m corresponds with a water level difference of $h_h - h_l = 2{,}33$ m and a distance of $1{,}5$ m between the girders as shown in figure 3.2.

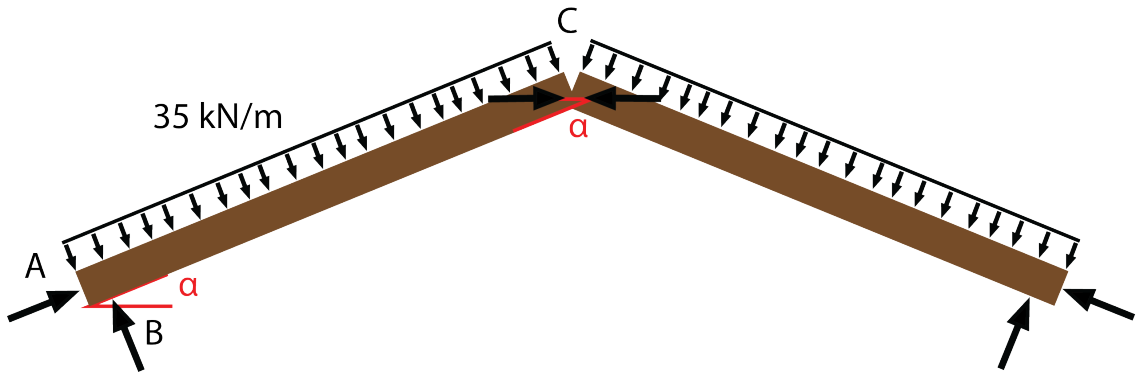

Figure 3.1: Water pressure loading on a lock gate and the support reactions, top view

3.2. Qualitative force analysis

The water pressure displayed in figure 3.2 shows the loads and the resultant load on the sheeting of the gate. The diagonal sheeting transfer, the load to the girders by bending. Because of the shape of the water pressure, the load carried by the

girders increases along the depth of the gate. The girders will carry the forces to the post by bending. The heel post will transfer the shear force via the seal strip to the lock. The mitre post will transfer the shear to the other gate, as a normal force.

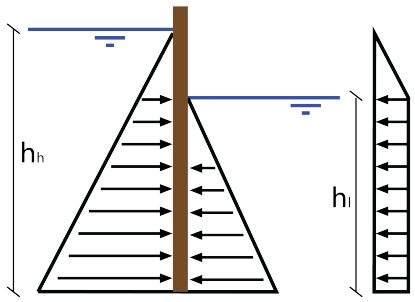

Figure 3.2: Water pressure on the lock gate, side view

Due to the angle of the mitre gate a normal force develops in the gate. This normal force is transferred via the girders to the heel post. The heel post transfers the normal force to the embedment in the lock. Possible friction forces at the embedment, the seal strip and the mitre post interface are not considered in this thesis.

The two gates are symmetrical in the middle of the lock. The other gate will be the mirror image of the calculated gate. This results in that only one gate is calculated.

To get a complete understanding of the mt joint, all the different connection methods need to be studied to know the individual behaviour of the connection. When the individual behaviour is known the whole joint needs to be studied, to see how the different connection methods work together. This total behaviour is outside of the scope of this thesis. In this chapter the individual connection methods are studied to understand their individual behaviour.

The forces due to the water pressure results in shear stresses and in normal stresses. A possible stress distribution is displayed in figure 2.2.1. Different connection methods are capable of transferring different stresses this will be explained and studied in paragraph 3.3.

The mt joint in mitre gate consist of three different connections methods, shown in 3.3.

1. The steel strip and bolt
2. The timber pegs
3. The mortise tenon joint

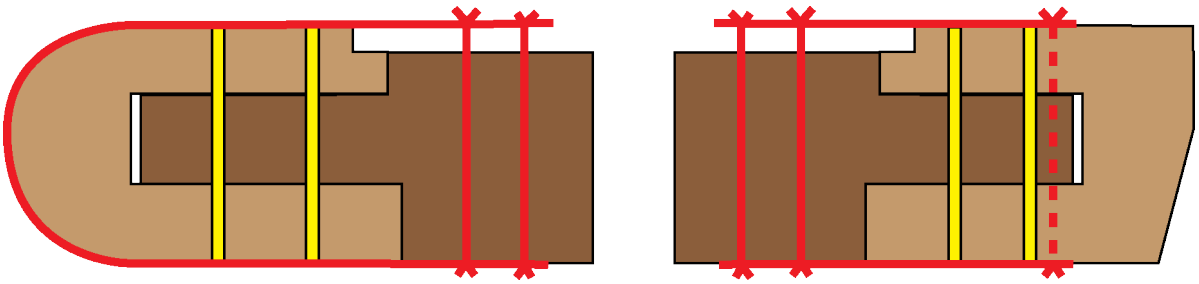

Figure 3.3: Mortise and tenon joint with without the sheeting: steel parts (red), pegs (yellow) and timber parts (brown)

3.2.1. The steel strip and bolt connection in normal tension stress

The heel post is wrapped in a steel strip connected with bolts to the girder. The mitre post is connected with steel t-strips to the girder. This connection method is only suitable to transfer normal stresses. The wrapping of the steel strip at the heel post is only used to transfer normal tension stresses. Under compression there will be no resistance because it will push the strip out of the post and possible buckle. The dimensions of the cross section for both steel strips are small, width x height $80x10\ mm$. To simplify this, the strips are only capable of transferring tension stress, under compression buckling of the strips is assumed.

In this thesis only normal compression stresses are assumed in the mt joint due to the loading case. The strength of the the steel strip and bolt connection, is calculated according the equations of Johansen in paragraph 8.2 of Eurocode 5 (2005) This strength is calculated in paragraph 3.3.3.

3.2.2. The peg in normal stress

The pegs in the mt joint are only capable of transferring normal stress in compression and tension. This transfer resembles the transfer of a steel dowel connection described in the EC 5 paragraph 8.2 with the Johansen equations. Because of the use of a peg instead of the steel dowels the equations of Johansen are not valid for this connection.

Judd et al (2011) studied the strength of timber dowel connections. This study only uses a tension tests, this neglect the possible contact pressures of the chest when a compression test is done. In the case of this mortise and tenon joint compression is present. Based on de Johansen equations in EC 5 it is assumed that the compression strength is the same as the tension strength. Keeping in mind that only the peg is considered, thus leaving out the contact pressures at the chests. Paragraph 3.3.4. studies and calculates the strength of timber pegs.

3.2.3. The mortise and tenon joint in shear and compression stress

The mortise and tenon joint is capable of transferring shear stress and normal compression stress. The tenon in the mitre gate is subjected to a shear force, a normal force and a small moment. How the transfer of these forces and moment occurs remains unknown. The used verification for a mortise and tenon joint are based on notched beams with only shear and a moment resulting from the shear. This verification is done through the reduced shear strength.

Previous studies started by using; a notched beam, because notched beams are widely studied. A notched beam is different from a tenon. Also the stresses distribution between the mortise and the tenon of the joint is unknown. More research is needed to get a better understanding. With this in mind the rough calculations in this chapter will assume a stress distribution and use the reduced shear strength for notched beams.

To get a better understanding, two extreme possible cases are used for the force distribution in the mortise and tenon joint. Also a possible 3D effect is explained and inserted in different locations to calculate the extreme stresses.

Case one

Case one assumes that a part of the shear force in the tenon beam is transferred via friction of the inside and outside chest. The other part is transferred via de tenon. The resulting shear force will result in a moment in the tenon. This moment is subtracted from the found moment to find the difference. This is transferred via an increase on the bottom and decrease on the top for the compression force in the chests. This is shown in figure 3.4.

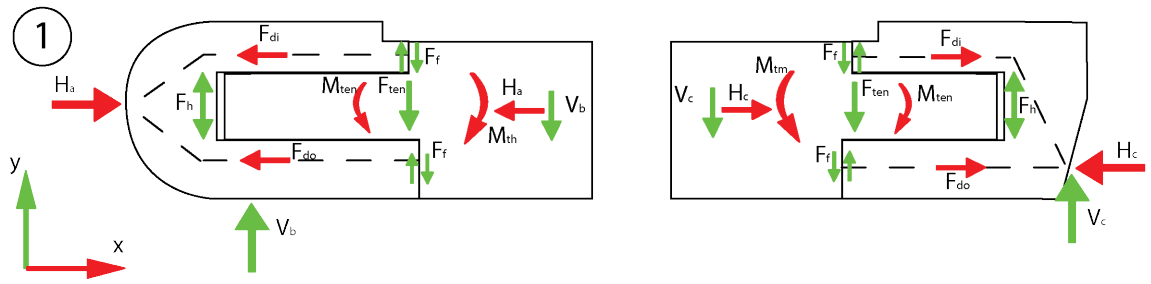

Figure 3.4: Case 1 in the heel and mitre joint

Case two

Case two assumes a clamping of the tenon in the mortise. In this case the full moment will be in the tenon, resulting in a compression stress in top back and bottom front of the mortise. Assuming that the shear force is transferred close to the edge, the bottom force is increased. Due to this compression a normal friction force is possible. This friction will result in lower compression on the inside chest, illustrated by figure 3.5.

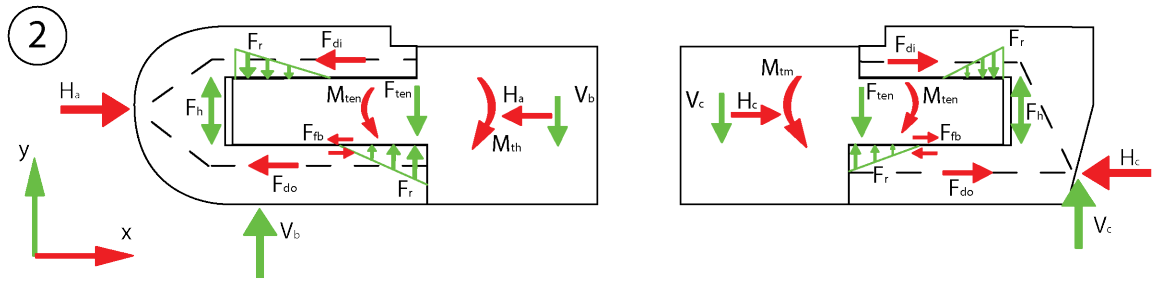

Figure 3.5: Case 2 in the heel and mitre joint

3D effect
The 3D effect assumes that the bottom part of mortise is a plate that is clamped on three sides. The result of this is that the shear force is transferred the sides of the mt joint. Displayed in figure 3.6.

The real force and stress distribution will be a combination of case one and two with an influence of the 3D effect. This combination will probably be different for the heel joint and mitre joint. The difference in the supports, geometry and force will probably result in different internal stresses between the heel and mitre joint.

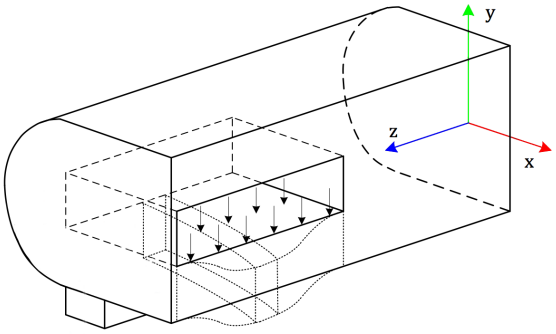

Figure 3.6: 3D effect shown in the heel joint (edited from [26], fig. 48)

3.3. Quantitative force analysis

In this paragraph calculations are made to get a feeling of the size and proportions of the forces and stresses. The verification is calculated according the Eurocode 5 (2005).

3.3.1. Reaction forces

For the simplified analysis a simple force diagram is assumed as in figure 3.7. The model is chosen on the basis, that there is no friction at the supports, the result of this is roller supports at A, B and C. The model in figure 3.7 is static determined; this results in equations, where the stiffness has no influence on the support reactions. The distributed load in this model is the result of the water pressure and assumed 35 kN/m. As shown in the figure 3.1 the angle of the gate remained variable between 15° and 30° degrees. The angle of 0° is included to calculate the behaviour of the mt joint when only a shear force is present. A gate with an angle of 0° is no a mitre gate.

Equilibrium is used to calculate the reaction forces.

1. Moment equilibrium around C

$$V_b = \frac{(0,5a_{de} + a_{ec} - 0,5\tan(\alpha_g)h_{sm})qa_{de}}{a_{db} + a_{de} + a_{ec} - 0,5\tan(\alpha_g)h_{sm}} \tag{3.1}$$

$$V_b = \frac{(0,5\cdot 3 + 0,36 - 0,5\tan(\alpha_g)0,15)35\cdot 3}{0,24 + 3 + 0,36 - 0,5\tan(\alpha_g)0,15} \tag{3.2}$$

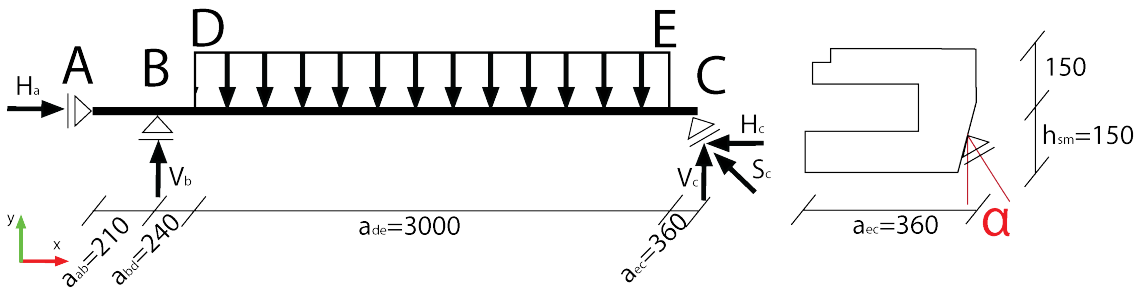

Figure 3.7: Simplified mechanical model of a lock gate and detail of the mitre support

2. Vertical equilibrium

$$V_c = q a_{de} - V_b \tag{3.3}$$

$$V_c = 35 \cdot 3 - V_b \tag{3.4}$$

3. Geometric properties of support C and horizontal equilibrium

$$H_c = H_a = \frac{V_c}{\tan(\alpha_g)} \tag{3.5}$$

4. The reaction force at C

$$S_c = H_a = \sqrt{V_c^2 + H_c^2} \tag{3.6}$$

Table 3.1 shows the forces and the moments of different gate angles. The moment line for the gate at an angle of 18,5 degrees is shown in graph 3.8 the blue line. The shear force line for the gate angle of 18,5 degrees is shown in graph 3.8 the red line.

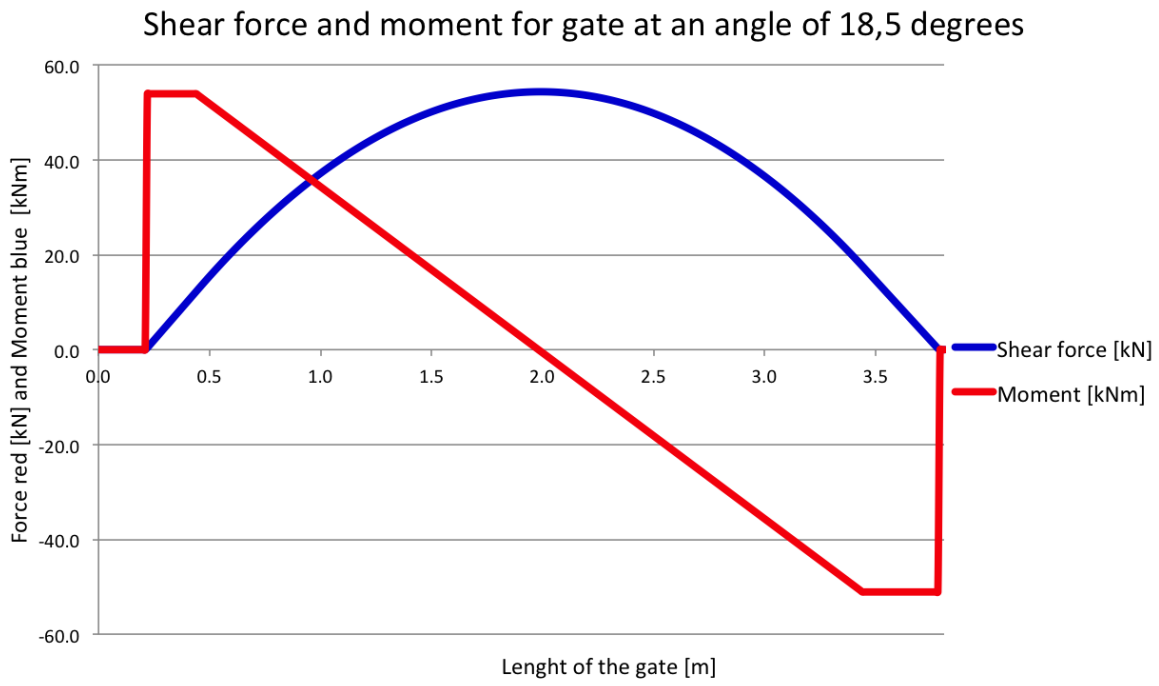

Figure 3.8: Shear force [kN] (red) and moment [kNm] (blue) for a gate at 18,5° degrees

The influence of the angle of the gate is shown in table 3.1. When the angle of the gate increases the normal force H_a and H_c in the gate lowers significant. The other forces and moment change little due to a different gate angle. The difference between the heel and mitre joint lead to different reaction forces and moments. A bigger shear force is transferred via the heel joint, while a smaller moment is present in comparison with the mitre joint.

Table 3.1: Forces and moments, overview for different gate angles

$Angle[deg]$	0°	15°	18,5°	30°
$V_b[kN]$	54,3	54,0	53,9	53,7
$V_c[kN]$	50,7	51,1	51,1	51,3
$S_c[kN]$	50,7	197,0	161,0	102,7
$H_c[kN]$	0,0	190,3	152,6	88,9
$H_a[kN]$	0,0	190,3	152,6	88,9
$M_{th}[kNm]$	12,9	12,8	12,8	12,8
$M_{max}[kNm]$	55,0	54,5	54,4	53,9
$M_{tm}[kNm]$	18,4	17,4	17,1	16,2

3.3.2. 2D force distribution inside the mortise tenon joint

The 2D force distribution for the cases and the heel and mitre joint are calculated in this paragraph. The angle of the gate is chosen 18,5° degrees.

Case independent heel post

The normal force at the support A follows directly from the global calculation and is half of H_a, $F_{di} = F_{do} = 76,3\ kN$. The shear force at the support B also follows directly from the global calculation this is $V_b = 53,9\ kN$.

Case independent mitre post

The normal force at the support A follows directly from the global calculation and is half of H_c, $F_d = F_d = 76,3\ kN$. The vertical component at the support c also follows directly from the global calculation this is $V_c = 51,1\ kN$.

Case 1 heel post

In case 1 the force distribution is calculated assuming friction at the chests of the post and the girder F_f. The tension force F_h in the post behind the mortise is the result from the change of direction of the forces F_d shown in figure 3.9. It is assumed that the normal force H_a is divided in two equal parts. This is calculated according. $F_h = 2\frac{F_d \Delta d}{\Delta b} = 2\frac{76,3 \cdot 75}{140} = 81,8\ kN$.

The maximum possible friction force F_f at the inside and outside chest is calculated with the friction coefficient of wet wood-to-wood contact with the friction coefficient $\mu = 0,2$ [15]. This will result in a maximum friction force, $F_f = 2F_d\mu = 2 \cdot 76,3 \cdot 0,2 = 30,5\ kN$. The resulting shear force in the tenon will be $F_{ten} = V_b - F_f = 53,9 - 30,5 = 23,4\ kN$. The possible 3D effect for shear force is not included.

The moment in the tenon will be equal to $M_{ten} = F_{ten}x = 23,4 \cdot 0,2375 = 5,6\ kNm$. The resulting forces due to the moment in the beam will be $\Delta F_d = \frac{(M_{th} - M_{ten})}{a_d} = \frac{(12,8-5,6)}{0,15} = 48,4\ kN$. This will lead to a decrease in the inside chest compression force $F_{di} = F_d - \Delta F_d = 76,3 - 48,4 = 27,9\ kN$. This will lead to a increase in the outside chest compression force $F_{do} = F_d + \Delta F_d = 76,3 + 48,4 = 124,6\ kN$. An overview is given in table 3.2.

Case 1 mitre post

In case 1 in the mitre post assumes the maximum friction force F_f at the chests, $F_f = 2F_d\mu = 2 \cdot 76,3 \cdot 0,2 = 30,5\ kN$. The resulting shear force in the tenon will be $F_{ten} = V_b - F_f = 51,0 - 30,5 = 20,5\ kN$. The possible 3D effect for shear force is not included.

The moment in the tenon will be equal to $M_{ten} = F_{ten}(d - 0,5\tan(\alpha_g)0,15 = 20,5 \cdot (0,36 - 0,5\tan(18,5)0,15) = 6,9\ kNm$. The resulting forces due to the moment in the beam will be $\Delta F_d = \frac{(M_{tm} - M_{ten})}{a_d} = \frac{(17,1-6,9)}{0,15} = 68,2\ kN$. This will lead to a decrease in the inside chest compression force $F_{di} = F_d - \Delta F_d = 76,3 - 69,9 = 8,1\ kN$. This will lead to an increase in the outside chest compression force $F_{do} = F_d + \Delta F_d = 152,6 + 69,9 = 144,5\ kN$.

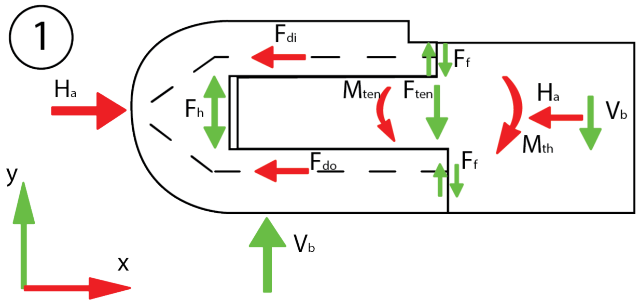

Figure 3.9: Case 1 forces for the heel post

Table 3.2: Case 1 forces for the heel post

Name	Value
V_b	53,9 kN
F_h	81,5 kN
F_f	30,5 kN
F_{ten}	23,4 kN
M_{ten}	5,6 kNm
F_{di}	27,9 kN
F_{do}	124,6 kN

The tension force F_h in the post behind the mortise is the result from the change of direction of the force F_{di} this is calculated according. $F_h = \frac{F_d \Delta d}{\Delta b} = \frac{6{,}3 \cdot 150}{120 - 0{,}5 \cdot 150 \cdot \tan(18{,}5)} = 12{,}8\ kN$. An overview is given in table 3.3.

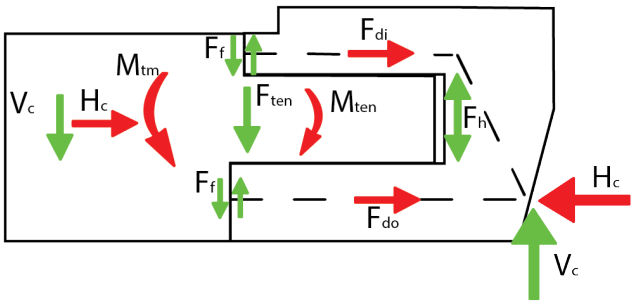

Figure 3.10: Case 1 forces for the mitre post

Table 3.3: Case 1 forces for the mitre post

Name	Value
V_c	51,1 kN
F_h	12,8 kN
F_f	30,5 kN
F_{ten}	20,5 kN
M_{ten}	6,9 kNm
F_{di}	8,1 kN
F_{do}	144,5 kN

Case 2 heel post

Case two assumes that the total moment is transferred via clamping in the mortise. The shear force in this case is transferred completely through the tenon, without a possible 3D effect, there is no friction at the chests. Due to the high shear force a friction force in the mortise is present. This friction will transfer a part of the normal force.

The shear force in the tenon equals the support reaction $F_{ten} = 53{,}9\ kN$. The moment in the tenon becomes $M_{ten} = M_{th} = 12{,}8\ kNm$. The moment in de tenon will be clamped in the mortise. This clamping results in a force on the top at the back of the mortise $F_r = M_{ten} a = \frac{12{,}8}{0{,}184} = 69{,}6\ kN$. On the bottom of the mortise the same force is present as a result of the moment in the tenon. Due to this force F_r and the force in the tenon F_{ten} a maximum friction force is possible, $F_{fb} = (F_r + F_{ten})\mu = (69{,}6 + 53{,}9)0{,}2 = 24{,}7\ kN$. This friction force will act on the outside chest and increase F_{do}, it will lower the inside chest F_{di}, $F_{di} = F_d - F_{fb} = 51{,}6\ kN$ $F_{do} = F_d - F_{fb} = 101{,}0\ kN$. F_d remains the same value thus F_h will be the same as in load case 1 $F_h = 81.8\ kN$. An overview is given in table 3.4.

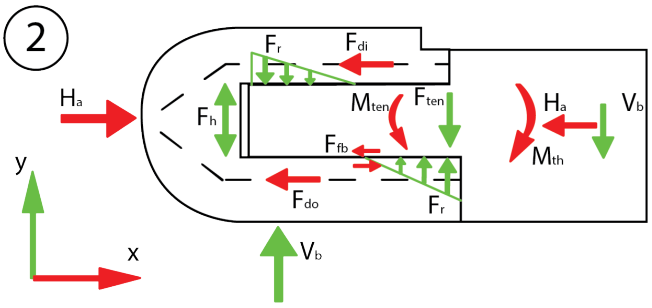

Figure 3.11: Case 2 forces for the heel post

Table 3.4: Case 2 forces for the heel post

Name	Value
V_b	53,9 kN
F_{ten}	53,9 kN
M_{ten}	12,8 kNm
F_r	69,6 kN
F_{fb}	24,7 kN
F_{di}	51,6 kN
F_{do}	101,0 kN
F_h	81,8 kN

Case 2 mitre post

The shear force in the tenon is equal to the support reaction $F_{ten} = 51,1\ kN$ in case 2 for the mitre post.

The moment in the tenon becomes $M_{ten} = M_{tm} = 17,1\ kNm$. The moment in de tenon will be clamped in the mortise. This clamping results in a force on the top at the back of the mortise $F_r = \frac{M_{ten}}{a} = \frac{17,1}{0,144} = 118,8\ kN$. On the bottom at the entrance of the mortise, the same force is present as a result of the moment in the tenon. Due to this force F_r and the force in the tenon F_{ten} the maximum friction force possible is $F_{fb} = (F_r + F_{ten})\mu = (118,8 + 51,1)0,2 = 34,0\ kN$. The friction force will lower the forces in the inside chest F_{di} and increase the forces in the outside chest F_{do}, $F_{di} = F_d - F_{fb} = 42,3\ kN$ $F_{do} = F_d - F_{fb} = 85,0\ kN$. The force on the inside chest F_{di} needs to change from direction to go to the support, this results in the tension force $F_h = F_{di}\frac{\Delta d}{\Delta b} = 42,3 \cdot \frac{150}{120-0,5\cdot 150 tan(18,5)\cdot} = 66,9\ kN$. An overview is given in table 3.5.

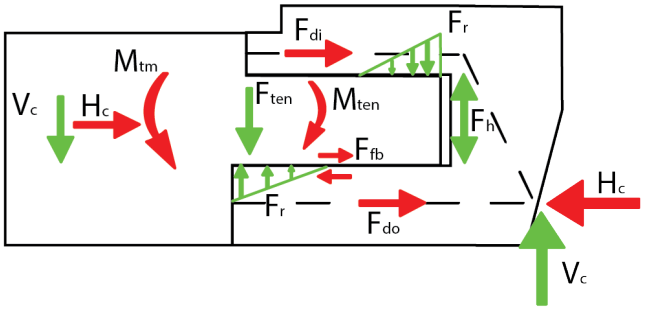

Figure 3.12: Case 2 forces for the mitre post

Table 3.5: Case 2 forces for the mitre post

Name	Value
V_c	$51,1\ kN$
F_{ten}	$51,1\ kN$
M_{ten}	$17,1\ kNm$
F_r	$118,8\ kN$
F_{fb}	$34,0\ kN$
F_{di}	$42,3\ kN$
F_{do}	$85,0\ kN$
F_h	$66,9\ kN$

Observations for the two cases

The two different cases show different force distributions, without the 3D effect. In reality it will be a combination of both cases and some 3D effects. The different support reaction and the different geometry between the heel and mitre post result in different forces between the joints. In the paragraph 3.3.5. the stresses from these forces are calculated and verified according the Eurocode 5.

3.3.3. Strength of the bolted steel strip

The force that is present in the bolted connection is unknown. The strength is calculated to obtain the maximum possible strength of the bolt as a size indication of the maximum posible stresses. The tension strength of the bolted steel strip connection is well known and is described in the Eurocode 5 paragraph 8.2.2. This calculation method includes two different failure mechanics for thin steel plates as outer members of a double shear connection. The plate is thin if $t_1 \leq 0,5d$, t_1 is 10 mm the diameter of the bold d is 20 mm this means that this is a thin steel plate. The failure mechanisms are shown in figure 3.13 and 3.14. Failure A is a failure due to exceeding the embedment strength of the timber matching with the formula 3.7. Failure B is failure due to development of plastic hinges in the bolt matching with formula 3.8. The smallest value is the strength of the bolted connection. The strength calculation according the NEN1995-1-1 formula (8.12) [3] are written in equation 3.7 and 3.8.

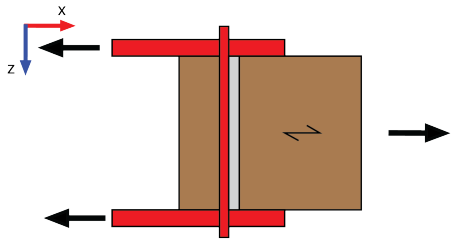

Figure 3.13: Failure mode A

$$F_{v,Rk} = 0,5 f_{h,2,d}\, t_2 d \tag{3.7}$$

$$F_{v,Rk} = 1,15\sqrt{2M_{y,Rk} f_{h,2,d} d} + \frac{F_{ax,Rk}}{4} \tag{3.8}$$

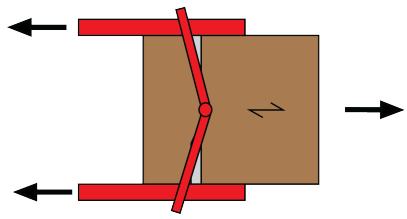

Figure 3.14: Failure mode B

Where $F_{v,Rk}$ $[N]$ is the characteristic load carrying capacity per shear plane per fastener; $f_{h,2,d}$ $[N/m^2]$ is the characteristic embedment strength in the timber member; t_2 $[mm]$ is the thickness of the timber; d $[mm]$ is the fastener diameter; $M_{y,Rk}$ $[N/mm]$ is the characteristic fastener yield moment; $F_{ax,Rk}$ $[N]$ is the characteristic withdrawal capacity of the fastener for a bolt.

$$M_{y,Rk} = 0,3 f_{u,k} d^{2,6} \tag{3.9}$$

$$F_{ax,Rk} = 0,25 \cdot 1,15 \sqrt{2 M_{y,Rk} f_{h,2,d} d} \tag{3.10}$$

Where $M_{y,Rk}$ $[Nmm]$ is the characteristic fastener yield moment; $f_{u,k}$ $[N/mm^2]$ is the characteristic tensile strength; d $[mm]$ is the bolt diameter.

The bolt diameter is 20 mm with tension strength of 800 N/mm^2. This will lead to a $M_{y,Rk}$ value of $5,8e+05$ Nmm. The embedment strength parallel to the fibre in the girder for azobé is $59,0$ N/mm^2 via equation 3.11. The embedment strength perpendicular to the fibre in the post for azobé is $49,2$ N/mm^2. This value is found using the equation 3.12. Using the prescribed formulas the strength of the bolt is found and shown in table 3.6. The embedment force for the girder and post are the same because of the same embedment thickens ratio $f_{h,2,90,d}\, t_{2,p} = f_{h2,0,d}\, t_{2,g}$ is $49,2 \cdot 300 = 59,0 \cdot 250$.

$$0,082(1 - 0,01d)\rho = f_{h,2,0,d} \tag{3.11}$$

$$f_{h,2,90,d} = \frac{f_{h,2,0,d}}{(0,9 + 0,0015d)\sin^2(90) + \cos^2(90)} \tag{3.12}$$

Table 3.6: Tension strength of the bolt

Girder connection		
Embedment (a)	295,2	Kn per bolt
Plastic bolt (b)	90,4	Kn per bolt
Post connection		
Embedment (a)	295,2	Kn per bolt
Plastic bolt (b)	82,5	Kn per bolt

The tension strength of the steel strip bolt connection, in the mitre joint is the amount of bolts times the minimum strength in table 3.6. The result is three bolts with $247,5$ kN. The force of $247,5$ kN is the tension strength for the steel t-strip connection in the mitre joint. It is the maximum force under full tension of the joint. The strength of the steel strip is not calculated, but is important for the strength of the total connection. The compression stress is not calculated, this will be lower or the same as the tension stress depending on possible buckling of the steel strip. This constant stress does not occur in the loading case studied in this thesis.

The strength of the blotted strip connection in the heel joint is different because the wrapping of the steel strip. The width of the steel strip is 80 mm this is wrapped around the circular back of the heel post. The length of the wrap parallel to the force is 300 mm. The area of the steel strip wrap is $80 \cdot 300 = 24000$ mm^2. The embedment strength will be $49,20 \cdot 24000 = 1181$ kN this is higher than the strengths in in table 3.6. The tension strength of the steel strip bolt connection in the heel, is three times the strength of the plastic bolt failure in the girder $90,4$ kN. The full tension strength is $271,2$ kN. The strength of the steel strip in not calculated. Due to the shape of the steel strip at the heel joint, compression is not possible.

3.3.4. Strength of the peg connection

The force on the peg connection is unknown. The strength is calculated to get a size indication of the maximum strength posible in the peg. Several studies in the strength of the timber dowel connections are done in the context of a mortis tenon joint in tension. The timber dowel connection is capable of transvering normal compression force, when the contact forces are neglected. In the study: Tensile strength of varied-angle mortis and tenon connections in timber frames by Judd J. et al. (2011) failure modes for pegs are described. The described failure modes are described for tension, those failure modes are the same in compression, with the assumption that there will be no contact forces present. The failure modes in the Eurocode 5 paragraph 8.2.2. G, H, J and K are the same as for the steel dowel. Some changes are made for the use of the peg, this is explained for all the individual failure modes. A fifth failure mode, shear failure of the peg is included. The smallest strength is the strength of this peg connection.

Failure mode G

Failure mode G is the embedment of the timber in the mortise and the embedment of the peg along the thickness of the mortise shown in figure 3.15. Both the mortise and the peg are loaded perpendicular to the fibre. The embedment for the peg and the mortise are the same because they are both in timber class D70. The embedment strength is calculated according the formula 3.13 with $f_{h,90,d} = 29,5\ N/mm^2$ obtained using equations 3.11 and 3.12, $d = 40\ mm$ and $t_m = 100\ mm$. The failure through mode G is $236,2\ kN$ per peg for both the mortise and the peg.

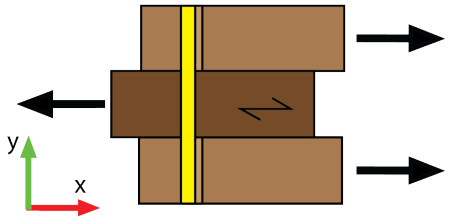

Figure 3.15: Failure mode G

$$F_g = 2 t_m f_{h,90,d} d \tag{3.13}$$

Failure mode H

Failure mode H is the embedment of the timber in the tenon and the embedment of the peg along the thickness of the tenon displayed in figure 3.16. The peg is loaded perpendicular to the fibre while at the tenon it is parallel to the fibre. According equation 3.11 and 3.12 the embedment strength is $f_{h,90,d} = 29,5\ N/mm^2$ for the peg, while it is $f_{h,0,d} = 44,3\ N/mm^2$ for the tenon. The failure trough mode H for the peg is $118,1\ kN$ per peg the failure in the tenon is $177,1\ kN$ per peg. Both are calculated according equation 3.14, with $t_t = 100\ mm$ and $d = 40\ mm$.

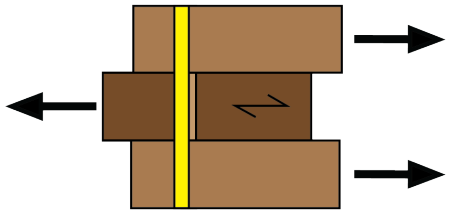

Figure 3.16: Failure mode H

$$F_h = t_t f_{h,\alpha,d} d \tag{3.14}$$

Failure mode J

Failure mode J is the failure due to bending failure of peg with one hinge. This hinge happens in the middle of the tenon. The strength of this failure is derived using moment equilibrium around the middle point at the hinge in figure 3.17. To calculate the resulting force $F_j = f_{h,90,d} b_2 d$ the following assumptions are made: $\beta = \frac{f_{h,90,d}}{f_{h,0,d}}$, $a_2 = \frac{t_2 - b_2}{2}$ and $b_1 = \frac{t_1}{2}$. Half a moment is present in the peg, this moment is the failure moment of the peg this is calculated by equation 3.15 here

$f_{md} = 70\frac{k_{mod}}{\gamma_m} = \frac{70 \cdot 0,5}{1,3} = 26,9\ N/mm^2$ for the lock gate. The maximum moment in the peg will be $0,2\ kNm$. The moment equilibrium around the middle of the peg is equation 3.16 this equation is solved for b_2, this shows in equation 3.17 and then substituted in the equation for F_j. Using the known geometric properties and multiplying it with two, a strength of $92,6\ kN$ per peg is obtained for failure mode J.

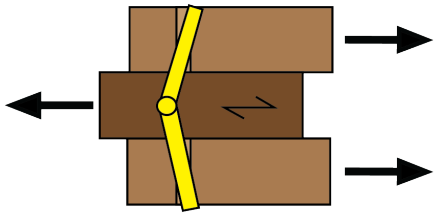

Figure 3.17: Failure mode J

$$M_{y,h} = f_{m,d}\frac{\pi d^3}{32} \tag{3.15}$$

$$0 = \frac{-M_{y,h}}{2} + d\left(\frac{-f_{h,0,d}t_1^2}{8} + \beta f_{h,0,d} b_2\left(\frac{b_2}{2} + \frac{t_1}{2}\right) + \beta f_{h,0,d}\left(\frac{t_2}{2} - \frac{b_2}{2}\right)\left(\frac{t_2}{4} + \frac{3b_2}{4} + \frac{t_1}{2}\right) - \beta f_{h,0,d}\left(\frac{t_2}{2} - \frac{b_2}{2}\right)\left(\frac{3t_2}{4} + \frac{b_2}{4} + \frac{t_1}{2}\right)\right) \tag{3.16}$$

$$b_2 = \frac{1}{2\beta d f_{h,0,d}}\left(-2\beta d f_{h,0,d} t_1 - 2\beta d f_{h,0,d} t_2 + \sqrt{4\beta^2 f_{h,0,d}^2 t_1^2 + 8\beta^2 f_{h,0,d}^2 t_1 t_2 + 8\beta^2 f_{h,0,d}^2 t_2^2 + 2\beta f_{h,0,d}^2 t_1^2 + 8M_{yh}\beta d f_{h,0,d}}\right) \tag{3.17}$$

Failure mode K

Failure mode K is the failure due to bending failure of peg with three hinges. One hinge happens in the middle of the tenon the other two hinges occur in the mortise. The strength of this failure is derived using moment equilibrium around middle of the peg in figure 3.18. To calculate the resulting force $F_k = f_{h,90,d} b_2 d$ the following assumptions are made: $\beta = \frac{f_{h,90,d}}{f_{h,0,d}}$ and $b_1 = \frac{t_1}{2}$. Figure 3.18 shows the hinges at the circles. There are the moments present in this failure mode. The failure moments of the peg is calculated by equation 3.15 for the lock gate. The moment in the middle of the tenon is half of the maximum moment, just as in failure mode J. The maximum moment in the peg is the same as in failure mode J $0,2\ kNm$. The moment equilibrium around middle of the peg is formula 3.18 this equation is solved for b_2 in formula 3.19 and then substituted in the equation for F_k. Using the known geometric properties and multiplying it with two, a strength of $15,9\ kN$ per peg is obtained for failure mode K.

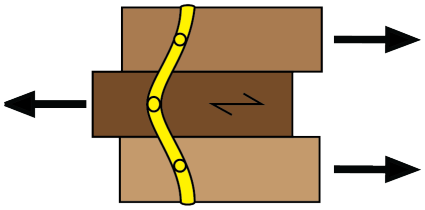

Figure 3.18: Failure mode K

$$0 = \frac{-3M_{y,h}}{2} + \beta f_{h,0,d} d b_2\left(\frac{t1}{2} + \frac{b_2}{2}\right) - \frac{f_{h,0,d} d t_1^2}{8} \tag{3.18}$$

$$b_2 = \frac{-\beta d f_{h,0,d} t_1 + \sqrt{\beta^2 d^2 f_{h,0,d}^2 t_1^2 + \beta d^2 f_{h,0,d}^2 t_1^2 + 12 M_{y,h}\beta d f_{h,0,d}}}{2\beta d f_{h,0,d}} \tag{3.19}$$

Failure mode peg shear
The shear capacity of the peg is calculated, this is an extra failure mode, in comparison to the steel dowels. This failure mode is caused by the shearing of the peg over its two cross sections shown in figure 3.19. The shear strength for D70 timber is $f_{v,d} = 5\frac{k_{mod}}{\gamma_m}$ in the case of the lock gate $f_{v,d} = 1.9\ N/mm^2$. The diameter of the peg is 40 mm this results in a strength of $3,6\ kN$ per peg for shear failure. This is calculated using the shear strength of a circular cross section shown in equation 3.20, the failure force is calculated with $t_v = f_{v,d}$ this leads to equation 3.21.

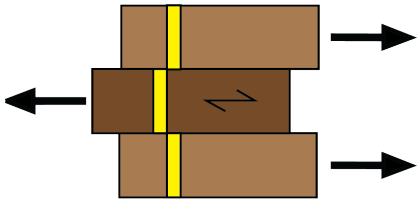

Figure 3.19: Failure mode shear

$$t_v = \frac{VS}{Ib} = \frac{V\left(\left(\frac{\pi r^2}{2}\right)\frac{4r}{3\pi}\right)}{\left(\frac{\pi r^4}{4}\right)2r} = \frac{4V}{3\pi\,(0,5d)^2} \tag{3.20}$$

$$F_{shear} = 2\frac{3}{4}f_{v,d}\pi\,(0,5d)^2 \tag{3.21}$$

The strength of the peg
The smallest strength of the five failure modes govern the strength of this connection, this is the shear failure of the peg. All the values of the failure mechanisms are shown in table 3.7. The connection uses two pegs per connection, the total strength will be $2 \cdot 3,6 = 7,2\ kN$. This strength can be in tension and in compression when neglecting the contact forces. The strength is a small in comparison with the bolt strength and the forces in the gate. In the construction method the pegs are used to pretension the connection. The maximal possible pretension before failure of the pegs is $7,3\ kN$ for two pegs. The true pre tension force due to the use of the pegs in the connections remains unknown. How the pretension influence the strength of the peg connection remains unknown.

Table 3.7: Compression and tension strength of the peg connection

	Joint	Peg	
Failure mode G	236,2	236,2	kN per peg
Failure mode H	177,1	118,0	kN per peg
Failure mode J		92,6	kN per peg
Failure mode K		18,9	kN per peg
Failure mode peg shear		3,6	kN per peg

3.3.5. Strength of the mortise and tenon joint
The strength of a mortise and tenon joint in shear and compression is unknown. In this paragraph individual locations are verified according the Eurocode 5. Also different studies are done on the strength of a tenon beam and on the strength of the mortise and tenon joint connection.

One study focused the difference of a notch beam and a tenon beam under shear by Vermeij (2011). An other research was done on the force distribution and connection strength in timber lock gates by van Otterloo (2013). This research contained a 2D final element model to get a bigger knowledge in the strength and stress distribution of the joint.

In “Pen gat verbinding” (Mortise and tenon joint) Vermeij (2011) looked at the behaviour of a tenon beam compared to a notched beam made of hardwood (azobé) and softwood (pine) by doing tests.

Vermeij stated that the tenon beam has different behaviour than a notched beam. The calculation method based on a notched beam is not valid, the tenon beam is much stronger than a notched beam. The extra material that is present above the tenon makes it not suitable to calculate a tenon beam to an equivalent notched beam as in figure 2.8. It is concluded that the rules according the Eurocode 5 NEN-EN 1995-1-1 (2005) paragraph 6.5.2. should not be used for the

tenon beam. This is because the calculations are based on softwood notched beams and this is not valid for a hardwood tenon beams. This is also the conclusion of chapter 2.

The research of van Otterloo (2013) stated that a closer look was needed at the mt joint's 3D behaviour. In the 2D model of his research, 3D behaviour was included. The 3D final element model in this thesis is used to study if there is a 3D behaviour in the mortise.

The previous studies and the explanation of the Eurocode 5 paragraph 6.5.2. in chapter 2 shown, that the reduced shear method based on notched beams is not the right verification method for a mortise and tenon joint.

This paragraph uses the forces calculated in paragraph 3.2, for a rough calculations as an indication of the strength of the mt joint. The material properties that are used for the rough calculations are in table 3.8 the values are from NEN-EN 338 (2016) the values are calculated according $f_d = k_{mod} \frac{f_k}{\gamma_M}$. The calculation method and the values are from the EC 5 and NEN-EN 338 (2016) this means that the reduced shear method and the shear value are used. While they are possibly not right for azobé mt joint. All the checks are done for a gate angle of $18,5°$ degrees.

Table 3.8: Design strength properties for D70

Name	symbol	value	unit
Partial material factor	γ_M	1,3	–
Modification factor	k_{mod}	0,50	–
Bending	$f_{m,d}$	26,92	N/mm^2
Tension parallel	$f_{t,0,d}$	16,15	N/mm^2
Tension perpendicular	$f_{t,90,d}$	0,23	N/mm^2
Compression parallel	$f_{c,0,d}$	13,08	N/mm^2
Compression perpendicular	$f_{c,90,d}$	5,19	N/mm^2
Shear	$f_{v,d}$	1,29	N/mm^2
Rolling shear	$f_{v,r,d}$	0,46	N/mm^2

The locations of the verifications are shown per verification by a small illustration. The compression stresses perpendicular at the fibre will spread, as is show in figure 3.20 over an effective length. The effective length for the post will be bigger than the initial width of 250 mm. This effective length is calculated by $l_{ef} = l + \frac{h}{3}$ from paragraph 6.1.5. of Eurocode 5 (2005). This distance is included in the tables and named h.

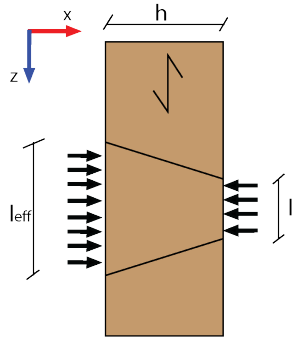

Figure 3.20: Spread of the load parallel to the fibre

Compression at the back heel post, location 1

The compression at the back of the heel post is case independent, this is validated for compression $\frac{F_a}{A} \leq f_{c,90,d}$. Table 3.9 shows the validation for this location the unity check is valid.

Compression at the strip of the heel post, location 2

The compression at the strip of the heel post is case independent, this is validated for compression $\frac{F_b}{A} \leq f_{c,90,d}$. Table 3.10 shows the validation for this location, the unity check is valid.

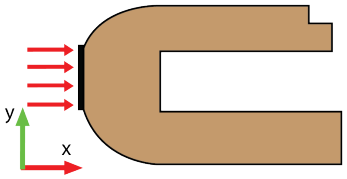

Figure 3.21: Location 1 in the heel post

Table 3.9: Compression at location 1 in the heel post, for case 1 and 2

	Heel post	Unit
$x = h$	450	mm
y	125	mm
$z = l_{ef}$	400	mm
$A = yz$	50000	mm^2
$F_a = H_a$	152,6	kN
$\sigma_{c,1}$	3,0	N/mm^2
$f_{c,90,d}$	5,2	N/mm^2
Unity check	59%	–

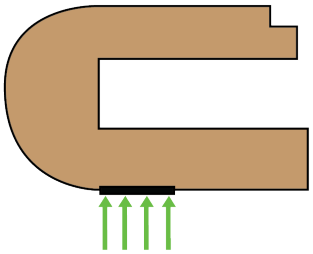

Figure 3.22: Location 2 in the heel post

Table 3.10: Compression at location 2 in the heel post, for case 1 and 2

	Heel post	Unit
x	125	mm
$y = h$	100	mm
$z = l_{ef}$	158,3	mm
$A = xz$	19791,7	mm^2
$F_b = V_b$	53,9	kN
$\sigma_{c,2}$	2,7	N/mm^2
$f_{c,90,d}$	5,2	N/mm^2
Unity check	52%	–

Compression at the support of the mitre post, location 3

The compression at support C in the mitre post is case independent, it is validated for compression $\frac{F_c}{A} \leq f_{c,90,d}$. The angle of the force to the fibre remains 90° degrees independent of the angle of the gate, because the force is acting on the transverse plane. Table 3.11 shows the validation for this location where the unity check is valid.

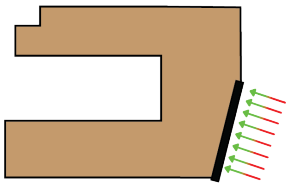

Figure 3.23: Location 3 in the mitre post

Table 3.11: Compression at location 3 in the mitre post, for case 1 and 2

	Mitre post	Unit
$x = h$	360	mm
$y = 150\tan(18,3)$	157,17	mm
$z = l_{ef}$	370	mm
$A = yz$	58522,9	mm^2
$F_c = S_c$	161,0	kN
$\sigma_{c,3}$	2,8	N/mm^2
$f_{c,90,d}$	5,2	N/mm^2
Unity check	53%	–

Tension behind the mortise, location 4

The tension just behind the mortise is caused by changing the direction of the compression force to the support. This force is case independent, but is different for the heel and mitre post by $\frac{F_h}{A} \leq f_{t,90,d}$. The value for the depth x is estimated at $\frac{2}{3}$ of the material thickens that is present. The width $z = 250\ mm$ is used this is the same as the width of the mortise. Table 3.12 shows the verification for this location, the unity checks are way too high.

Compression and shear at the inside chest, location 5

The compression stress at the inside chest is calculated for case 1 and 2. For case 1 the shear stress due to friction is calculated. This force is case dependent and different for the heel and mitre post for compression is used $\frac{F_{di}}{A} \leq f_{c,90,d}$, for shear is used $\frac{3F_{f,5}}{2A} \leq f_{v,r,d}$. Table 3.13 shows the verification for this location, the unity checks in the heel post for case 1 are too high.

Compression and shear at the outside chest, locations 6

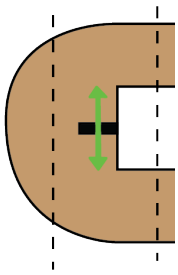

Figure 3.24: Location 4 in the heel and mitre post

Table 3.12: Tension at locations 4

	Heel post	Mitre post		
	case 1 and 2	case 1	case 2	Unit
x	93,3	73,3		mm
z	250	250		mm
$A = xz$	23333,3	18333,3		mm^2
F_h	81,8	12.8	66.9	kN
$\sigma_{t,4}$	3,5	0,7	3,7	N/mm^2
$f_{t,90,d}$	0,2	0,2		N/mm^2
Unity check	1519%	304%	1587%	–

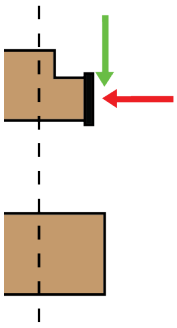

Figure 3.25: Location 5 in the heel and mitre post

Table 3.13: Compression and shear at locations 5

	Heel post		Mitre post		
	Case 1	Case 2	Case 1	Case 2	Unit
y	50		50		mm
z	250		250		mm
$A = yz$	12500		12500		mm^2
F_{di}	28,0	51,6	8,1	42,3	kN
$F_{f,5} = F_{di} \cdot \mu$	5,6		1,6		kN
$\sigma_{c,5}$	2,2	4,1	0,7	3,4	N/mm^2
τ_5	0,7		0,2		N/mm^2
$f_{c,90,d}$	5,2		5,2		N/mm^2
$f_{v,r,d}$	0,5		0,5		N/mm^2
UC compression	43%	80%	13%	65%	–
UC shear	145%		42%		–

The compression stress at the outside chest is calculated for case 1 and 2. For case 1 the shear stress due to friction is calculated. This force is case dependent and different for the heel and mitre posts. For compression is used $\frac{F_{do}}{A} \leq f_{c,90,d}$, for shear is used $\frac{3F_{f,6}}{2A} \leq f_{v,r,d}$. Table 3.14 shows that in the heel post the shear stress is too high. In the mitre post both the shear and compression stress are to high for case 1. The compression in the mitre post for case 2 is okay.

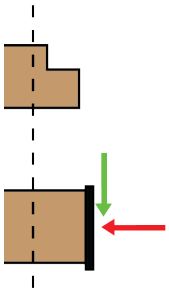

Figure 3.26: Location 6 in the heel and mitre post

Table 3.14: Compression and shear at location 6

	Heel post		Mitre post		
	Case 1	Case 2	Case 1	Case 2	Unit
y	100		100		mm
z	250		250		mm
$A = yz$	25000		25000		mm^2
F_{do}	124,7	101,0	144,5	89,0	kN
$F_{f,6} = F_{do} \cdot \mu$	24,9		28,9		kN
$\sigma_{c,6}$	5,0	4,0	5,8	3,4	N/mm^2
τ_6	1,5		1,7		N/mm^2
$f_{c,90,d}$	5,2		5,2		N/mm^2
$f_{v,r,d}$	0,5		0,5		N/mm^2
UC compression	96%	78%	111%	66%	–
UC shear	324%		377%		–

Compression and shear in the inside chest, locations 7

The stresses inside the chest in the post are calculated for case 1 and 2. The forces are case dependent and different for the heel and mitre posts. Compression is calculated with $\frac{F_{di}}{A_c} \leq f_{c,90,d}$, for shear $\frac{3F_{v,7}}{2A_s} \leq f_{v,r,d}$ is used. $F_{v,7}$ is different depending on the case. For case 1 it is $F_{v,7} = \mu F_{fi}$ while for case 2 it is $F_{v,7} = F_r$. This cross section fails for the shear verification in case 2 as shown in table 3.15.

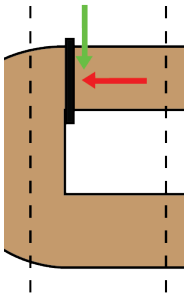

Figure 3.27: Location 7 in the heel and mitre post

Table 3.15: Compression and shear at location 7

	Heel post		Mitre post		
	Case 1	Case 2	Case 1	Case 2	Unit
$x = h$	270		210		mm
y	100		100		mm
z_s	250		250		mm
$z_c = l_{ef}$	340		320		mm
$A_s = yz_s$	25000		25000		mm^2
$A_c = yz_c$	34000		32000		mm^2
F_{di}	27,8	51,6	8,1	42,3	kN
$F_{v,7}$	5,6	69,6	1,6	118,8	kN
$\sigma_{c,7}$	0,8	1,5	0,3	1,3	N/mm^2
τ_7	0,3	4,1	0,1	7,1	N/mm^2
$f_{c,90,d}$	5,2		5,2		N/mm^2
$f_{v,r,d}$	0,5		0,5		N/mm^2
UC compression	16%	29%	5%	25%	–
UC shear	73%	905%	21%	1550%	–

Compression and shear in the outside chest, locations 8

In the outside chest stresses are calculated for case 1 and 2. There are two locations, location 8_h this is in front of the seal strip in the heel joint. The location 8_m is at the end of the mortise. This is shown in figure 3.28. The forces are case dependent and different for the heel and mitre posts. Compression is calculated with $\frac{F_{do}}{A_c} \leq f_{c,90,d}$, for shear $\frac{3F_{v,8}}{2A_s} \leq f_{v,r,d}$ is used. $F_{v,8}$ is different depending on the case and the post. For case 1 in the heel and mitre post it is $F_{v,7} = \mu F_{fo} + F_{ten}$. Case 2 in the heel post has $F_{v,7} = F_r$ it is assumed that the F_{ten} is transferred directly to the support and thereby not included at this location. In case 2 for the mitre post it is $F_{v,7} = F_r + F_{ten}$. In this cross section the shear verification fails in case 1 and 2 as shown in table 3.15.

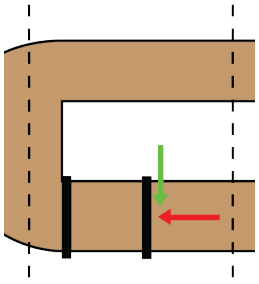

Figure 3.28: Location 8 in the heel and mitre post

Table 3.16: Compression and shear at location 8

	Heel post		Mitre post		
	Case 1	Case 2	Case 1	Case 2	Unit
$x = h$	151		226		mm
y	100		100		mm
z_s	250		250		mm
$z_c = l_{ef}$	300		320		mm
$A_s = yz_s$	25000		25000		mm^2
$A_c = yz_c$	30033		32533		mm^2
F_{do}	124,7	101,0	144,5	85,0	kN
$F_{v,8}$	48,3	69,6	49,4	169,8	kN
$\sigma_{c,8}$	4,1	3,4	4,4	2,6	N/mm^2
τ_8	2,9	4,1	3,0	10,2	N/mm^2
$f_{c,90,d}$	5,2		5,2		N/mm^2
$f_{v,r,d}$	0,46		0,5		N/mm^2
UC compression	80%	69%	86%	50%	–
UC shear	628%	905%	645%	2215%	–

Moment in the bottom of the mortise, the 3D effect at location 9

The force in the tenon is assumed as a equivalent pressure over the width of the mortise, the 3D effect of the mortise. At this location it is assumed that the total shear force is transferred through this mechanism. This part of the mortise is simplified as a two sided clamped beam with the thickness of $\frac{1}{4}$ of the depth of the mortise shown in figure 3.6. With these assumptions the moment in the middle of the mortise is calculated according $M_m = \frac{Ql}{24}$. The stress from the moment follows from $\frac{M_m}{W} \leq f_{m,d}$. Table 3.17 shows that the the unity checks are small.

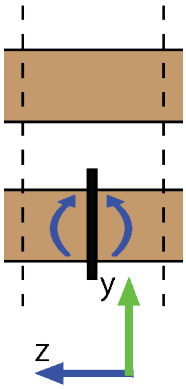

Figure 3.29: Location 9 in the heel and mitre post

Table 3.17: Moment at location 9

	Heel post		Mitre post		
	Case 1	Case 2	Case 1	Case 2	Unit
$x = \frac{l_t - l_{oc}}{4}$	69		54		mm
y	100		100		mm
$z = l$	250		250		mm
$W = \frac{1}{6}xy^2$	115000		90000		mm^3
Q	23,4	53,9	20,6	51,1	kN
M_m	243750	561771	215000	532083	Nmm
$\sigma_{m,9}$	2,1	4,9	2,4	5,9	N/mm^2
$f_{m,d}$	26,9		26,9		N/mm^2
Unity check	8%	18%	9%	22%	–

Shear at the corner of the mortise the 3D effect, location 10

The force in the tenon F_{tem} is transferred through shear to the full cross section of the post. The force in the tenon is divided by two $F_{v,10} = F_{ten}/2$, on half for each side of the mortise. The distance from the seal strip to the end of the post is the assumed width of the shear area, for the heel post. The width in the mitre post is assumed equal to the depth of the mitre mortise. The shear is calculated via $\frac{3F_{v,10}}{2A} \leq f_{v,r,d}$. In table 3.18 is shown that the shear stress for case 2 in the heel post exceeds the shear strength.

The reduced shear at the corner of the mortise the 3D effect, location 11

The force in the tenon is transferred via shear to the full cross section of the post. The shear is reduced due to possible crack formation parallel to the fibre. In figure 3.31 is shown how the reduced shear calculation is applied at this part of the mortise. In paragraph 2.4 is this calculation method explained and is calculated according EC 5. Here the distance x is chosen to be $\frac{1}{4}$ of the width of the mortise. Table 3.19 shows that the shear for case 1 in the mitre post is valid. The other stresses are too high.

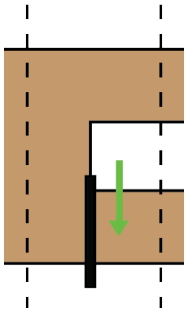

Figure 3.30: Location 10 in the heel and mitre post

Table 3.18: Shear at location 10

	Heel post		Mitre post		
	Case 1	Case 2	Case 1	Case 2	Unit
x	175		250		mm
y	100		100		mm
$A = xy$	17500		25000		mm^2
$F_{v,10}$	11,7	26,9	10,3	25,5	kN
τ_{10}	1,0	2,3	0,6	2,5	N/mm^2
$f_{v,d}$	1,9		1,9		N/mm^2
Unity check	52%	120%	32%	80%	–

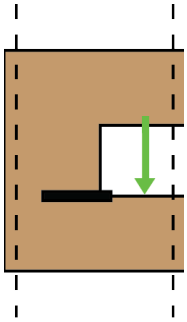

Figure 3.31: Location 11 in the heel and mitre post

Table 3.19: Reduced shear at location 11

	Heel post		Mitre post		
	Case 1	Case 2	Case 1	Case 2	Unit
x	62,5		62,5		mm
$y = h$	300		300		mm
h_e	100		100		mm
$a = \frac{h_e}{h}$	0,3		0,3		–
k_v	0,4		0,4		–
τ_{11}	1,0	2,3	0,6	2,5	N/mm^2
$f_{v,d}k_v$	0,7		0,7		N/mm^2
Unity check	136%	314%	84%	209%	–

The shear in the tenon, location 12

The shear force in the tenon is directly transferred to the mortise via the tenon. Depending on the case a part of the shear force is transferred through friction. The shear in the tenon is calculated according $\frac{3F_{v,12}}{2A_s} \leq f_{v,r,d}$ Table 3.20 shows that the shear stress for case 2 are to high.

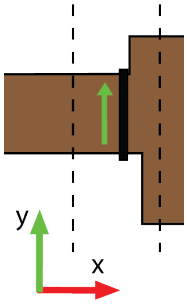

Figure 3.32: Location 12 on the heel and mitre side of the beam

Table 3.20: Shear at location 12

	Heel post		Mitre post		
	Case 1	Case 2	Case 1	Case 2	Unit
y	100		100		mm
z	250		250		mm
$A = xy$	25000		25000		mm^2
$F_{v,12}$	23,4	53,9	20,5	51,0	kN
τ_{12}	1,4	3,2	1,2	3,1	N/mm^2
$f_{v,d}k_v$	1,9		1,9		N/mm^2
Unity check	73%	168%	64%	160%	–

The reduced shear in the tenon, location 13

The distance x is chosen in the heel tenon to be the distance of the tenon pit to half the support $x = 213,50\ mm$. This distance is from the tenon pit to the end of the tenon $x = 198\ mm$ in the mitre post. Table 3.21 shows that all the reduced shear stresses are to high.

Moment in the tenon, location 14

The last verification is the moment verification in the tenon. The size of the moment differs between the cases. The stress from the moment follows from $\frac{M_t}{W} \leq f_{m,d}$. Table 3.22 shows that in case 1 the stress due to the moment are valid.

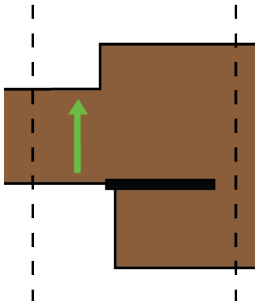

Figure 3.33: Location 13 on the heel and mitre side of the beam

Table 3.21: Reduced shear at location 13

	Heel post		Mitre post		
	Case 1	Case 2	Case 1	Case 2	Unit
x	213,5		198		mm
$y = h$	250		250		mm
h_e	100		100		mm
$a = \frac{h_e}{h}$	0,4		0,4		–
k_v	0,2		0,2		–
τ_{13}	1,4	3,2	1,2	3,1	N/mm^2
$f_{v,d}k_v$	0,4		0,4		N/mm^2
Unity check	354%	890%	296%	736%	–

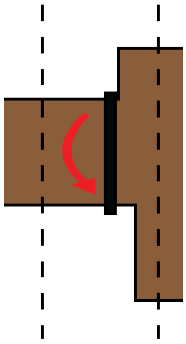

Figure 3.34: Location 14 on the heel and mitre side of the beam

Table 3.22: Moment at location 14

	Heel post		Mitre post		
	Case 1	Case 2	Case 1	Case 2	Unit
y	100		100		mm
$z = l$	250		250		mm
$W = \frac{1}{6}xy^2$	416667		416667		mm^3
M_t	5,6	12,8	6,9	17,1	kNm
$\sigma_{m,6}$	13,3	30,7	16,5	41,0	N/mm^2
$f_{m,d}$	26,9		26,9		N/mm^2
Unity check	50%	114%	61%	153%	–

Conclusions on the verification

Multiply locations where verified. The maximum strength is exceeded at multiple locations shown in table 3.23. In reality there will be a combination of case 1 and 2 with some 3D effect. This will lower the forces and thereby the stresses. How this is combined remains unknown.

Some of the calculations are based on the EC 5 for the notched beam. In the previous chapter 2 is already stated that this norm is not valid for azobé tenons beams, those calculations are in location 11 and 13. Only the stresses at the locations 1, 2, 3 and 9 are okay according verification. The calculations shown that there is a difference between the heel joint and the mitre joint. This shows that it is not sufficient to only look at one joint. There are checks at corresponding locations where the verification at the mitre joint is valid, while at the heel joint the verifications are not valid and the inverse. The results of the final element model in chapter 5 will show: how the combination of case 1 and case 2 with 3D effect happens trough the stress is distributed in the joint.

Table 3.23: Overview of the verification of the locations

	Heel post		Mitre post	
	Case 1	Case 2	Case 1	Case 2
Compression at location 1	Valid	Valid	-	-
Compression at location 2	Valid	Valid	-	-
Compression at location 3	-	-	Valid	Valid
Tension at location 4	Not valid	Not valid	Not valid	Not valid
Compression at location 5	Valid	Valid	Valid	Valid
Shear at location 5	Not valid	-	Valid	-
Compression at location 6	Valid	Valid	Not valid	Valid
Shear at location 6	Not valid	-	Not valid	-
Compression at location 7	Valid	Valid	Valid	Valid
Shear at location 7	Valid	Not valid	Valid	Not valid
Compression at location 8	Valid	Valid	Valid	Valid
Shear at location 8	Not valid	Not valid	Not valid	Not valid
Moment at location 9	Valid	Valid	Valid	Valid
Shear at location 10	Valid	Not valid	Valid	Valid
Reduced shear at location 11	Not valid	Not valid	Valid	Not valid
Shear at location 12	Valid	Not valid	Valid	Not valid
Reduced shear at location 13	Not valid	Not valid	Not valid	Not valid
Moment at location 14	Valid	Not valid	Valid	Not valid

4

Explanation of the used finite element method

To get an bigger understanding on the stresses in the mortise and tenon joint, finite element modelling is used. Using a finite element method several chooses have to be made in designing the model. This chapter will explain the choices made in the different paragraphs.

The finite element program that is used is Abaqus CAE 6.14-1. Abaqus will be used to model the joint, to calculate the joint and display the results. The results are also exported to use in different computer programs as Excel 2011 and Maple 2017. Both Excel and Maple are used for further calculations.

The model used in this thesis has the flowing characteristics:

- Linear elastic orthotropic material in 3 dimensions
- The post and girder in the model are: solid, linear, homogeneous and deformable
- The supports of the model are handled by prescribed displacement and rotations
- The fibre directions in the model is aligned by using different material orientations
- Static calculations are done
- Surface-to-surface contact is used
- Coulomb friction is used
- The posts and girder are individual meshed
- 8-node linear brick reduced integration with hourglass control is used

These points will be explained in the next paragraphs.

4.1. Size, boundary conditions and material orientation

The geometry of the mortise and tenon joint flows the geometry found in table 2.1. Figure 4.1 shows the model with a length of the posts of 3250 mm

The used coordinate systems are displayed in figure 4.1. Two support areas support the heel post. Area one is where the heel meets the embedding of the lock. The chosen support is $u_2 = u_3 = ur_2 = 0$ in the global coordinate system. The second support area of the heel post is the location of the seal strip. The supports that are used at this location are $u_2 = u_3 = ur_1 = 0$ in the global coordinate system. In reality $u_2 \leq 0$ because only compression is transferable at this support. The support of the mitre post is $u_2 = u_3 = ur_1 = 0$ in the local coordinate system. The local coordinate system is used to incorporate the angle of the mitre post. The supports are drawn in figure 4.2. The supports are chosen to fix the model in the z-direction. In the other directions of the supports is assumed that there is no friction, or shear resistance thus only roller supports are used. The supports that are used are a simplification. In reality friction is present at supports. The support of the seal strip is different because only compression is possible in reality.

Al wood species are a composite material of organic compounds. These organic compounds, make wood an orthotropic material, this means that the material properties differs along the direction of the material. The three directions where

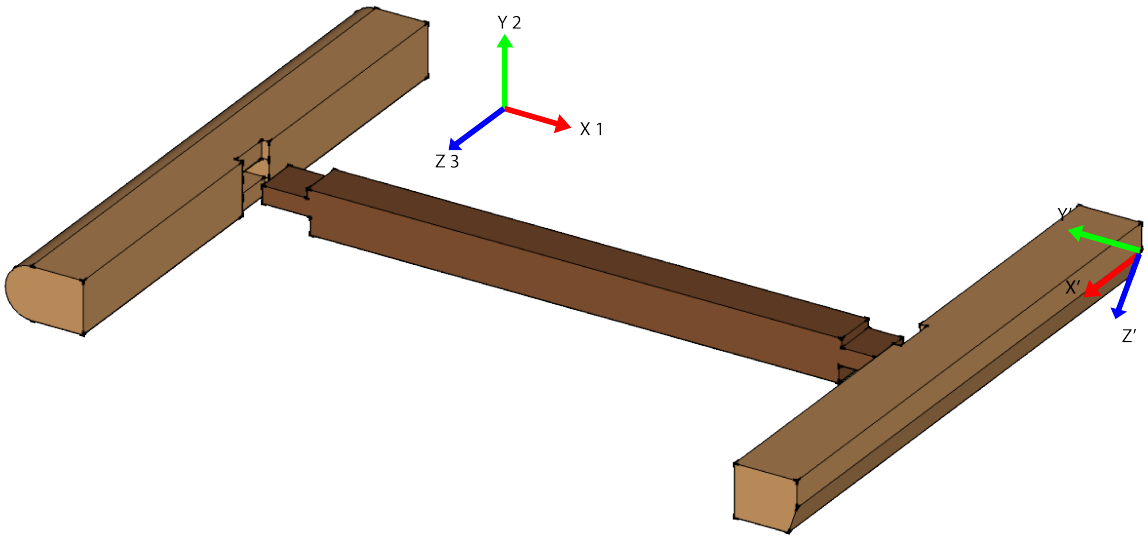

Figure 4.1: Exploded overview of the test model with the global and local coordinate system

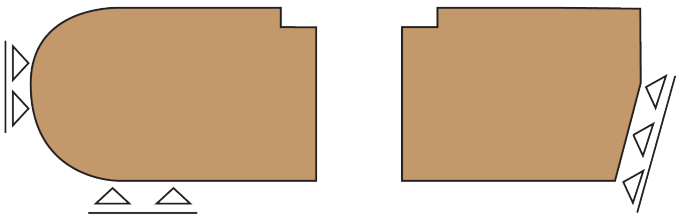

Figure 4.2: Supports of the posts

the properties of wood are different are: axial, radial and tangential.

The orthotropic property of timber leads to that the strength is different depending on the material orientation. The material orientation of the posts and girder are defined in the model to incorporate this property. The material orientation of the girder match with the global coordinates system. The posts use the material orientation where the fibre is parallel to the length of the posts. This is done by rotating the orientation 90° degrees clockwise around the y axis of the global coordinate system. The material orientations that are used in this model are shown in figure 4.3. This material orientation will have consequence for the stress plots. The stress plots refer to the material orientation and not to the coordinate system.

4.2. Material properties for the model

The strength of an linear elastic material is described in the three different directions 1,2 and 3 as shown figure 4.3 and by twelve constraints, with nine independents (E_1, E_2, E_3, G_{12}, G_{13}, G_{23}, υ_{12}, υ_{13}, υ_{23}, υ_{21}, υ_{31}, υ_{32}). These constrains are:

- Three moduli of elasticity E (Young's moduli) $[N/mm^2]$. The Young's modulus describes the relationship between the stress and the strain in a linear elastic material.
- Three moduli of rigidity or shear G $[N/mm^2]$ they describe the relation between the shear stress and the shear strain.
- Six Poisson's ratios υ $[-]$ are needed. The Poisson ratio's describes the perpendicular distortion of the material due to the elongation or shrinking, parallel from a force.

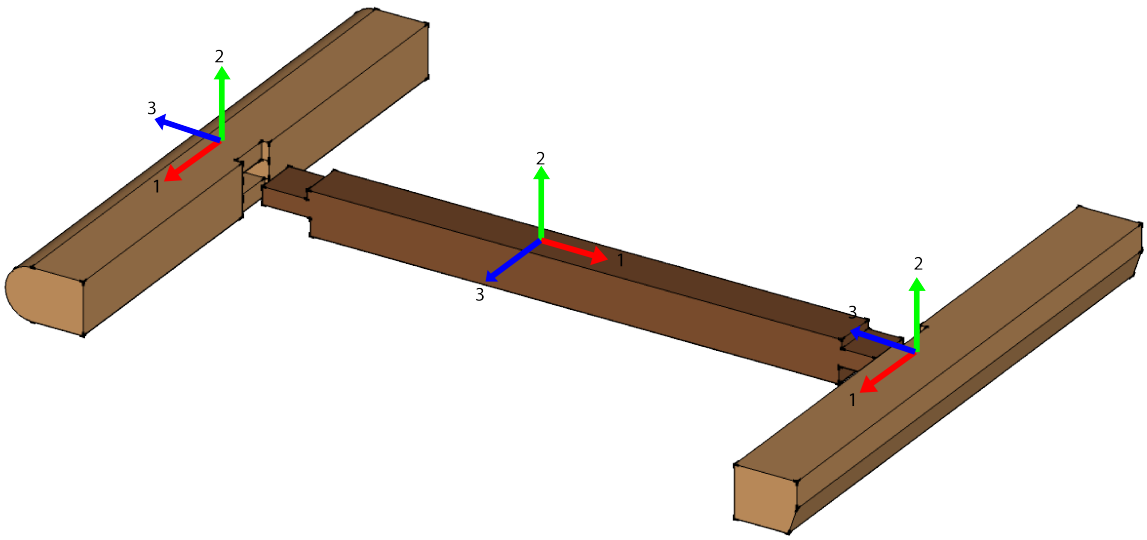

Figure 4.3: Material orientation in the model

The three moduli of elasticity are related to the six Poisson's ratios by the equation 4.1.

$$\frac{\upsilon_{ij}}{E_i} = \frac{\upsilon_{ji}}{E_j}, i \neq j \text{ and } i, j = 1,2,3 \tag{4.1}$$

Equation 4.1 implies that $\upsilon_{12} \neq \upsilon_{21}$, $\upsilon_{13} \neq \upsilon_{31}$ and $\upsilon_{23} \neq \upsilon_{32}$. Using equation 4.1 Abaqus needs nine constrains E_1, E_2, E_3, G_{12}, G_{13}, G_{23}, υ_{12}, υ_{13} and υ_{23} to simulate the material.

Strength class

Wood is a natural product with a large variation in its properties depending different conditions. To make wood suitable as a construction material strength grades are used to categorize the wood in different timber strength classes. This needs to be done according NEN-EN 384 (2016) and NEN-EN 14081 (2016). There are 6 different hardwood strength classes according the NEN-EN 338 (2016) . The strength class that is used for azobé lock gates is D70 currently the highest grade.

Young's moduli
The average Young's moduli E according NEN-EN 338 (2016) for the strengthen class D70 are $E_{0,mean}$ = 20000 N/mm^2, $E_{90,mean}$ = 1330 N/mm^2. Only two moduli are prescribed instead of the three that are needed. This is because it is not possible to make a distinction in the radial and the tangential direction in timber. The direction of the fibre in the timber corresponds with the direction 1 in the model. The directions 2 and 3 in the model are 90° degrees from direction 1 the fibre direction. The three moduli of elasticity are: E_1 = 20000 N/mm^2, E_2 = 1330 N/mm^2, E_3 = 1330 N/mm^2.

Moduli of rigidity
The moduli of rigidity or shear G are also described in NEN-EN 338 (2016). The value according NEN-EN 338 (2016) is G_{mean} = 1250 N/mm^2. Here only one value is give while three are needed for the model. With the fibre in direction 1, G_{mean} corresponds with G_{12} and G_{13} the value is G_{12} = 1250 N/mm^2 and G_{13} = 1250 N/mm^2. In the used coordinate system G_{23} corresponds with G_{roll}. This value is calculated with the assumption of Sandhaas (2012). This assumption states that the ratio between G_{mean}/G_{roll} is constant for different wood species. Using this assumption, spruce (C24) is used to calculated the ratio G_{mean}/G_{roll} = 690/50 = 13.8. With the ratio of 13.8 the azobé (D70) rolling shear is G_{roll} = $G_{12} = G_{mean}/13,8 = 1250/13,8 = 91\ N/mm^2$.

Poisson ratios
The last material properties that are used in Abaqus are the Poisson ratios υ. Poisson ratios for azobé are unknown. The Poisson ratios that are used in de model (υ_{12}, υ_{13} and υ_{23}), are obtained by calculating the average from different known Poisson ratios, from hardwood species with a density ≥ 500 kg/m^3 out of Wood Handbook (2010). Abaqus will then use equation 4.1 to calculate the other three ratios υ_{21}, υ_{31} and υ_{32}.

Table 4.1 shows the Poisson rations from hardwood species out of tabel 5-2 from Wood Handbook (2010). The row with "Species with average ≥ 500kg/m^3" shows the calculated averages from the above-mentioned wood species with a density higher than 500kg/m^3. The row at the bottom "Azobé used ratio NEN-EN 338" shows the values that are calculated by Abaqus using equation 4.1 with the average υ_{12} = 0,38, υ_{13} = 0,49 and υ_{23} = 0,67 and the previous E values out of the NEN-EN 338 (2016). This is also the reason why the values υ_{21} = 0,025, υ_{31} = 0,033 and υ_{32} = 0,670 do not match with the average ratios in the "Species with average ≥ 500 kg/m^3" row.

Table 4.1: Poisson ratios for hardwood species [22]

Species	Density $[kg/m^2]$	$\upsilon_{lr} = \upsilon_{12}$	$\upsilon_{lt} = \upsilon_{13}$	$\upsilon_{rt} = \upsilon_{23}$	$\upsilon_{tr} = \upsilon_{32}$	$\upsilon_{rl} = \upsilon_{21}$	$\upsilon_{tl} = \upsilon_{31}$
Sweetgum	545	0,325	0,403	0,682	0,309	0,044	0,023
Cherry, black	560	0,391	0,428	0,695	0,282	0,086	0,048
Mahogany, Honduras	590	0,314	0,533	0,600	0,326	0,033	0,034
Maple, red	610	0,434	0,509	0,762	0,354	0,063	0,044
Walnut, black	610	0,495	0,632	0,718	0,367	0,052	0,036
Mahogany, African	640	0,297	0,641	0,604	0,264	0,033	0,032
Maple, sugar	640	0,424	0,476	0,774	0,349	0,065	0,037
Ash, white	675	0,371	0,440	0,684	0,360	0,059	0,051
Birch, yellow	690	0,426	0,451	0,697	0,426	0,043	0,024
Oak, red	700	0,350	0,448	0,560	0,292	0,064	0,033
Oak, white	755	0,369	0,428	0,618	0,300	0,074	0,036
Species with average ≥ 500 kg/m^3	638	0,381	0,490	0,672	0,330	0,056	0,036
Azobé used ratio NEN-EN 338	1065	0,380	0,490	0,670	0,670	0,025	0,033

Friction coefficient
In the model, timber surfaces are in contact with each other. When there is contact between materials there is a possibility of friction. Friction is a reaction force of interacting surfaces. Friction is described with the formula $F_{max} = \mu F_n$ $[kN]$. Mu μ $[-]$ is the friction coefficient; there are two kinds of friction coefficients: static friction and kinetic friction. In the case of this connection static friction is needed because in this connection there is no big movement relative to each other.

The friction is modelled with the Coulomb friction model. This friction is dependent on the contact pressure between the surfaces, when a contact pressure is present a friction stress can develop. The two contacting surfaces are able to carry

shear stresses up to a certain magnitude across their interface before they start sliding relative to one another. The used friction model assumes isotropic friction, friction is the same in all directions.

The static friction coefficient for timber is depended on different factors: wood species, moisture content and roughness of the surface. Different wood species can have different extractives, there are extractives that are greasy or sticky. This grease or stick, can lead to decrease or increase the friction coefficient. It is assumed that this in not the case for azobé. An increase in moisture contents will lead to a bigger friction coefficient McKenzie and Karpovich (1968). In this wet environment it is assumed that the wood is fully saturated. It is assumed that the azobé timber that is used is smooth. In the research of McKenzie and Karpovich (1968) $\mu = 0,2$ is found as static friction coefficient, for smooth and fibre saturated timber. The used isotropic friction coefficient of 0.2 [−] for azobé is an assumption.

4.3. Contact surfaces

The girder and posts are in contact and thus contain contact surfaces with each other. In the previous paragraph the friction of these surfaces are explained. The model assumed hard contact. Hard contact means, that for contact between the surfaces it is necessary to have a contact pressure. When there is a gap between the surfaces no contact pressure is possible.

All the contact surfaces are assigned a master or slave surface. The master surface is impermeable for the slave surface while the master surface will penetrate the slave surface. The model uses the 'surface-to-surface' contact method. This means that the whole surface makes contact with the whole other surface. This way there is less penetration of the slave surface. The benefit of using this surface-to-surface method, is that this will lead to more accurate stress results at corners in the model. In the model the girder contains the master surfaces, while the post contains the slave surfaces.

4.4. Calculation method

The use of friction at the contact surfaces leads to non-linear equations. The calculation method that is fit for static non-linear equations is Full Newton. The Full Newton method is used for al the steps, until a equilibrium is reached.

The model is split in two steps that are automatically divided into smaller increments. The two steps that are used are:

Set-up step The set-up step secures the girder in the mortises of the posts. The supports are applied to the posts. At the end of this step the model is fixed.

Test step In the test step the pressure load is applied 35 kN/m. The automatic increments split this step in six load increments until the last step. The total load is present at the last step.

4.5. The mesh and the elements of the model

The elements that are used are an 8-node linear brick with reduced integration and with hourglass control. This is an first-order solid element, the element is shown in figure 4.4.

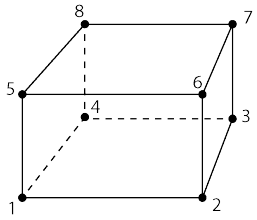

Figure 4.4: An 8-node linear brick

Reduced integration is used instead of a full integration. Using first order elements and reduced integration will increase the computational efficiency, because of less integration point this is shown in figure 4.5. Reduced integration will also prevent locking of the elements. Locking means that the element act more stiff than they are.
Hourglass control is applied to prevent the hourglass mode of the elements. Figure 4.6 shows the element with the reduced integration and the possible hourglass mode. In the hourglass mode deformation is happening while there is no change in energy, because the stationary location of the integration point.

The mesh that is used is displayed in figure 4.7, 4.8 and 4.9. Around the joint a finer mesh is used for accurate measurements. The mesh that is used outside the joint, is a more coarse mesh to reduce the calculation time. The mesh is made

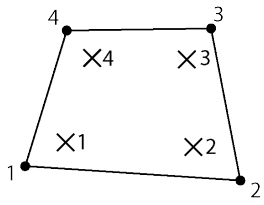

Figure 4.5: Reduced integration for one side of the element

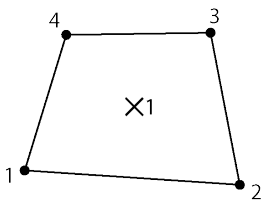

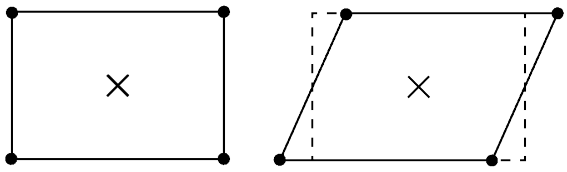

Figure 4.6: Hourglass mode of one side of the element

up of mostly straight lines where possible, to make it more suitable for making Excel graphs. The graphs are made with the data points of the mesh. Due to the different angles of the gate models, the geometry of all three mitre posts are different. This result in three different meshes, all three models are meshed along the explained guidelines.

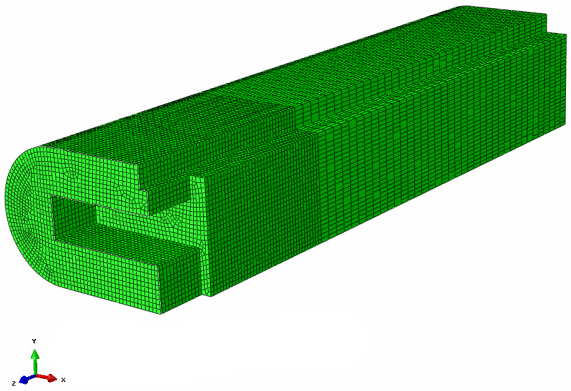

Figure 4.7: Half of the heel post

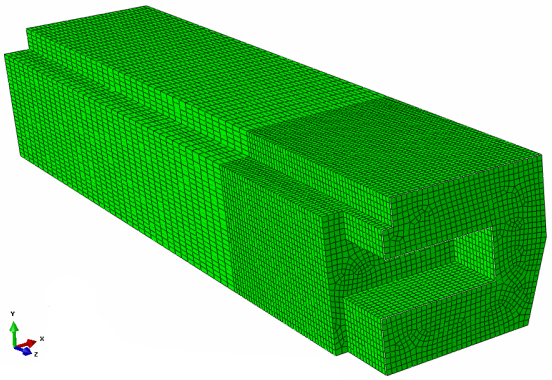

Figure 4.8: Half of the mitre post

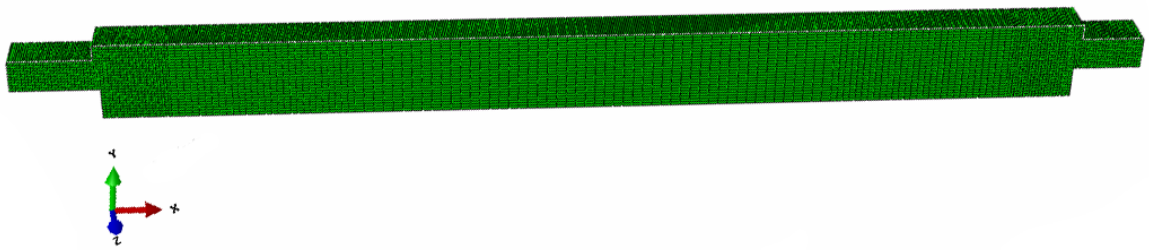

Figure 4.9: The girder, heel side on the left mortise side on the right

5

Results of the finite element model

This chapter is split in two parts: the contact stresses in the joints and the stress perpendicular to the fibre in the y-direction. In the first part the contact stresses are used to calculate the force equilibrium in the x and z-direction, using the contact stresses of the three different gate angles 15°, 18,5° and 30° degrees. The contact stresses are studied in depth in the same paragraph for the three different gate angles. After studying the contact stresses, the stresses perpendicular to the fibre in the y-direction of the mortise (location 11 in paragraph 3.3.5.) and of the tenon (location 13 in paragraph 3.3.5.) are studied.

The contour plots from Abaqus are used to analyse the acting stresses without safety factors. Excel is used to plot the values of the lines shown in the contour plot. This is done to give an indication of the shape of the pressure and stress distribution. Excel is also used to calculate the sectional forces on these areas by using the pressures, to indicate how the forces are transferred.

Local peak stresses in the results need to be handled with caution, because of elastic modelling and possible model singularity. In reality due to plastic behaviour stresses will redistribute when the ultimate strength is reached. In this model the stress will increase beyond the ultimate strength without redistribution in the model. The finite element model can contain singularity's. Singularity's are points in the model where the stress values goes to infinity. Sharp concave corners in the model are sensitive for singularity's. When the elements of the mesh becomes smaller the stress value at the singularity will increase. This will show the location of the singularity's. In this model only one mesh is used. A result of this is that the exact location of singularity's are not known. The possibility of singularity's at corners in the model should be noted.

5.1. Contact stresses for three different gate angles

The different gate angles, result in different internal forces as shown in paragraph 3.3.1. that will result in possibly different contact stresses at the joints. At first the force equilibrium in the x and z-direction is calculated to validate the model. In the second part the values and the shapes of the contact stresses are studied. There are 6 contact areas that are studied all shown in figure 5.1. The contact areas are named from a to f for both the heel joint and the mitre joint. All the stresses and the forces in this paragraph are related to one of those areas.

5.1.1. Force equilibrium based on the joint contact stresses

A quick simplified verification of this model is done in this paragraph. The found contact pressures in the FEM are multiplied by the corresponding area. This way the resulting contact force on the area is calculated in the x and z-direction. By calculating the force this way in the x-direction, it is assumed that the stress due to the moments at both joints are the same. This makes it possible to calculate the force equilibrium in the x-direction. This is not the reality, this simplification is done to use of the same data for multiple calculations to save time. This is also the reason that force equilibrium in the y-direction is not done. This simplification is not valid for the y-direction. This is shown in paragraph 5.1.3.

The resulting forces in the x-direction are shown in table 5.1. The x-direction compression force is coming from area c and f. The x-direction friction forces are coming from area a,b,d and e.

Subtracting the total x-direction forces of the mitre joint from the heel joint results in $1,1\ kN$ for 15° degrees, $0,9\ kN$ for 18,5° degrees and $-3,6\ kN$ for 30° degrees. This difference would have been $0\ kN$ when the heel joint and the mitre joint

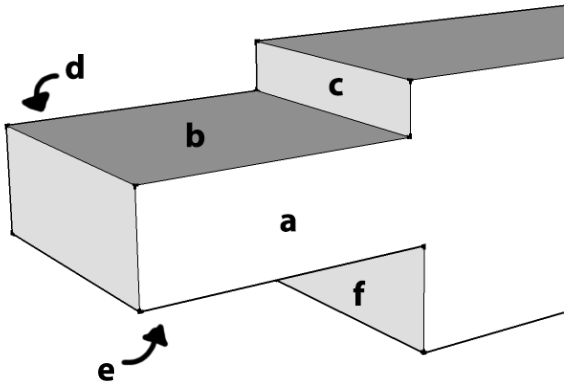

Figure 5.1: Locations of the contact areas for both heel and mitre tenons

Table 5.1: Resulting x-direction contact forces of the joints

	Heel joint			Mitre joint		
Angle [degrees]	15°	18,5°	30°	15°	18,5°	30°
Total pressure [kN]	−162.6	−130.2	−81.7	−175.4	−141.9	−84.3
Total friction [kN]	−26.5	−23.5	−14.0	−14.9	−12.7	−7.7
Total normal force [kN]	−189.1	−153.7	−95.7	−190.3	−154.6	−92.1

are subjected to the same moment. The differences are close to 0 kN this means that there is a difference in the moment between the heel and mitre joints. The moments are calculated in paragraph 5.1.2. there is shown in the tables 5.4 and 5.7 that they are close to each other.

The resulting forces in the z-direction are shown in table 5.2. The z-direction compression force is coming from area a and d. The z-direction friction forces are coming from area b,c,e and f, this is zero. There is no external force present in the z-direction. This means that the forces present in both joints needs to be in equilibrium.

Table 5.2: Resulting z-direction contact forces of the joints

	Heel joint			Mitre joint		
Angle [degrees]	15°	18,5°	30°	15°	18,5°	30°
Pressure area a [kN]	40,0	34,9	25,7	26,9	23,4	19,6
Pressure area d [kN]	−39,8	−34,7	−25,6	−26,9	−23,6	−19,2
Total normal force [kN]	0,2	0,2	0,1	−0,1	−0,2	0,4

The resulting force in the z-direction are all almost 0 kN. In the z-direction there is a difference between the force on the heel and mitre joint.

In the x-direction equilibrium is not zero because of a possible influence of a moment difference at the joints, this is calculated in paragraph 5.1.2. The x-direction equilibrium is just slightly off due to a possible moment difference but assumed in equilibrium. In the z-direction equilibrium is almost zero thus assumed valid. On the basis of this quick simplified verification of the z and x-direction equilibrium of the joints, the model is assumed valid. A more in depth look at the contact pressures is present in the paragraph 5.1. were also the contact pressures in the y-direction are studied.

5.1.2. Contact stresses in the x-direction

The contact stresses in the x-direction are the contact pressures at area c and f and the contact friction acting on the areas a, b, d and e.

Heel joint

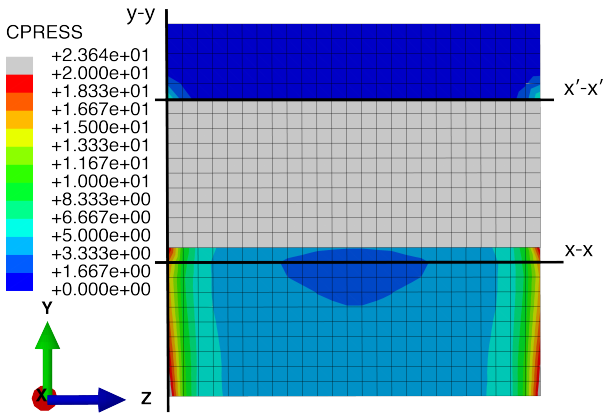

Figure 5.2: Contour plot area c and f in the heel joint $[N/mm^2]$

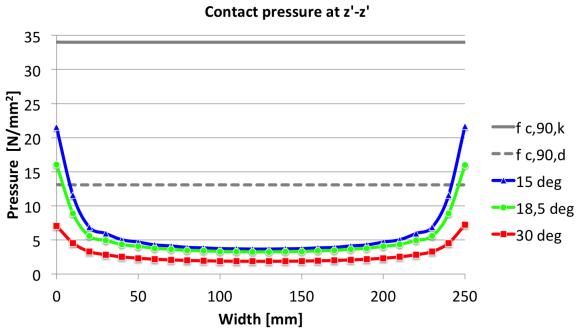

Figure 5.3: Contact pressures at z'-z' in the heel joint $[N/mm^2]$

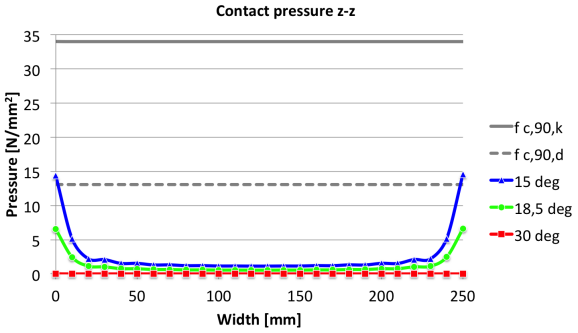

Figure 5.4: Contact pressures at z-z in the heel joint $[N/mm^2]$

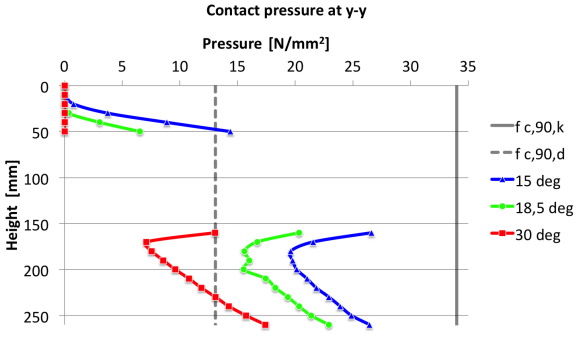

Figure 5.5: Contact pressures at y-y in the heel joint $[N/mm^2]$

The contour plot in figure 5.2 shows the contact pressures in area c and f for a gate angle of 18,5° degrees. The biggest pressures are present at the edges of the beam. Both figures 5.3 and 5.4 show the similarities between the different gate angles. The edges of the beam obtain the biggest pressure while the pressure in the middle of the beam is almost evenly distributed. Figure 5.5 shows the contact pressures at the edge of the beam in the y-direction, with the location shown in figure 5.2. All the gate angles exceed the design value of compressive strength parallel to grain in area f, this only occurs at the edges of the beam. When the gate angle is 30° degrees, there is no contact with area c. The other gate angles have small contact pressures at the bottom of area c. The bolted steel strips that are present in reality, are able to transverse tension in position of the mt joint. The bolted connection will probably maintain the timber to timber contact at area c and result in a different contact pressure distribution.

The equivalent point forces along the height of the beam, are calculated by multiplying the pressure with the area. The distance of the equivalent point force is calculated by calculating the point of gravity of all the contact pressure distributions along the height. Table 5.3 shows the height on which the equivalent force is present. The forces are negative because they are in the opposite direction of the global axis system. With these equivalent forces a moment is calculated, that is the result of the contact pressure. The moments are shown in table 5.4.

Table 5.3: Forces and there location on area c and f in the heel joint

Area and Angle [deg]	Distance from top [mm]	Force [kN]
c 15°	41	−10
c 18,5°	44	−3
c 30°	0	0
f 15°	202	−153
f 18,5°	202	−127
f 30°	205	−82

Table 5.4: Moment due to the different angles on area c and f in the heel joint

Gate angle [deg]	Moment [kNm]
15°	31
18,5°	26
30°	17

Table 5.5: Friction forces in the x-direction in the heel joint

	Friction force [kN]		
Area	15°	18,5°	30°
a	−5	−4	−1
b	−4	−4	−3
d	−5	−4	−1
e	−12	−11	−9

The friction forces in the x-direction are unevenly distributed over the area a and d. To maintain an overview of the forces differences between the gate angles, only the sizes of the frictions are considered in table 5.5. The distribution of the friction force are left out.

Mitre joint

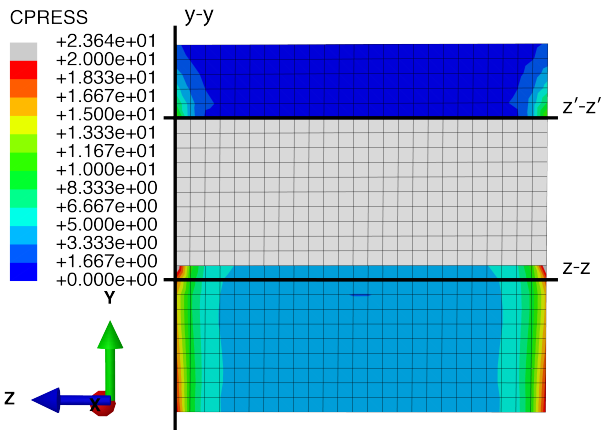

Figure 5.6: Contour plot area c and f in the mitre joint [N/mm^2]

The contour plot of the mitre joint in figure 5.6 shows the contact pressure in area c and f for a gate angle of 18,5° degrees. The biggest pressures are present at the edges of the beam the same location as in the heel joint. The edges of the beam endures the biggest pressure while the pressure in the middle of the beam is almost evenly distributed as shown in figure 5.8 and figure 5.7. Area c has bigger contact pressure compared to the heel joint. Figure 5.9 shows the contact pressure at the edge of the beam. All the gate angles exceed the design value of compressive strength parallel to grain in area f. This only occurs at the edges of the beam. With a gate angle of 30° degrees there is no contact with area c. The other gate angles do have small contact pressures at the bottom of area c like in the heel joint. The bolted steel strips can have an influence on this.

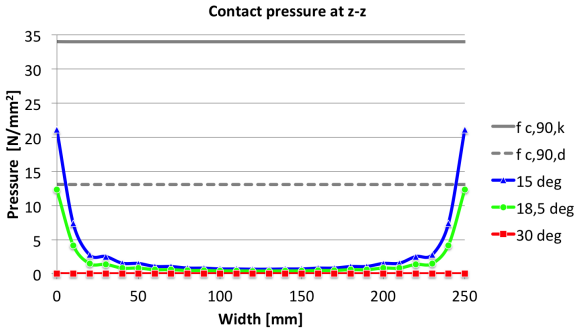

Figure 5.7: Contact pressure at z-z in the mitre joint $[N/mm^2]$

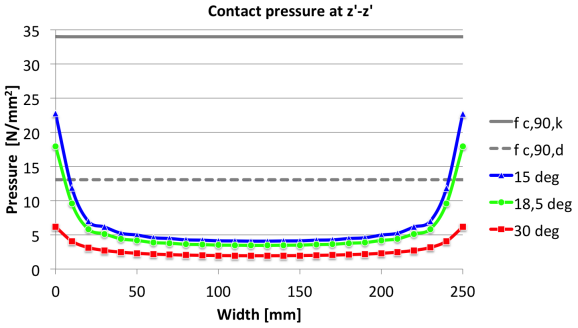

Figure 5.8: Contact pressure at z'-z' in the mitre joint $[N/mm^2]$

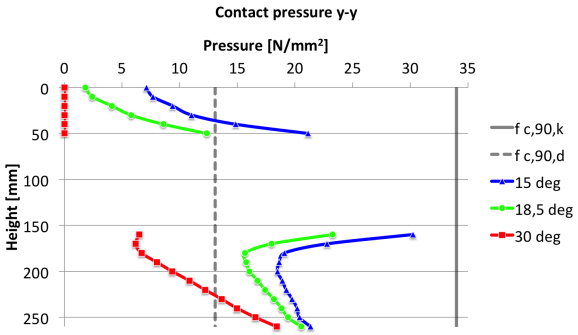

Figure 5.9: Contact pressure at y-y in the mitre joint $[N/mm^2]$

The equivalent point forces are calculated the same way as in the heel joint. Figure 5.6 shows the height on which the equivalent force is present. The forces are positive, because they are in the direction of the global axis system. With these values a moment is calculated that is the result of the contact pressure. The moments are shown in table 5.7.

Table 5.6: Forces and there location on area c and f in the mitre joint

Area and Angle $[deg]$	Distance from beam top $[mm]$	Force $[kN]$
c 15°	26	32
c 18,5°	29	15
c 30°	0	0
f 15°	199	143
f 18,5°	200	126
f 30°	206	84

The friction forces in the x-direction are unevenly distributed on the areas. The distribution of the friction force are left out. The friction forces are shown in table 5.8.

Difference between the mitre joint and heel joint in the x-direction

- More than 90% of the compression force is transferred via area f in the heel joint. This value increase with the angle of the gate to 100%.
- More than 80% of the compression force is transferred via area f in the mitre joint. This value increase with the angle of the gate to 100%
- The bolted connection will probably have influence on the contact at area c.
- In the heel joint 15% of the total force in the x-direction transferred via friction.
- In the mitre joint 8% of the total force in the x-direction is transferred via friction.
- The moments due to the contact pressures are almost the same. This is in line with the assumption in paragraph 5.1.1. They are the same despite the difference of the forces between heel and mitre joint.

Table 5.7: Moment due to the different angles on area c and f in the mitre joint

Gate angle $[deg]$	Moment $[kNm]$
15°	29
18,5°	26
30°	17

Table 5.8: Friction forces in the x-direction in the mitre joint

	Friction force $[kN]$		
Area	15°	18,5°	30°
a	4	3	0
b	0	0	1
d	4	3	0
e	7	7	7

5.1.3. Contact pressure in the y-direction

The contact stress in the y-direction are the contact pressures on area b and e and the contact friction acting on the areas a, c, d and f.

Heel joint

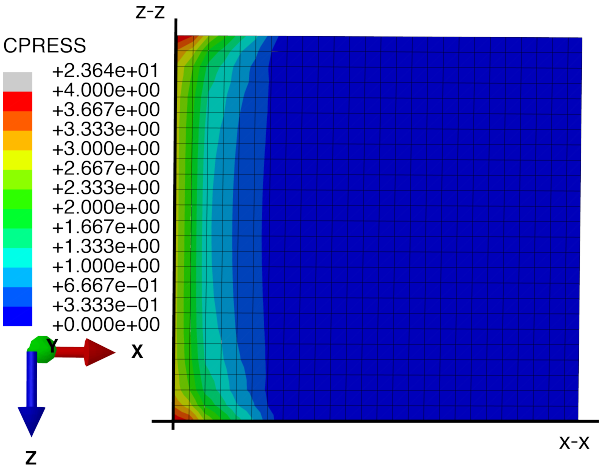

Figure 5.10: Contour plot area b in the heel joint $[N/mm^2]$

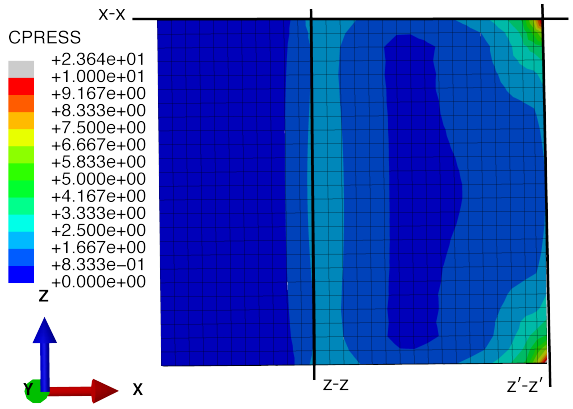

Figure 5.11: Contour plot area e in the heel joint $[N/mm^2]$

The contour plots in figure 5.10 and figure 5.11 show the contact pressure in area b and e for a gate angle of 18,5° degrees. The biggest pressures are present at the edges of the tenon shown in figure 5.11. The the hump between 80 mm and 150 mm has a evenly distributed pressure along the width of the tenon shown in figure 5.12. The pressure at the 0 mm on the top of the tenon in area b, are almost evenly distributed along the width of the tenon shown in figure 5.14. Figure 5.12 shows the peak pressure at the pit of the tenon on the edges of the tenon. These peak pressures exceed the design value of compressive strength perpendicular to grain from 260 mm to 276 mm at area e. The peak pressure on the edge are left out with the assumption of redistribution due plasticity and possible singularity's. Without the peak pressures figure 5.16 shows an polynomial pressure distribution along the width of the tenon with a $R^2 = 0,95107$ for a second order and $R^2 = 0,99813$ for an sixth order polynomial, the maximum possible order for polynomial regression lines in Excel. In figure 5.16 the regression line (black line) shows the sixth order polynomial.

The equivalent point force along the length of the tenon is calculated, by multiplying the pressure with the area. The distance of the equivalent point forces, are calculated by calculating the point of gravity of all the contact pressures distributions along the length. Table 5.9 shows the distance on which point the equivalent force is present. The forces at area b are negative because they are in the opposite direction of the global axis system. With these values a moment is calculated that is the result of the contact pressure. The moments in the tenon are shown in table 5.10.

The friction forces in the y-direction are unevenly distributed on the areas. The distribution of the friction force are left out. The friction forces are shown in table 5.11, they are positive and act in the direction of the global axis.

Mitre joint

The contour plots in figure 5.17 and figure 5.18 show the contact pressure in area b and e for a gate angle of 18,5° degrees. The biggest pressures are present at the edges of the tenon shown in figure 5.19. Figure 5.21 and 5.22 shows the peak pressures at the pit of the tenon and on the edged of the tenon. These peak pressures exceed the design value of compressive

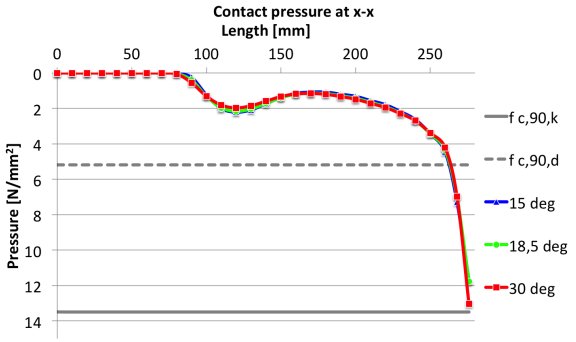

Figure 5.12: Contact pressure at area e x-x in the heel joint $[N/mm^2]$

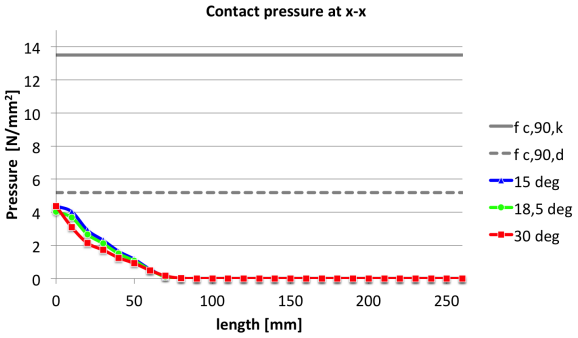

Figure 5.13: Contact pressure at area b x-x in the heel joint $[N/mm^2]$

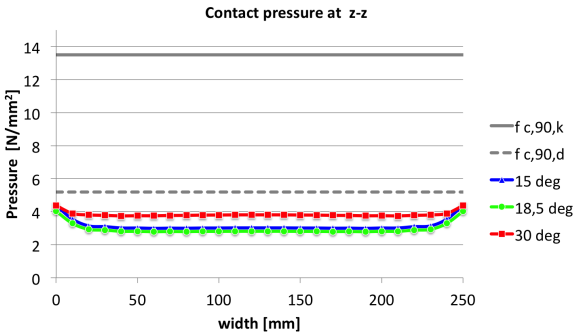

Figure 5.14: Contact pressure at area b z-z in the heel joint $[N/mm^2]$

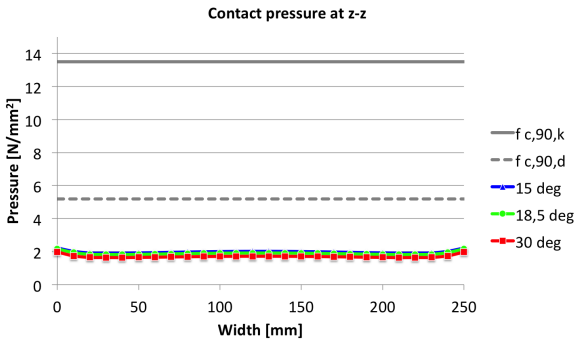

Figure 5.15: Contact pressure at area e z-z in the heel joint $[N/mm^2]$

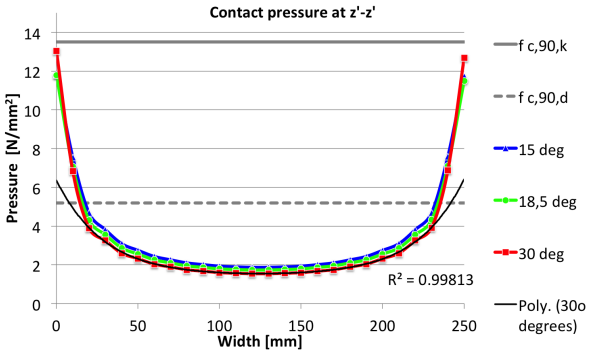

Figure 5.16: Contact pressure at area e z'-z' in the heel joint $[N/mm^2]$

Table 5.9: Forces and there location on area b and e in the heel joint

Area and angle $[deg]$	Distance from tenon tip $[mm]$	Force $[kN]$
b 15°	21	−21
b 18,5°	21	−19
b 30°	19	−19
e 15°	189	66
e 18,5°	188	63
e 30°	189	61

Table 5.10: Moment in the tenon at area b and e in the heel joint

Gate angle [deg]	Moment [kNm]
15°	12
18,5°	11
30°	11

Table 5.11: Friction forces in the y-direction in the heel joint

	Friction force [kN]		
Area	15°	18,5°	30°
a	4	4	3
c	2	1	0
d	5	4	3
f	5	6	8

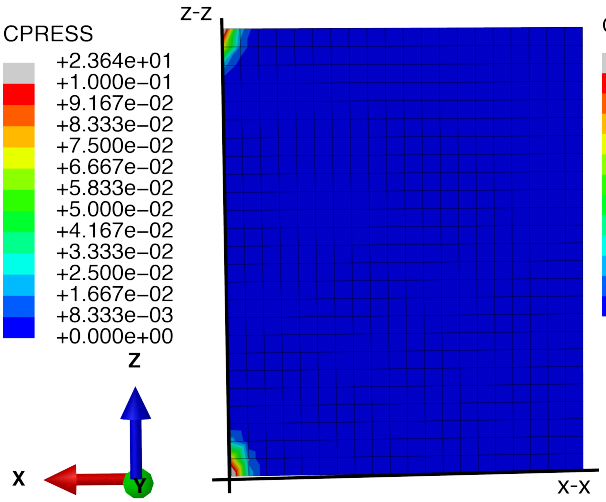

Figure 5.17: Contour plot area b in the mitre joint [N/mm^2]

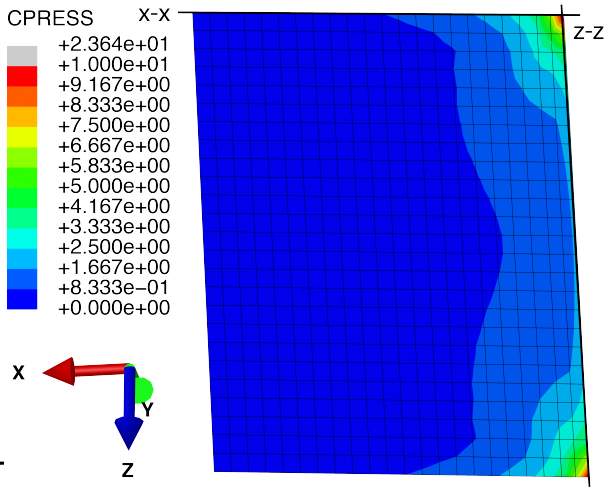

Figure 5.18: Contour plot area e in the mitre joint [N/mm^2]

strength perpendicular to grain from 208 mm to 216 mm of area e. Like in the heel joint an polynomial contact pressure distribution seems present along the width of the tenon, when the peak pressures are left out shown in figure 5.20. The pressures at 0 mm on the top of the tenon in area b, are almost evenly distributed along the width of the tenon this is shown in figure 5.20. The pressure at area b differ with the angle of the gate. When the angle of the gate is 30° degrees there is a pressure present while at 15° no pressure is present at area b.

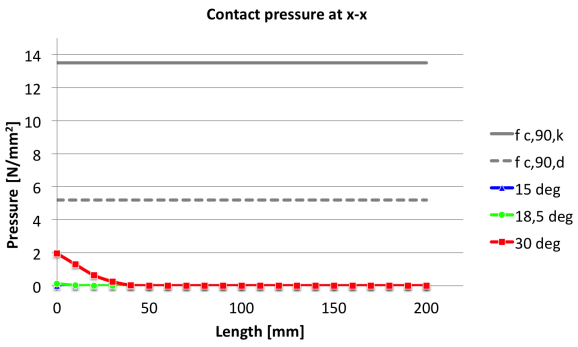

Figure 5.19: Contact pressure at area b x-x in the mitre joint [N/mm^2]

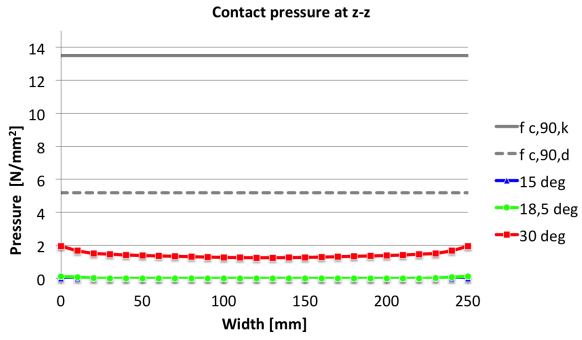

Figure 5.20: Contact pressure at area b z-z in the mitre joint [N/mm^2]

Table 5.12 shows the distance on which point the equivalent force is present. The forces at area b are negative because they are in the opposite direction of the global axis system. With these values a moment is calculated that is the result of the contact pressure in the tenon. This is shown in figure 5.13.

The friction forces in the y-direction are unevenly distributed on the areas. The distribution of the friction force are left out. The friction forces are shown in table 5.14 they are positive and act in the direction of the global axis.

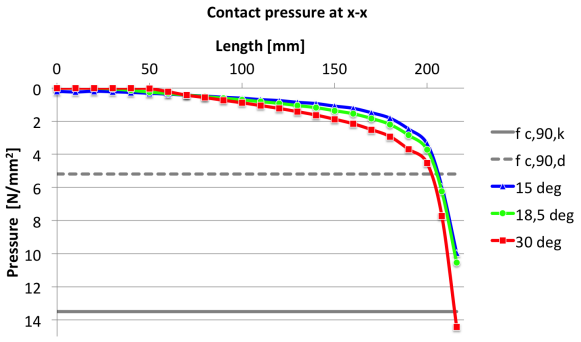

Figure 5.21: Contact pressure at area e x-x in the mitre joint $[N/mm^2]$

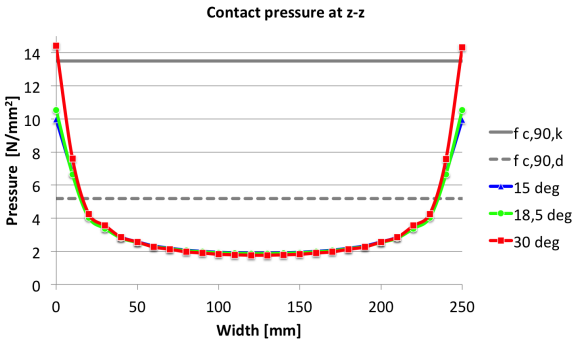

Figure 5.22: Contact pressure at area e z-z in the mitre joint $[N/mm^2]$

Table 5.12: Forces and there location on area b and e in the mitre joint

Area and angle $[deg]$	Distance $[mm]$	Force $[kN]$
b 15°	0	0
b 18,5°	5	0
b 30°	8	−4
e 15°	157	38
e 18,5°	162	40
e 30°	167	45

Table 5.13: Moment in the tenon due area b and e in the mitre joint

Gate angle $[deg]$	Moment $[kNm]$
15°	6
18,5°	6
30°	7

Table 5.14: Friction forces in the y-direction in the mitre joint

	Friction force $[kN]$		
Area	15°	18.5°	30°
a	3	3	3
c	5	3	0
d	3	3	3
f	5	6	9

Difference between the mitre and heel joint in the y-direction

- The contact pressure distribution along the length of the tenon on area e is different for the mitre and heel joint and unevenly distributed.
- The seal strip support B result in a bump in the contact pressure along the length, in the heel joint at area e.
- The moment in the tenon in the heel joint is almost twice the moment in the tenon in the mitre joint.
- Around 74% of the force in the y-direction is transferred via pressure, 26% via friction in the heel joint.
- Around 70% of the force in the y-direction is transferred via pressure, 30% via friction in the mitre joint.
- Area b in the mitre joint is subjected to a small negative force when the gate angle is 30° degrees, at an angle of 15° degrees this force is 0 kN.
- The heel joint caries 53% of the force in the y-direction at an angle of 15° degrees. It is 50% of the force at 30° degrees.
- The distance of the resulting force to the pit of the tenon, at area e is the bigger for the mitre joint 276 – 188 = 88 mm, at the heel joint it is 216 – 162 = 54 mm, due to size difference and the seal strip support.

5.1.4. Observations regarding the contact stress distribution

Figure 5.23 shows the heel and mortise tenon and the contact forces for a gate with a angle of 18,5° degrees. In both the mitre and tenon joint a 3D effect is present. The contact pressure distribution at the bottom of the tenon is distributed as a high order polynomial, with the biggest pressures at the edges of the tenon. This corresponds with the presumption that the force is unevenly distributed along the width of the tenon by van Otterloo (2013). The contact forces are different from the assumed cases 1 and 2 in chapter 3. The biggest differences are the forces in the x-direction in the outside and inside chests, this will result in lower tension forces behind the mortise than calculated in paragraph 3.2.3. Other notable differences are:

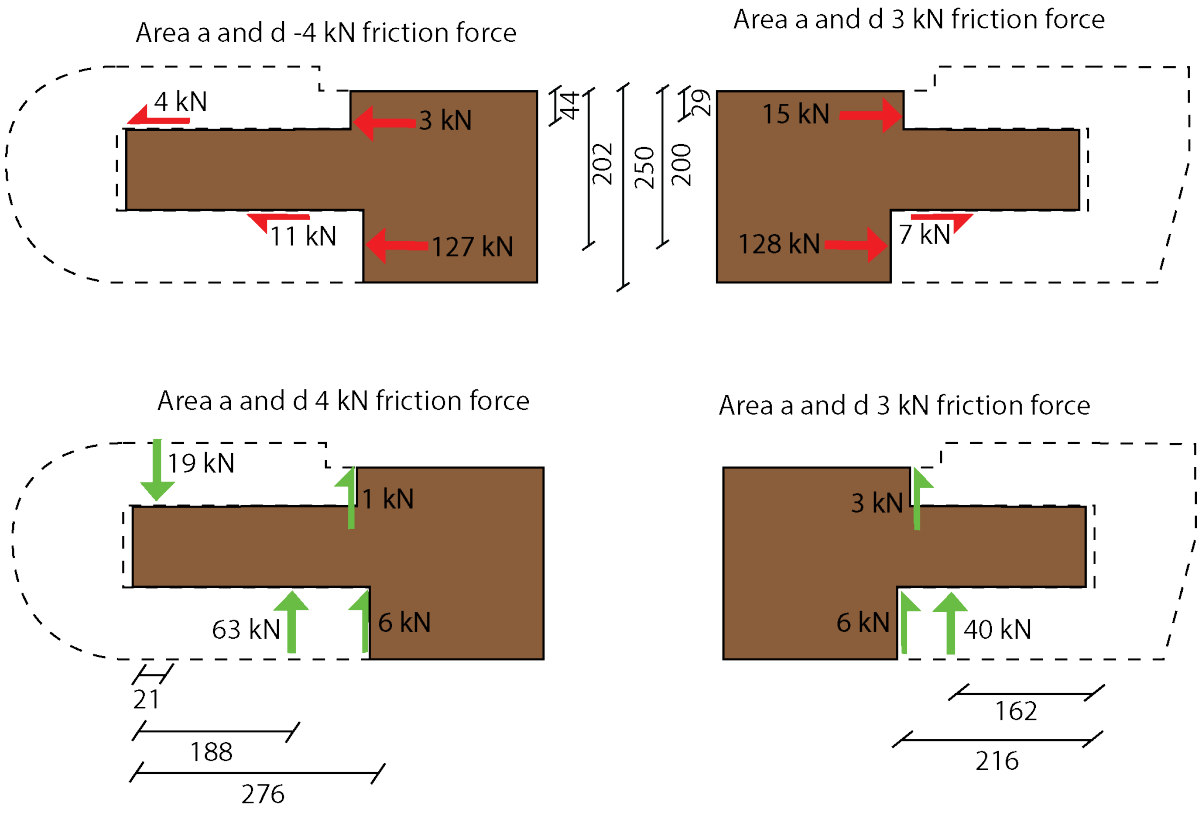

Figure 5.23: Overview of the resultant forces [kN] for a gate angle of 18,5° degrees distances in [mm].

- Bigger forces in the x-direction on the outside chest in case 2 and the heel of case 1.
- Smaller forces in the x-direction on the inside chest in case 2 and the heel of case 1.
- Friction in the x-direction is lower than in case 2. At the top of the heel tenon is a friction present.

- The force in the y-direction at the top of the heel tenon is smaller than in case 2. The bottom force is slightly smaller than in case 2. In the heel joint a clamping of the tenon is present thus matching the best with case 2.
- The force in the y-direction at top of the tenon in the mitre joint is zero, the force at the bottom of the tenon is twice the size of the calculated force in case 1. In the mitre joint is a no clamping of the tenon present thus matching the best case 1.
- The friction force in the y-direction on the chests are all smaller than calculated in case 1.
- Friction forces at the areas a and d are present in the model, not in the cases.

There is also an difference between the heel tenon and mitre tenon. The most notably differences are:

- The transfer of forces in the y-direction of the tenon, is different between the heel and mitre tenon.
- The heel joint acts as case 2 with clamping.
- The mitre joint acts as case 1 without clamping.
- Clamping in the heel joint result in a moment in the tenon twice the size of the moment in the tenon in the mitre joint.

5.2. Stresses perpendicular to the fibre

In this paragraph stresses perpendicular to the fibre are studied. This is done for a gate angle of $18,5°$ degrees. This internal stress is studied, because the verifications suggest the failure due to to high tension stress perpendicular to the fibre in the y-direction in the tenon pit and bottom corners of the mitres. This correspondent with the reduced shear verifications at location 11 and location 13 in paragraph 3.3.5.

5.2.1. Stress perpendicular to the fibre in the girder

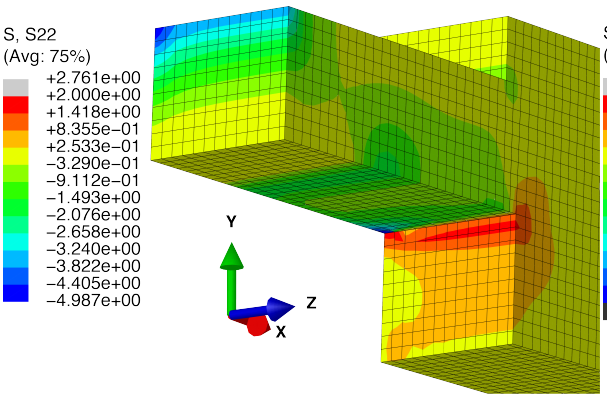

Figure 5.24: Cross section of the heel tenon with the stress perpendicular to the fibre $[N/mm^2]$

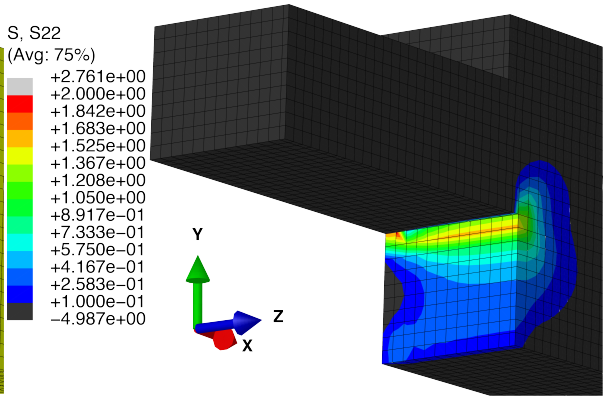

Figure 5.25: Cross section of the heel tenon with the tension stress perpendicular to the fibre $[N/mm^2]$

The contour plots in figure 5.24 and 5.25 show the cross section along the middle of the girder. Figure 5.24 and 5.25 displays the heel side. The stress perpendicular to the fibre corresponds with the found contact pressures by:

- Bigger stresses on the edge of the beam.
- Compression stress at the top end of the tenon.
- A wide area of compression stress matching with contact area e.

The biggest tension stresses are located under the tenon pit. The tension stresses present are around $1,6\ N/mm^2$ this stress is present along the width of the girder, with an exception of the girder edges. These stresses are the maximum tension stress at the heel side.

Figure 5.26 and 5.27 show the stresses in the mitre side. The stress shown in the contour plots corresponds with the contact pressures by:

- Bigger stresses on the edge of the beam.
- No compression stress at the top end of the tenon.
- A wide area of compression stress matching with contact area e.

The tension stresses at the mitre tenon pit are larger than in the heel side. An possible explanation is that the contact stress at area e in the mitre are less spread out, due to the smaller distance to the tenon pit. The non local maximum tension stress is around $2,0\ N/mm^2$.

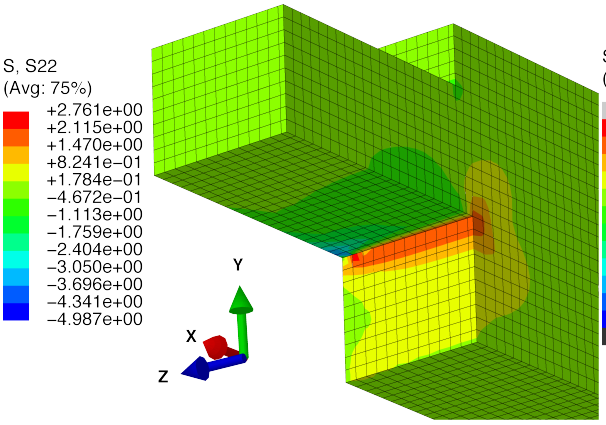

Figure 5.26: Cross section of the mitre tenon with the stress perpendicular to the fibre $[N/mm^2]$

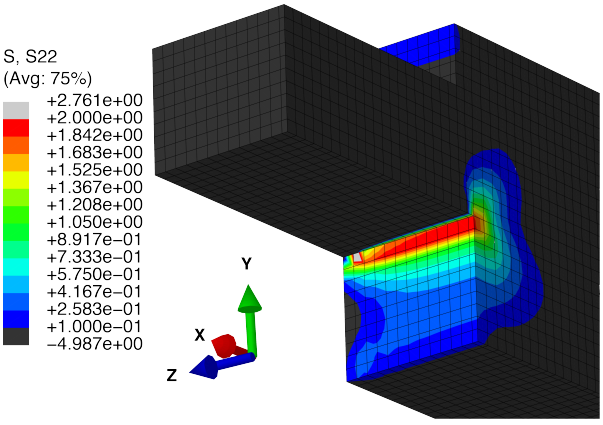

Figure 5.27: Cross section of the mitre tenon with the tension stress perpendicular to the fibre $[N/mm^2]$

5.2.2. Stress perpendicular to the fibre in the posts

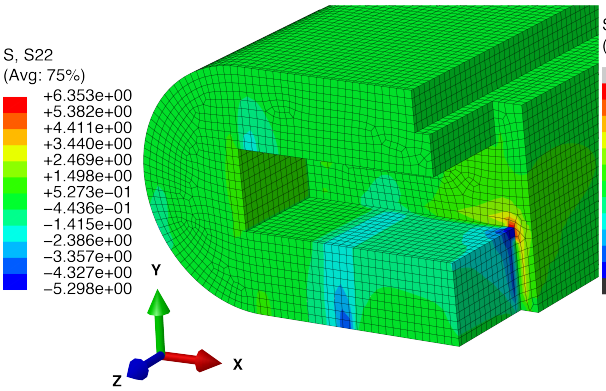

Figure 5.28: Cross section of the heel post with the stress perpendicular to the fibre $[N/mm^2]$

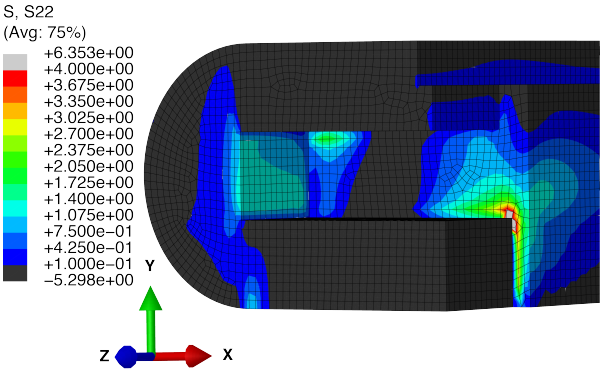

Figure 5.29: Cross section of the heel post with the tension stress perpendicular to the fibre $[N/mm^2]$

The contour plot of the cross section of the heel post show a local peak at the corner of the mortise in figure 5.28 and figure 5.29. The stress perpendicular to the fibre in the heel post corresponds with the found contact pressures in:

- Bigger stresses on the edge of the beam.
- Compression stress at the top end of the mortise.
- A wide area of compression stress matching with contact area e.

The first observation is, the tension stress that is present at the support. In reality this support will be a contact support making it impossible to transfer tension stresses. The clamping of the tenon results in a compression stress at the top end of the mortise. This compression stress will result in a tension right behind the end of the mortise. The side of the mortise corresponds with contact area a and contains two areas of tension stresses. The area to the back of the mortise is the result of the compression stress at the top end of the tenon. The area at the start of the mortise is the result of the compression area at the bottom of the tenon. The maximum tension stresses decreases along the length of the post. The non local maximum tension stresses at area at the entrance of the mortise is around 4 N/mm^2

The contour plot of the cross section of the mitre post show a local peak at the corner of the mortise in figure 5.30 and 5.31. The stress perpendicular to the fibre in the heel post corresponds with the found contact pressures in:

- Bigger stresses on the edge of the beam.
- No compression stress at the top end of the mortise.
- A wide area of compression stress matching with contact area e.

Due to the lack of the compression stress at the top of the tenon. Only one tension area on the side of the mortise is present. This is the result of the compression area at the bottom of the tenon. This maximum tension stresses decreases along the length of the post. The non local maximum tension stress is around 3,5 kN/mm^2

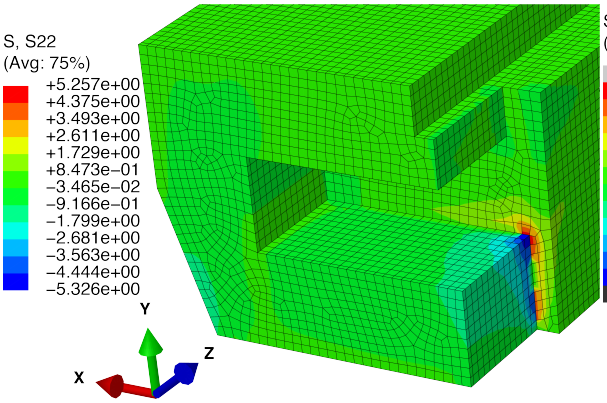

Figure 5.30: Cross section of the heel post with the stress perpendicular to the fibre $[N/mm^2]$

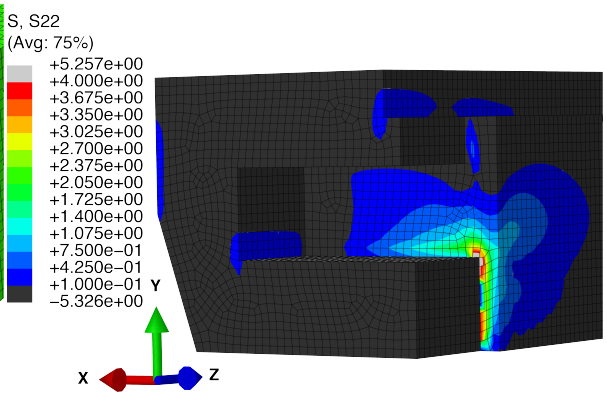

Figure 5.31: Cross section of the heel post with the tension stress perpendicular to the fibre $[N/mm^2]$

5.2.3. Result comparison with literature

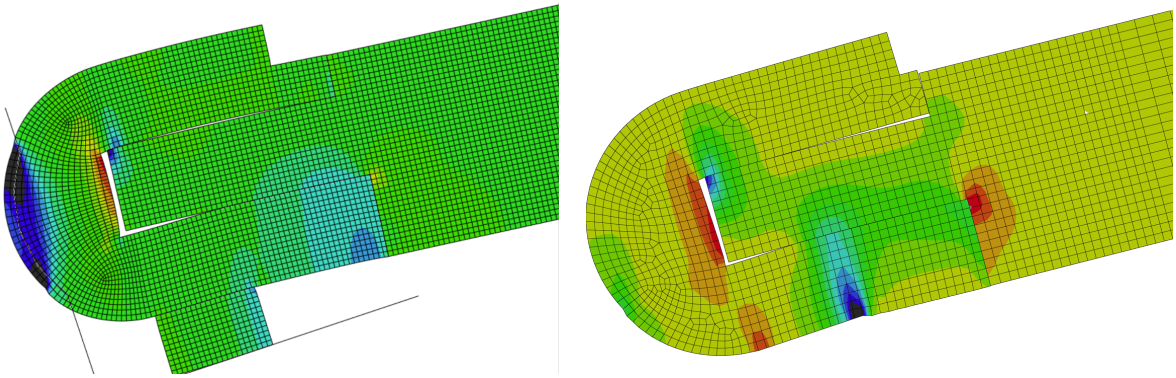

Figure 5.32: Stress perpendicularity to the grain S_{22}. Result from van Otterloo (2013) fig. 68 (Left) and the 3D model (right)

The middle cross section of the post and beam are shown on the right in figure 5.1. This is visual compared with the stress distribution of van Otterloo (2013) on the left. The following observations are done:

- The supports are different. The contact supports with friction and the springs of van Otterloo (2013) differ from the roll supports used in this thesis. This results in a different stress distribution.
- Both show a tension stress (the red areas) at the pit.
- The clamping of the tenon is present in both figures. Shown by compression (the blue area) at the top of the tenon.
- The tension stress at the back of the mortise is present in both figures.

5.2.4. Tension strength of the timber perpendicular to the grain

The characteristic tension strength perpendicular to the fibre of timber according the NEN-EN 338 (2016) is $0,4\ N/mm^2$ for softwood and $0,6\ N/mm^2$ for hardwood. This is a low strength value that is used in the verifications. When looking at average values of the perpendicular tension strength of clear specimen higher values are obtained. According table 5-3a from the Wood Handbook (2010) the tension strength perpendicular to the fibre for American white spruce, a softwood is $2,5\ N/mm^2$ with a moisture content of 12%. This is more than five times higher than the value in the NEN-EN 338 (2016). Tropical hardwood are not given in the table 5-3a of the Wood Handbook (2010). A tension strength perpendicular to the fibre for American white oak a hardwood is $5,5\ N/mm^2$ with a moisture content of 12%. This is also higher than the value given in the NEN-EN 338 (2016). The tension strength perpendicular to the fibre of azobé is unknown. A tension strength perpendicular to the fibre of $5,5\ N/mm^2$ is assumed, the same as American white oak strength, because both are hardwood with a high density.

5.3. Conclusions on the results of the finite element model

The model is assumed valid true force equilibrium, by making use of contact stresses.

The finite element model shows that the contact pressures between the tenon and the mortise are unevenly distributed in the x and z-direction. At the heel joint a clamping in the mortise is present with an influence of the seal strip support as shown in figure 5.11. The mitre joint has no clamping in the mortise at an angle of $18,5°$ degrees. Both modelled joints transfer the forces different than calculated by case 1 and 2. Different gate angles will result in a change of the normal force in the x-direction as calculated in paragraph 3.3.1. This is the only big difference between the different gate angles between 15° and 30° degrees. This results in a different inside outside chest stress distribution ratio.

The stresses parallel to the fibre show that parts of the force in the y-direction are transferred via the 3D effect. The tension stresses in the y-direction in the corners of the mortise, in the post are the biggest at the heel post around $4,0$ kN/mm^2. The tension force under the pit of the tenon in the girder are the biggest in the mitre joint around the value of $2,0$ kN/mm^2. Without knowing the tension strength perpendicular to the fibre of azobé it assumed as $5,5$ N/mm^2. This strength is without safety factors. The found stresses does not exceed the assumed strength.

A 3D finite element is better suitable for a mortise and tenon joint than a 2D model. The mt joint is a 3D connection and when a 2D model is used, the 3D behaviours needs to be incorporated. Without fully understanding possible 3D behaviours of the mt joint, it is not possible to incorporate this behaviours in a 2D model.

6

Analytical derivation of the shear strength of a tenon beam

In previous paragraph 2.5. on the remarks of the Eurocode 5 is explained that the Eurocode 5 verification for the notched beam is not valid for the mortise and tenon joint. In this chapter a derivation is done to obtain an strength equation for a tenon beam. This equation will still not be valid for the mt joint in a lock gate. The water pressure on the gate results in a unevenly distributed contact pressure on the tenon. That is why this equation will not be valid for this case, because equation 6.1 assumes a constant shear force V. Despite its applicability in this load case this derivation is done to get more knowledge about the behaviour of the tenon beam.

The derivation of the theoretical tenon beam strength is based on the derivation of notched strength by Gustafsson (1988). The tenon beam is split in a symmetric half according figure 6.1 and 6.2. The energy balance for a tenon beam and a notch beam are exactly the same. This results in the equation 6.1, for potential energy equal to the fracture energy per crack area, where the shear force V is constant.

$$\frac{V_f}{b\alpha d} = \sqrt{\frac{2G_c}{b\alpha^2 d} / \frac{\Delta\left(\frac{\delta}{V}\right)}{\Delta\beta}} \tag{6.1}$$

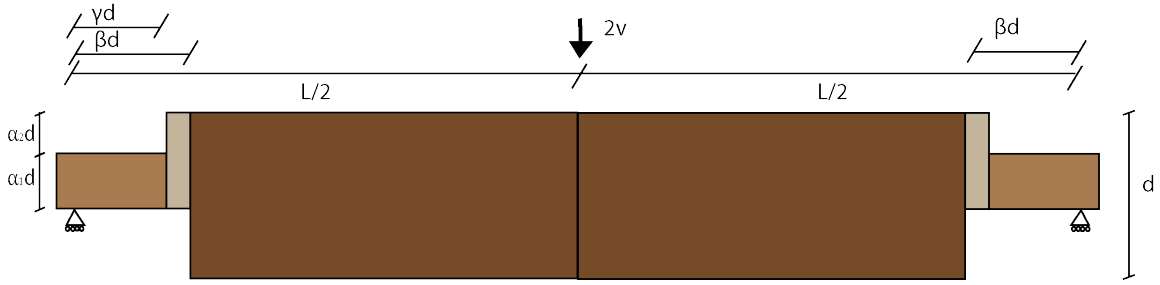

Figure 6.1: Tenon beam subjected to a point load

6.1. Derivation of the displacement for a tenon beam

The big difference between the tenon and notch beam is the geometry. The deflections needed for the derivation, are depended on the geometry of the tenon. The total deflections are described by equation 6.2. All the deflections are derived with the tenon geometry, shown in figure 6.2.

$$\delta_{t,t} = \delta_{l,t} + \delta_{v,t} + \delta_{e,t} + \delta_{r,t} \tag{6.2}$$

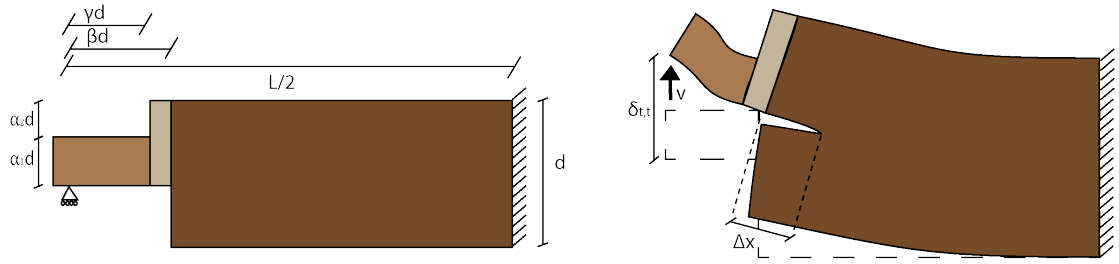

Figure 6.2: Half of the tenon beam subjected to a point load

6.1.1. Local, shear and bending displacement

The local deformation $\delta_{l,t}$, is the deformation of the material at the support and the location of the load. The local deformation is independent of β, and therefore not needed.

Figure 6.2 shows that the beam is split in three areas. This is done because it is not possible to incorporate α_2 in the deflection equations when two areas are used. It does not matter on which height the cantilever is located, for the deflection differential equation, that uses two areas such as the notched beam. Different α_2 values with two areas, will result in the same deflection equation.

The shear deflection $\delta_{v,t}$, is the deflection as a result of the shear modules from the material. The shear deflection is obtained by using the differential equation for a shear beam. The shear beam is divided in three fields shown in figure 6.3 to obtain the deflection according equation 6.3. This equation is obtained by solving the differential equation with boundary conditions that are included in appendix a. The deflection is multiplied with the factor 1,2 for the parabolic shear stress.

$$\delta_{v,t} = \frac{1,2V}{G_{xy}\left(\alpha_1+\alpha_2\right)b\alpha_1 d}\left(-\alpha_1^2\beta d-\alpha_1\alpha_2\beta d+0,5\alpha_1^2 L+0,5\alpha_1\alpha_2 L+\alpha_1\beta d+\alpha_2 d\gamma\right) \tag{6.3}$$

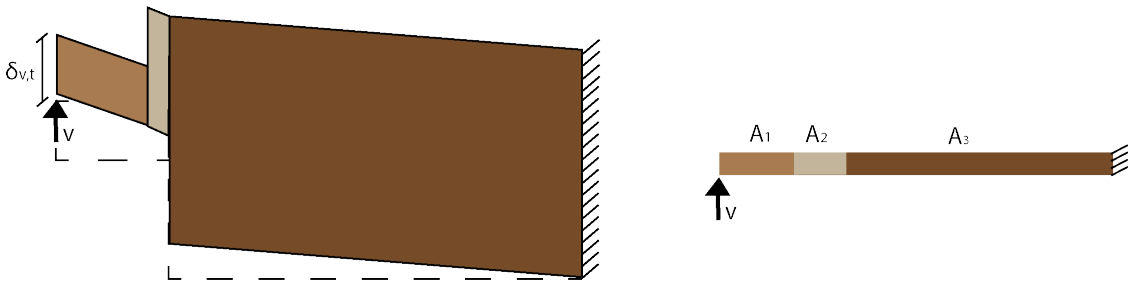

Figure 6.3: Shear displacement of the tenon

The bending deflection $\delta_{e,t}$, is the deflection as a result of the Young's modules of the material. The bending deformation is obtained by using the differential equation for an bending beam. Also the bending beam is divided in three fields shown in figure 6.4 to obtain the deflection according equation 6.4. This equation is obtained by solving the differential equation with boundary conditions that are included in appendix a.

$$\begin{aligned}\delta_{e,t} = \frac{V}{E_x b\alpha_1^3 d^3\left(\alpha_1^3+3\alpha_1^2\alpha_2+3\alpha_1\alpha_2^2+\alpha_2^3\right)}&\left(-4\alpha_1^6\beta^3 d^3-12\alpha_1^5\beta^3 d^3\alpha_2-12\alpha_1^4\beta^3 d^3\alpha_2^2-4\alpha_1^3\beta^3 d^3\alpha_2^3+0,5\alpha_1^6 L^3\right.\\&\left.+1,5\alpha_1^5 L^3\alpha_2+1,5\alpha_1^4 L^3\alpha_2^2+4\alpha_1^3\beta^3 d^3+0,5\alpha_1^3 L^3\alpha_2^3+12\alpha_1^2 d^3\gamma^3\alpha_2+12\alpha_1 d^3\gamma^3\alpha_2^2+4d^3\gamma^3\alpha_2^3\right)\end{aligned} \tag{6.4}$$

When $\gamma = \beta$ both equations for shear displacement equation 6.3 and bending displacement equation 6.4 become the shear displacement and bending displacement found by from Gustafsson (1988). This is right because, in the deflection differential equation it does not matter at what height the cantilever is fixed.

6.1.2. Simplification of the displacement equations

The equations 6.3 and 6.4 are large equations. In the method from Gustafsson (1988) the displacements are divided by V and differentiated with respect to β as shown in equation 6.1. This step is done for both the displacements for the notch

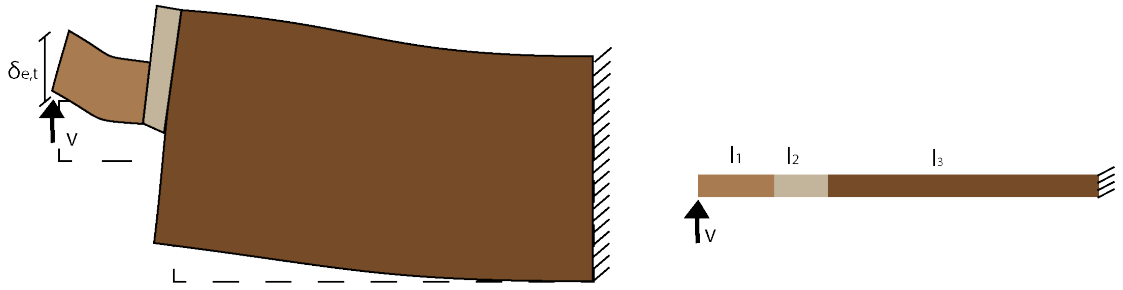

Figure 6.4: Bending displacement of the tenon

and tenon beams. The differentiated notch displacements are equation 6.5 and 6.7. The differentiated tenon displacements are equation6.6 and 6.8.

$$\frac{\partial(\delta_{v,n}/V)}{\partial\beta} = d_{v,n} = \frac{-1,2\,(\alpha_1-1)}{G_{xy}b\alpha_1} \tag{6.5}$$

$$\frac{\partial(\delta_{v,t}/V)}{\partial\beta} = d_{v,t} = \frac{-1,2\,(\alpha_1+\alpha_2-1)}{G_{xy}b\,(\alpha_1+\alpha_2)} \tag{6.6}$$

$$\frac{\partial(\delta_{e,n}/V)}{\partial\beta} = d_{e,n} = \frac{-12\beta^2\left(\alpha_1^3-1\right)}{E_x b\alpha_1^3} \tag{6.7}$$

$$\frac{\partial(\delta_{e,t}/V)}{\partial\beta} = d_{e,t} = \frac{-12\beta^2\left((\alpha_1+\alpha_2)^3-1\right)}{E_x b\,(\alpha_1+\alpha_2)^3} \tag{6.8}$$

The found equations for the shear and bending differentiated displacements, have shown close resemblance to each other. A notch to tenon transformation factor is introduced according to the equations 6.9 and 6.10. This leads to a transformation factor depended of α_1 and α_2. The transformation factors are equation 6.11 and 6.12.

$$d_{v,n}C_{v,t} = d_{v,t} \tag{6.9}$$

$$d_{e,n}C_{e,t} = d_{e,t} \tag{6.10}$$

$$C_{v,t} = \frac{(\alpha_1+\alpha_2-1)\,\alpha_1}{(\alpha_1+\alpha_2)\,(\alpha_1-1)} \tag{6.11}$$

$$C_{e,t} = \frac{\left((\alpha_1+\alpha_2)^3-1\right)\alpha_1^3}{(\alpha_1+\alpha_2)^3\left(\alpha_1^3-1\right)} \tag{6.12}$$

6.1.3. Mathematical Derivation of the rotational sprint stiffens in a tenon beam

The rotational deflection $\delta_{r,t}$, is a deflection as a result of the elastic clamping of the cantilever βd. This clamping is modelled with a rotational spring c $[1/Nm]$. This will lead to the deflection of $\delta_{r,t} = cV\beta^2 d^2$. The equation will be different for a tenon beam. The derivation of c from Gustafsson (1988) as explained in previous paragraph 2.4.3. is flowed to obtain a c for the tenon beam.

The transformation factors shown in equation 6.11 and 6.11 are dependent on β. This results in that those factors can be used on the displacements when only considering elements dependent on β. This will lead to the equations 6.13 and 6.14. Where the transformation factors are multiplied with the matching notch displacement to obtain the tenon displacement depending on βd. The total displacement is written as the equation 6.15.

$$\delta_{v,t} = C_{v,t}\frac{1,2V\beta d}{G_{xy}bd}\left(\frac{1}{\alpha_1}-1\right) + constant \tag{6.13}$$

$$\delta_{e,t} = C_{e,t}\frac{V\left(\beta d\right)^3}{3E_x bd^3/12}\left(\frac{1}{\alpha_1^3}-1\right) + constant \tag{6.14}$$

$$\delta_{t,t} = A\left(B+\beta d\right)^3 + constant = A\left(\beta d\right)^3 + 3AB\left(\beta d\right)^2 + 3AB^2\left(\beta d\right) + AB^3 + constant \tag{6.15}$$

The total displacement equation 6.15 is a polynomial of βd. Both the shear displacement equation 6.13 and the bending displacement equation 6.14 are dependent on βd and $(\beta d)^3$. Matching the βd's of the shear and bending displacement to the total displacement shows how the values for A and B are obtained. This is shown in equation 6.16 and 6.17.

$$\begin{aligned} A(\beta d)^3 &= \delta_{e,t} \\ A = \frac{\delta_e}{(\beta d)^3} &= \frac{C_{e,t}V}{3E_x bd^3/12}\left(\frac{1}{\alpha^3}-1\right) \end{aligned} \tag{6.16}$$

$$\begin{aligned} 3AB^2(\beta d) &= \delta_{v,t} \\ B = \sqrt{\frac{\delta v,t}{3A(\beta d)}} &= d\sqrt{\frac{C_{v,t}E_x}{10C_{e,t}G_{xy}}\frac{(1/\alpha-1)}{(1/\alpha^3-1)}} \end{aligned} \tag{6.17}$$

The rotational deflection equation 6.19 is dependent of $(\beta d)^2$ this is corresponds with the second term in equation 6.15. The previous calculated A and B makes it possible to calculate a c value.

$$\begin{aligned} \delta_{r,t} &= cV(\beta d)^2 = 3AB(\beta d)^2 \\ c = \frac{3AB}{V} &= \sqrt{C_{v,t}C_{e,t}}\frac{12}{b\alpha^2 d^2}\sqrt{\frac{(1-\alpha)(1-\alpha^3)}{10G_{xy}E_x}} \end{aligned} \tag{6.18}$$

The c value is obtained using both transformation factors in equation 6.18. Isolation both transformation factors results in the transformation factor of the spring $C_{r,t} = \sqrt{C_{v,t}C_{e,t}}$. This will lead to the rotation displacement equation 6.19 for $\delta_{r,t}$, where a c value id found by gustafsson (1988) as shown in figure 6.5.

$$\delta_{r,t} = C_{r,t}cV\beta^2 d^2 \tag{6.19}$$

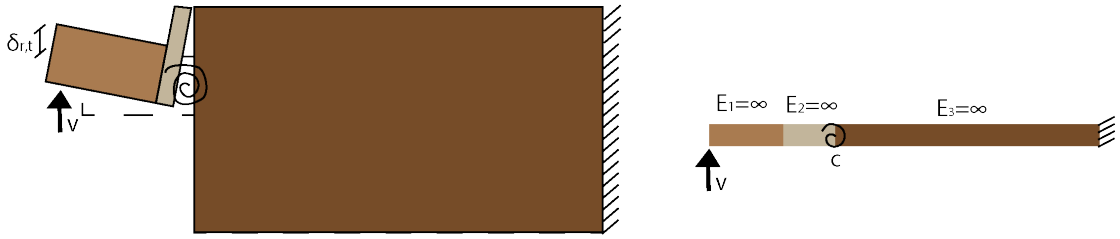

Figure 6.5: Rotation displacement of the tenon

6.1.4. Total displacement of the tenon beam

In this thesis two tenon displacements are used. Displacement one where $c = 0$ and displacement two is where $c \neq 0$ where c is assumed equation 6.18, the above explained mathematical obtained c.

Rotational spring stiffness assumed zero

It is assumed that there is no displacement, due to rotation at the tenon. The interface between tenon and the beam in figure 6.5 is assumed fixed, this results in $c = 0$. The total displacement will become equation 6.20.

$$\begin{aligned} \delta_{t,t} &= D\beta d + F(\beta d)^3 + constant \\ D &= \frac{1{,}2VC_{v,t}(1/\alpha_1-1)}{G_{xy}bd} \\ F &= \frac{12VC_{e,t}(1/\alpha^3-1)}{3E_x bd^3} \\ C_{v,t} &= \frac{(\alpha_1+\alpha_2-1)\alpha_1}{(\alpha_1+\alpha_2)(\alpha_1-1)} \\ C_{e,t} &= \frac{((\alpha_1+\alpha_2)^3-1)\alpha_1^3}{(\alpha_1+\alpha_2)^3(\alpha_1^3-1)} \end{aligned} \tag{6.20}$$

Rotational spring stiffness mathematical obtained

Using the method of Gustafsson (1988) the total displacement of equation 6.21 is found for the tenon beam. This is the total displacement with the assumption of $c \neq 0$ with c mathematical obtained to make it possible to write it as 6.21.

$$\begin{aligned}
\delta_{t,t} &= A\left(B+\beta d\right)^3 + constant \\
A &= \frac{VC_{e,t}}{3E_x bd^3/12}\left(1/\alpha_1^3-1\right) \\
B &= d\sqrt{\frac{E_x C_{v,t}}{10G_{xy}C_{e,t}}\frac{(1/\alpha_1-1)}{(1/\alpha_1^3-1)}} \\
C_{v,t} &= \frac{(\alpha_1+\alpha_2-1)\alpha_1}{(\alpha_1+\alpha_2)(\alpha_1-1)} \\
C_{e,t} &= \frac{\left((\alpha_1+\alpha_2)^3-1\right)\alpha_1^3}{(\alpha_1+\alpha_2)^3(\alpha_1^3-1)}
\end{aligned} \tag{6.21}$$

Boundaries of the total displacements
Both total displacement are depended on βd as shown in equation 6.20 and 6.21. Both will have two clear boundaries $\alpha_2 = 0$ and $\alpha_1 + \alpha_2 = 1$. The displacement is independent of βd when $\alpha_1 + \alpha_2 = 1$. The assumed failure mechanism: cracking in the pit, will not happen because there is no tenon. When $\alpha_2 = 0$ the transformation factors $C_{v,t}$ and $C_{e,t}$ will become 1, this is equal to the displacement equations for the notched beam.

6.2. Shear strength for a tenon beam

The total displacements in equation 6.20 and 6.21 is substituted in the equation 6.1 for the shear strength. This way equation for the shear strength for a tenon beam is obtained. The steps are written down in appendix b. The shear strength 6.22 assumes a c that is mathematical obtained. Equation 6.23 assumes $c = 0$ resulting in a different shear strength.

$$\begin{aligned}
\frac{V_f}{b\alpha_1 d} &= \frac{\sqrt{\frac{G_c}{d}}}{\sqrt{\frac{0{,}6C_{v,t}\left(\alpha_1-\alpha_1^2\right)}{G_{xy}}}+\beta\sqrt{\frac{6C_{e,t}\left(\frac{1}{\alpha_1}-\alpha_1^2\right)}{E_x}}} \\
C_{v,t} &= \frac{(\alpha_1+\alpha_2-1)\alpha_1}{(\alpha_1+\alpha_2)(\alpha_1-1)} \\
C_{e,t} &= \frac{\left((\alpha_1+\alpha_2)^3-1\right)\alpha_1^3}{(\alpha_1+\alpha_2)^3(\alpha_1^3-1)}
\end{aligned} \tag{6.22}$$

$$\begin{aligned}
\frac{V_f}{b\alpha_1 d} &= \sqrt{\frac{5G_c}{3d\left(\frac{C_{v,t}\left(\alpha_1-\alpha_1^2\right)}{G_{xy}}+10\beta^2\frac{C_{e,t}\left(1/\alpha_1-\alpha_1^2\right)}{E_x}\right)}} \\
C_{v,t} &= \frac{(\alpha_1+\alpha_2-1)\alpha_1}{(\alpha_1+\alpha_2)(\alpha_1-1)} \\
C_{e,t} &= \frac{\left((\alpha_1+\alpha_2)^3-1\right)\alpha_1^3}{(\alpha_1+\alpha_2)^3(\alpha_1^3-1)}
\end{aligned} \tag{6.23}$$

The fracture energy per crack area G_c is unknown. In this derivation the fracture mode already assumed fracture mode 1 according figure 6.6. This results in $G_c = G_{f,y}$. This assumption is made on the base that, the at least half of the height of the cantilever, is on the tension stress side of the beam. This results in a new bottom boundary according to equation 6.24.

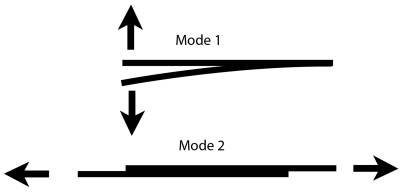

Figure 6.6: Possible fracture mode 1 and mode 2

$$\alpha_2 \leq 1-\alpha_1-\alpha_2 \Rightarrow \alpha_1 \leq (1-2\alpha_2) \tag{6.24}$$

It is unknown if this this assumption is right. This assumption depends on the value of $G_{f,y}$ and $G_{f,x}$, and also on possible combined failure modes of modes 1 and 2 are possible. Some theoretical $C_{v,t}$ and $C_{e,t}$ values are shown in tables 6.1 and 6.2. The transformation factor will lower the deflection depended of βd by multiplying it the corresponding notch

Table 6.1: $C_{v,t}$ values for different α_1 [−] and α_2 [−]

	$\alpha_2 = 0$	$\alpha_2 = 1/10$	$\alpha_2 = 1/5$	$\alpha_2 = 1/4$	$\alpha_2 = 1/3$	$\alpha_2 = 2/5$
$\alpha_1 = 1/5$	1,00	0,58	0,38	0,31	0,22	0,17
$\alpha_1 = 1/4$	1,00	0,62	0,41	0,33	0,24	Eq. 6.24 not valid
$\alpha_1 = 1/3$	1,00	0,65	0,44	0,36	0,25	Eq. 6.24 not valid
$\alpha_1 = 2/5$	1,00	0,67	0,44	0,36	Eq. 6.24 not valid	Eq. 6.24 not valid
$\alpha_1 = 2/4$	1,00	0,67	0,43	0,33	Eq. 6.24 not valid	Eq. 6.24 not valid
$\alpha_1 = 2/3$	1,00	0,61	Eq. 6.24 not valid	Eq. 6.24 not valid	Eq. 6.24 not valid	Eq. 6.24 not valid

Table 6.2: $C_{e,t}$ values for different α_1 [−] and α_2 [−]

	$\alpha_2 = 0$	$\alpha_2 = 1/10$	$\alpha_2 = 1/5$	$\alpha_2 = 1/4$	$\alpha_2 = 1/3$	$\alpha_2 = 2/5$
$\alpha_1 = 1/5$	1,00	0,29	0,12	0,08	0,05	0,03
$\alpha_1 = 1/4$	1,00	0,35	0,16	0,11	0,06	Eq. 6.24 not valid
$\alpha_1 = 1/3$	1,00	0,43	0,22	0,16	0,11	Eq. 6.24 not valid
$\alpha_1 = 2/5$	1,00	0,48	0,25	0,18	Eq. 6.24 not valid	Eq. 6.24 not valid
$\alpha_1 = 2/4$	1,00	0,52	0,27	0,20	Eq. 6.24 not valid	Eq. 6.24 not valid
$\alpha_1 = 2/3$	1,00	0,51	Eq. 6.24 not valid	Eq. 6.24 not valid	Eq. 6.24 not valid	Eq. 6.24 not valid

deflection dependend of βd. Chapter 7 uses test data to compare the theoretical tenon strength (TTS) equation 6.22 and (TTS $c = 0$) equation 6.23 for two different α_1 and α_2 combinations.

6.3. Linear fracture energy for azobé

The linear fracture energy for azobé remains unknown. Van Otterloo (2013) used the solve function of Excel with his test data to obtain a function for the fracture energy. The solve function minimizes the sum of squares in the linear regression, for the differences between the modelled value and value according the test of van Otterloo (2013). The solve function optimize the variables a to e in the linear equation 6.25.

$$G_{f,y} = a\rho + b\omega + cE_1 + dG_{12} + e \tag{6.25}$$

$$G_{f,y} = 5.36 \cdot 10^{-4}\rho + 4.15 \cdot 10^{-5}E_1 \tag{6.26}$$

The equation for the fracture energy found by van Otterloo (2013) is equation 6.26. In this equation are: $G_{f,y}$ $[N/m]$ the fracture energy in pure tensile splitting perpendicular to the grain, ρ $[kg/m^3]$ the density, ω [%] the moisture content, E_1 $[N/mm^2]$ the elasticity parallel to the fibre, G_{12} $[N/mm^2]$ the shear modulus. This results in a higher fracture energy that when the formula from Larsen and Gustafsson (1990) for softwood is used.

The equation 6.26 is used to obtain the fracture energy for azobé because it leads to better predicted fracture energy's for azobé. Further research on fracture energy of azobé and other hardwoods is needed.

7

Tested tenon strength

In previous research tenon beams where tested by Vermeij (2011) and van Otterloo (2013). The results of these tests are used in this chapter and compared with the found analytic expression for tenon beams in the previous chapter 6.

The spruce tenon tests of Vermeij (2011) are used to compare to the theoretic tenon strength TTS expressions. This is included in this thesis because the material properties for European spruce are well known in comparison with azobé. The test of van Otterloo (2013) were done on azobé. Those tests include two variations of tenon beam geometry.

All tests were done on a small number of test samples. More tests are needed for a bigger variation of test samples. More tests will lead to a better insight in the tenon strength. These small scale tests can be used as an indication for possible influences of different properties. The proposed TTS expressions in chapter 6 are used to calculate the strength of a tenon beam. Those expressions are used as an indication of the strength. More research is needed to obtain a final expression.

The test results and the values from the tests and expressions are shown as: average μ, coefficient of variation (COV) and 5^{th} the percentile value $x_{5\%}$. The COV is calculated according equation 7.1, σ is the standard deviation and μ is the average. The graphs of the cumulative distributions shown in the next paragraphs are the area under the probability density function of a normal distribution. The probability density function is calculated according to equation 7.2 assuming a normal distribution of the test results. The 5^{th} percentile value is calculated according to equation 7.3 assuming a normal distribution.

$$COV = \frac{\sigma}{\mu} \tag{7.1}$$

$$f(x|\mu,\sigma^2) = \frac{1}{\sqrt{2\sigma^2\pi}} e^{-\frac{(x-\mu)^2}{2\sigma^2}} \tag{7.2}$$

$$x_{5\%} = \mu - 1{,}645\sigma \tag{7.3}$$

7.1. Previous experimental programs

The used datasets on tenon beams in this thesis are obtained by using the datasets from two previous studies by Vermeij (2011) and van Otterloo (2013). The datasets will be used to to compare, the analytic derived theoretic tenon strength TTS in the previous chapter. In this paragraph both studies will be explained and discussed both studies are used in the next paragraph for comparing the TTS with of the obtained fail stress of the tenon.

7.1.1. Experimental program Vermeij (2011)

The reduced shear method in paragraph 6.5.2 from NEN-EN 1995-1-1 (2005) for hardwood tenon beams is tested in the Bachelor thesis of Vermeij (2011). In this research tests were done to compare, the formulas given by the Eurocode 5. Four kinds of geometric set-ups where tested: notch beams, tenon beams, inclined notch beams and inclined tenon beams. In this research only the dataset of the tenon beams are used.

Two kind of wood species were used in the tests, spruce from Scandinavia and azobé from Cameroon. The timber beams where stored, before and in between the tests, in a climate room with a constant humidity and temperature. The mother timber beams where subjected to non-destructive testing, to obtain the dynamic modulus of elasticity. The dynamic modulus of elasticity is dependent on the specific weight and the wave speed measured in the timber by using the timber

grader MTG. According the dynamic modulus of elasticity the spruce belongs in the C30 grade and the azobé in the D70 grade. The azobé beams with too much grain deviation where excluded from the analysis.

The geometry of the test pieces are shown in figure **??**. The width of the tenon beams are 30 mm. After making the test pieces from the mother timber beam, according the measures in figure **??**. No new exact measurements per test pieces were made. This means that the intended measurements from figure **??** are used in the analysis instead of individual measurements.

Figure 7.1: Beam dimensions [mm] of the tenon beams tested by Vermeij (obtained from [27], fig. 4.1)

The tenon beams are subjected to an asymmetric 4-point-bending test, shown in figure **??**. The asymmetric test makes it possible to calculate the side of the tenon failure. After failure on one side, the side gets repaired and set-up for a second test on the other side. Only the failure load is reported by Vermeij (2011). The tables regarding this dataset are included in appendix c.

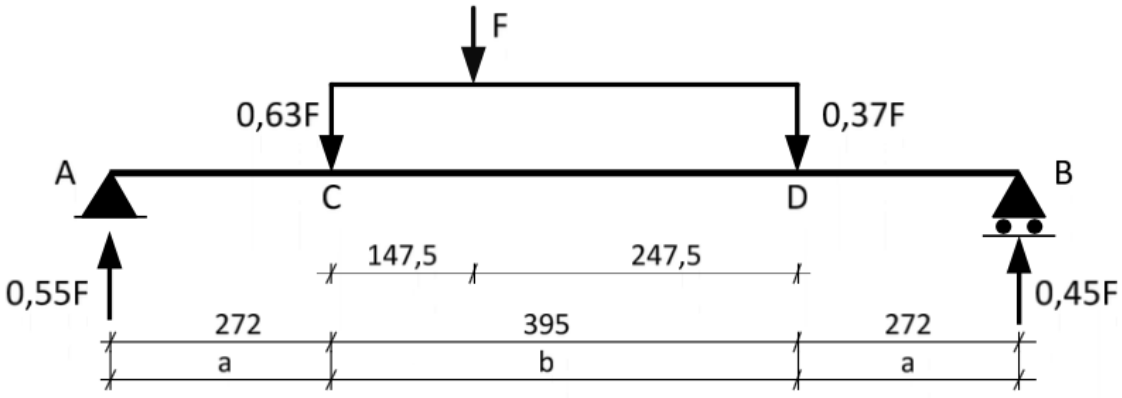

Figure 7.2: Test setup of Vermeij dimentions in [mm] (obtained from [27], fig. 4.5)

The gathered data by Vermeij (2011) that is used in this thesis are:

- Density and dynamic modulus of elasticity of the mother beam;
- Intended measurements of the beam geometry;
- Intended measurements of the test set-ups;
- Failure loads.

7.1.2. Experimental program Van Otterloo (2013)

Van Otterloo (2013) did tests on azobé tenon beams to get a bigger understanding in tenon beam failure due to crack growth. The results from the tests where compared with the validation in the Eurocode 5. In this test two different tenon beam geometries were tested. One tenon is located at 1/3 of the top of the beam with a height of 1/3 of the beam height. The other tenon is located at 1/5 of the top with a tenon height of 2/5, the proportions of the tenon in a mitre gate. With two different cantilever lengths there are four different combinations that were tested. The dataset of all the four tests are used in this thesis.

The beams are made of azobé from Cameroon. This wood is from the same batch as the wood used by Vermeij (2011). The beams are sawn from remainders of a previous bending test where the timber strength grade of D70 was found. The dynamic modulus of elasticity is also measured for these tests. The test samples were stored in a climate room with a constant humidity and temperature. In this experimental program the grain of the beam is examined on deviations. Test specimen with too much grain deviations are left out.

In figure **??** the geometry of the test pieces are shown with a width of 25 mm. In this test the test pieces are remeasured after fabrication. This is the result of in individual measurements per test piece. Figure **??** also shows a difference in tenon length between the middle and the high tenon. The geometry of the high tenon match with the geometry of the tenon in a mortise and tenon joint in a mitre gate.

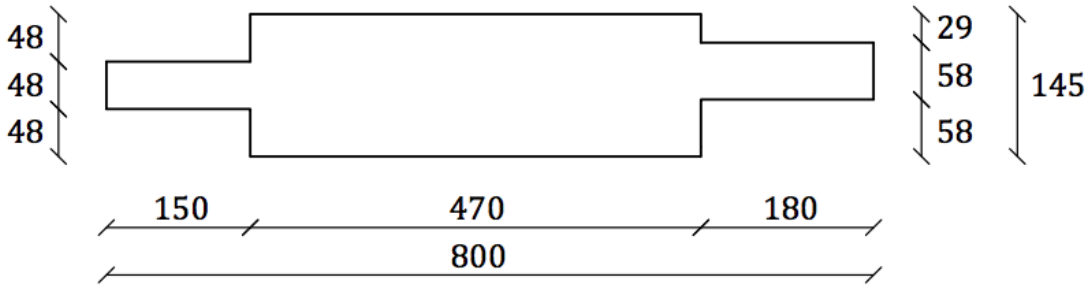

Figure 7.3: Beam dimensions [mm] of the tenon beams tested by Van Otterloo (obtained from [26], fig. 92)

The beams are set-up in a four point bending test. By aligning one force directly above the support the test set-up will become a three point bending test. Both the forces F_2 and V are transferred over a length of 50 mm and the whole width of the beam. The cantilever length of the tenons are defined as: short of 1/3 of the tenon length and long for 3/4 of the tenon length. Figure **??** shows the test set-up, in table 7.1 the intended measurement of the lengths are displayed. When the beam is placed in test bench a, b and x are remeasured to obtain individual measurements per test. After failure of one tenon the beam is reused for a second test on the other tenon. The tables regarding this dataset are included in appendix c.

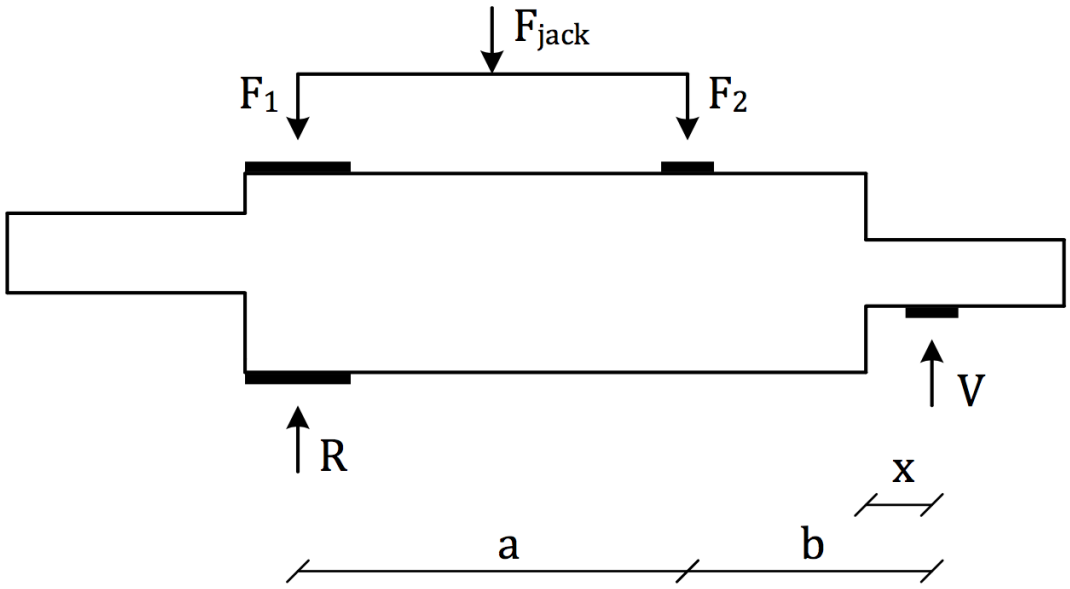

Figure 7.4: Test set-up of Van Otterloo dimensions in [mm] (obtained from [26], fig. 96)

The gathered data by van Otterloo (2013) that are used in this thesis are:

Table 7.1: Intended measurement for test set-ups

Tenon location	Middle	Middle	High	High
$x\ [mm]$	50	112,5	60	135
$b\ [mm]$	185	247,5	195	270
$a\ [mm]$	295	295	295	295

- Density and dynamic modulus of elasticity of the test beams;
- Individual measurements of the beam geometry;
- Individual measurements of the test set-ups;
- Failure loads.

7.2. Remarks on the datasets

Both datasets will be used in the next paragraph to test the analytic derived tenon strength. In this paragraph remarks about the dataset are described. The function of these remarks is to get to know the boundaries of the datasets and use those boundaries in the next paragraph.

7.2.1. Remarks on Vermeij (2011)

The biggest remark on the dataset of Vermeij (2011) is that only the intended measurements are present. The exact sizes of the test specimen are unknown, this could lower the accuracy of the test. Since only the intended measurements are used in further calculations. The exact measurement of the set-up are also unknown, this could also lower the accuracy of the test. The calculations in the next chapter are done with the intended measurements this will lead to less accurate results.

The density and modulus of elasticity are determined on the mother timber beams. Those beams are sawn in the sizes of the test pieces. Density and modules of elasticity can vary inside the timber. This can lead to different density and modules of elasticity in beams from the same mother beam. Knowing only the density and modules of elasticity of the mother beam can lead to less accurate results.

Figure 7.5 and 7.6 show the distribution functions of the density graph in figure 7.5 and modules of elasticity in figure 7.6. There is a small variation in density for the azobé beams with one exception. The modules of elasticity of the azobé beams are all in the lower 50% part of the moduli found by van Otterloo (2013) and that graph is steeper than the moduli found by Van Otterloo (2011). A steeper graph means more variation. There is a big variation in the modules of elasticity of the pine beams. It is important to know the variation in the density and modules of elasticity. Both will be used in the next chapter for calculations and can have an influence on the results.

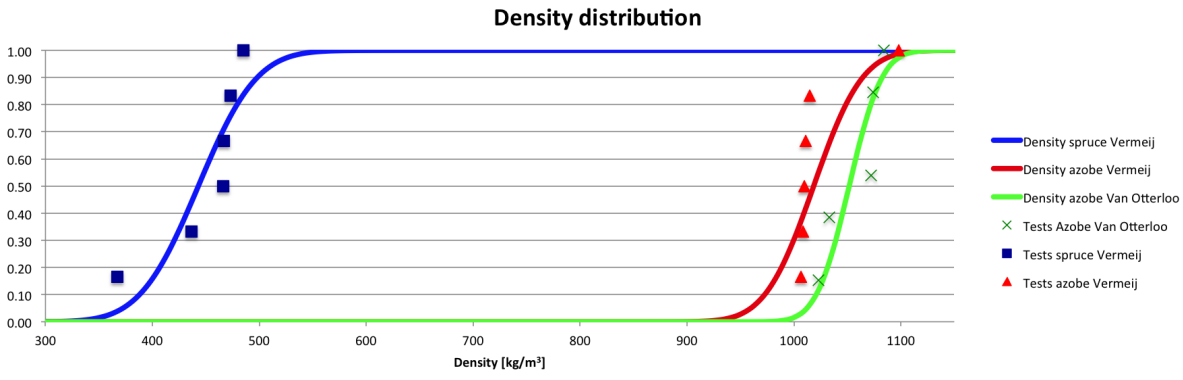

Figure 7.5: Density distribution of the tests

7.2.2. Remarks on Van Otterloo (2013)

In the tests of van Otterloo (2013) all the individual data on sizes, density, and moduli of elasticity and test set-up are written down. All these individual data can lead to more precise calculations using the individual test data. Due to the

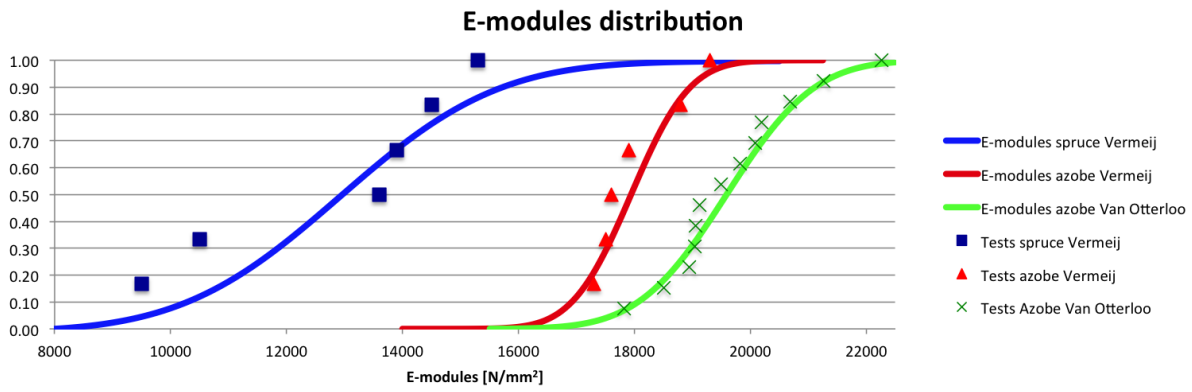

Figure 7.6: Density distribution of the tests

individual data more variation can be present in comparison with Vermeij (2011).

figure 7.5 and 7.6 show the distribution functions of the density figure 7.5 and modules of elasticity 7.6. The curve of the density is steeper than the curve found by Vermeij (2011) due to the 5 individual measured densities out of the 13 measurements. The curve from the modulus of elasticity is less steep then the curve found by Vermeij (2011). The average of van Otterloo (2013) is higher than the value found by Vermeij (2011). The variations of density and modulus of elasticity can have an influence on the results.

7.2.3. Remarks on both datasets

The gathered data from both experimental programs that are used in this thesis are: density, the dynamic modulus of elasticity, measurements of the beam geometry, measurements of the test set-ups and the failure loads. The other material properties are calculated from the gathered data. Both the modulus of shear G_{xy} $[N/mm^2]$ and the fracture energy $G_{f,y}$ $[Nm/m^2]$ are calculated from the density ρ $[kg/m^3]$ and modulus of elasticity E_x $[N/mm^2]$. This makes them dependent on the found data.

7.3. Comparison Vermeij (2011)

Two different kinds of tests are used from Vermeij (2011) the spruce tenon beam and the azobé tenon beam, they both have similar geometry's. The $G_{f,y}$ of the spruce follows from larsen and Gustafsson (1990) while the $G_{f,y}$ of the azobé is assumed according van Otterloo (2013) as disused in paragraph 6.3.

7.3.1. Comparison spruce test results analytic formulas

Table 7.2 shows that the average and the 5^{th} percentile from the theoretical tenon beam strength (TTS) are close to the the test results. The figure 7.7 and 7.8 confirm that the TTS is a close match with the test results. The graphs display that the strength for the TTS with $c = 0$ result in stronger tenons than tested.The inclination of the regression lines of the TTS models 0,7 and 0,5 are not close to 1,0 the inclination of $x = y$, where the tested shear force match the calculated shear force. This shows that possible behaviour of the tenon beam is missing in the calculation method.

Table 7.2: Reduced shear stress failure of a spruce tenon beam $[N/mm^2]$

	Average	COV	5^{th} percentile
Tests	5,1	0,20	3,4
TTS	5,0	0,14	3,8
TTS, $c = 0$	6,7	0,14	5,1
Notch strength	2,1	0,14	1,6

7.3.2. Comparison azobé test results analytic formulas

Table 7.3 shows that the average of the test is not corresponding with one of the expressions. The figures 7.9 and 7.10 show the small COV's by the narrow range of data point in figure 7.10 and the steep lines in graph 7.9. The TTS $c = 0$ is corresponding the best but remains on the conservative side. The low COV's for the equations in comparison with the

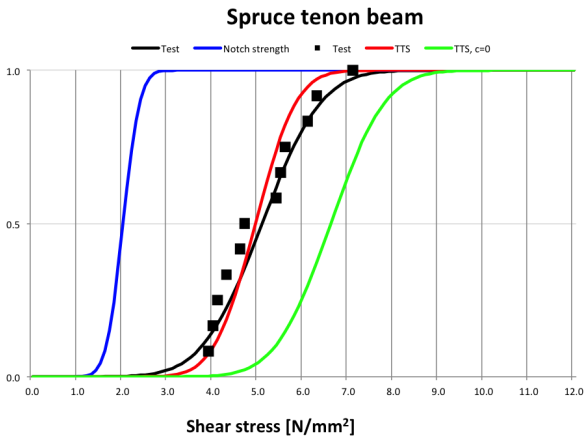

Figure 7.7: Tests results for the spruce tenon beam

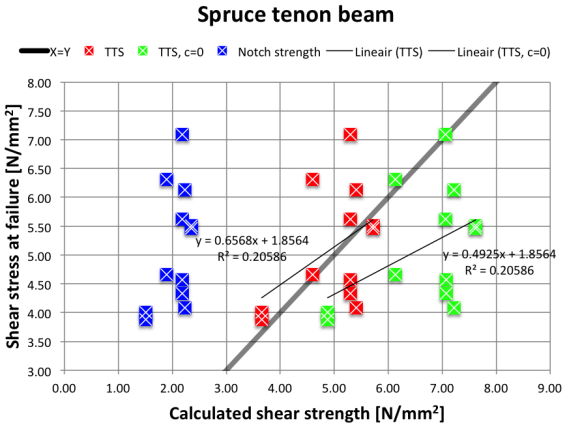

Figure 7.8: Calculated stress and fail stress comparison for the spruce tenon beam

tests can be a result of the remarks made in paragraph 7.2.1. The small spread in the modules of elasticity and only the intended geometric properties can be, one of the causes of the low COV's. The tests of van Otterloo (2013) will be studied for this big difference between the COV's. The slope of the regression line of the TTS $c = 0$ model 1,3 is closer to the $x = y$ line than that of the TTS model 1,7.

Table 7.3: Reduced shear stress failure of a azobé tenon beam $[N/mm^2]$

	Average	COV	5^{th} percentile
Tests	17,9	0,28	9,5
TTS	11,8	0,04	11,1
TTS, $c = 0$	15,8	0,04	14,8
Notch strength	4,9	0,04	4,6

7.4. Comparison van Otterloo (2013)

The tests of van Otterloo (2013) contain four different test set-ups named after the tenon location and cantilever length : middle long (ML), middle short (MS) high long (HL) and high short (HS). In paragraph 7.4.1. all individual set-ups are compared. In paragraph 7.4.2. the set-ups are combined in to four categories: middle, high, long and short. In paragraph 7.4.3. all the results are combined in one category. In the last paragraph the best calculation models are combined in one category.

7.4.1. The individual set-ups compared theoretic tenon strength

Table 7.4 shows the results of the tests, the theoretic tenon strength, the theoretic tenon strength with a $c = 0$ and the notch strength. For all the 4 test set-ups

Middle long

The average and the 5^{th} percentile of the tests from middle long set-up are close to the calculated value according to TTS. Both figures 7.11 and 7.12 show a good approximation of the test results with the calculated results. The inclinations of both regression lines are not close to 1,0. The regression line of TTS is close to the $x = y$. The calculations of the TTS $c = 0$ are too progressive while the existing calculations according the notch strength are too conservative.

Middle short

The average and the 5^{th} percentile of the tests from middle short set-up are close to the calculated value's according TTS. The COV value in the test is almost twice the size of the calculated COV. Both figures 7.13 and 7.14 show the approximation of the test results with the calculated results. Both regression lines of the TTS models are not matching the $x = y$ line. The slope of the graph of the test results is less steep that both calculated TTS values, this corresponds with the difference in

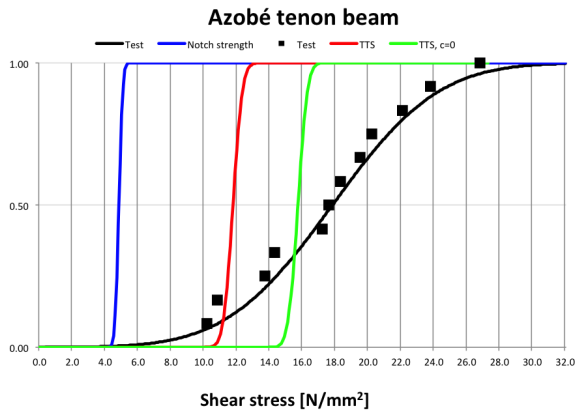

Figure 7.9: Tests results for the azobé tenon beam

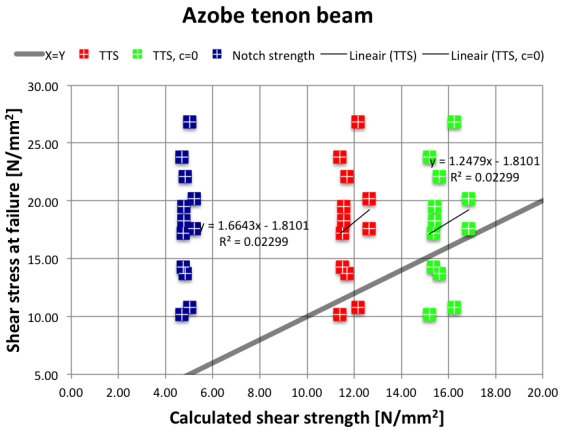

Figure 7.10: Calculated stress and fail stress comparison for the azobé tenon beam

Table 7.4: Reduced shear stress failure of a azobé tenon beam $[N/mm^2]$ for the individual set-ups

		Middle long	Middle short	High long	High short
Tests	Average	8,5	12,0	5,9	10,0
	COV	0,14	0,17	0,26	0,20
	5^{th} percentile	6,6	8,8	3,4	6,7
TTS	Average	8,0	11,4	4,8	7,2
	COV	0,09	0,08	0,05	0,05
	5^{th} percentile	6,8	9,9	4,4	6,6
TTS $c = 0$	Average	11,2	15,7	6,6	10,1
	COV	0,09	0,08	0,05	0,05
	5^{th} percentile	9,5	13,7	6,1	9,3
Notch strength	Average	2,9	4,5	2,8	4,4
	COV	0,06	0,06	0,05	0,04
	5^{th} percentile	2,6	4,1	2,6	4,0

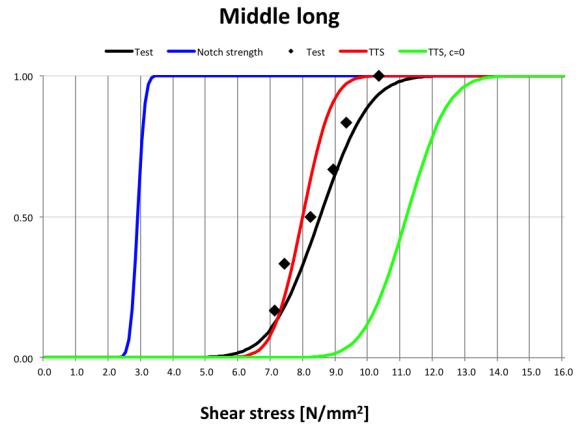

Figure 7.11: Tests results for the middle long tenon beam

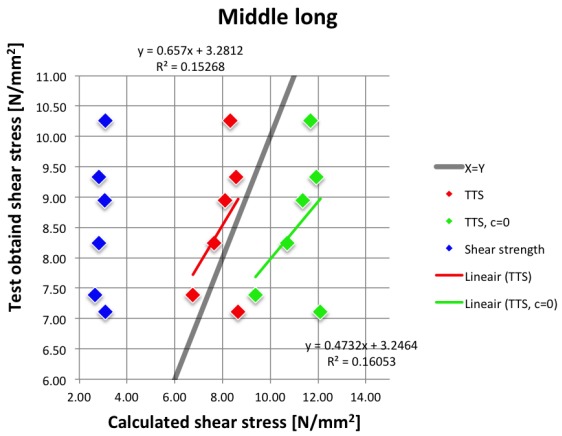

Figure 7.12: Calculated stress and fail stress comparison for the middle long tenon beam

COV value's.

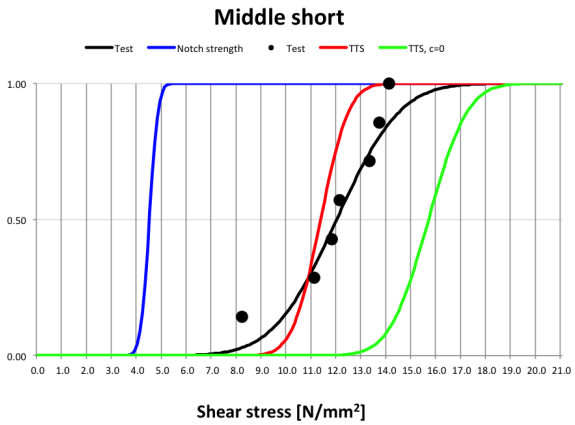

Figure 7.13: Tests results for the middle short tenon beam

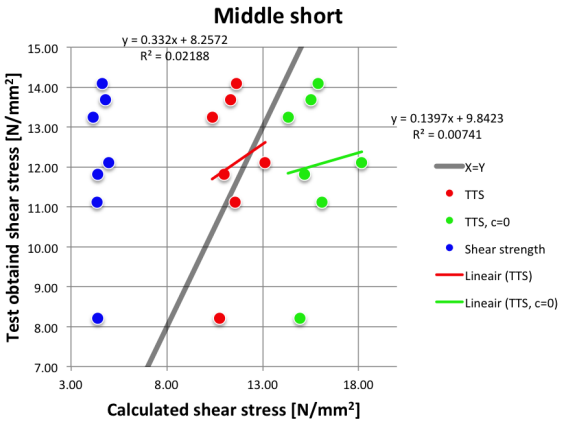

Figure 7.14: Calculated stress and fail stress comparison for the middle short tenon beam

High long

The average of the tests from the high long set-up are closer to the TTS with $c = 0$, but are more or less in the middle between both TTS methods. The COV from the test is high in comparison with the calculated COV's. This is also illustrated in figure 7.15 by the shallow slope in comparison with the other calculation methods. Figure 7.16 shows that the regression line of the TTS $c = 0$ is close to the $x = y$ line. How ever the inclination of the TTS $c = 0$ is higher 1,8 than that of the TTS model 1,7.

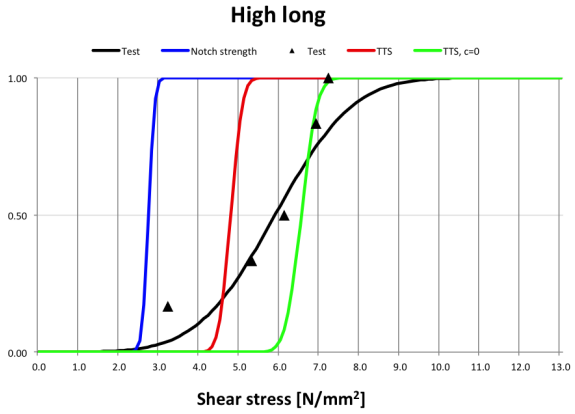

Figure 7.15: Tests results for the high long tenon beam

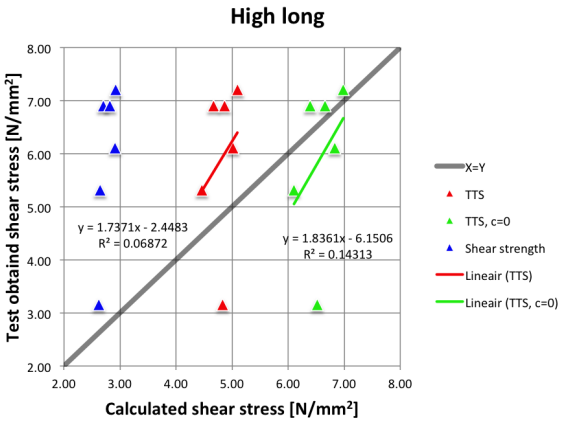

Figure 7.16: Calculated stress and fail stress comparison for the high long tenon beam

High short

The average of the tests from the high short set-up are very close to the average of the TTS $c = 0$ method. The COV of the test is bigger than all the calculated COV's this corresponds with the difference in the slopes in figure 7.17. Figure 7.18 shows that the calculations of TTS $c = 0$ is close to the $x = y$ line. The slopes of the regression lines of both models are negative and are fare away of the $x = y$ line.

7.4.2. Geometric combined compared theoretic tenon strength

In this paragraph all the set-ups are combined and matched in the four categories. This results in a combined data sets and new results. The results of combining and matching is shown in table 7.5.

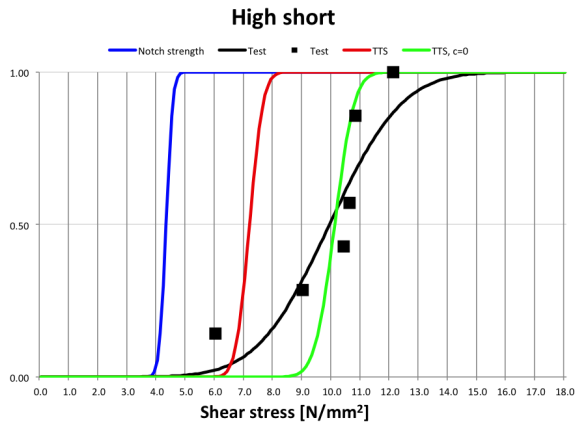

Figure 7.17: Tests results for the high short tenon beam

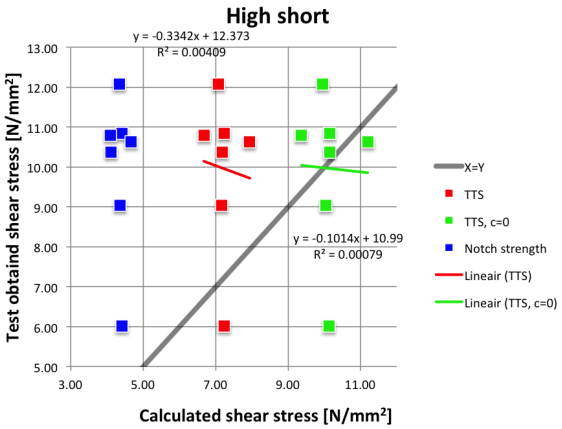

Figure 7.18: Calculated stress and fail stress comparison for the high short tenon beam

Table 7.5: Reduced shear stress failure of a azobé tenon beam $[N/mm^2]$ for the combined set-ups

		Short cantilever	Long cantilever	High tenon	Middle tenon
Tests	Average	11,0	7,2	8,1	10,4
	COV	0,20	0,26	0,33	0,23
	5^{th} percentile	7,4	4,1	3,7	6,4
TTS	Average	9,3	6,4	6,1	9,8
	COV	0,24	0,27	0,21	0,20
	5^{th} percentile	5,6	3,6	4,0	6,7
TTS $c = 0$	Average	12,9	8,9	8,5	13,6
	COV	0,24	0,28	0,22	0,19
	5^{th} percentile	7,9	4,8	5,4	9,4
Notch strength	Average	4,4	2,9	3,6	3,8
	COV	0,06	0,06	0,23	0,23
	5^{th} percentile	4,0	2,6	2,3	2,4

High tenon
The test results of the tenon located at the high location match close with the TTS $c = 0$ method for HS and HL. Figure 7.19 show that the long cantilevers match better with TTS $c = 0$ than the long cantilever in the test. The inclination of the regression line of the TTS $c = 0$ is 1.09 this is close to the 1,0 of the $x = y$ line. The regression line of the TTS method is steeper. All the COV's of the calculation methods are close to each other. The COV of the test is higher than the calculated COV's.

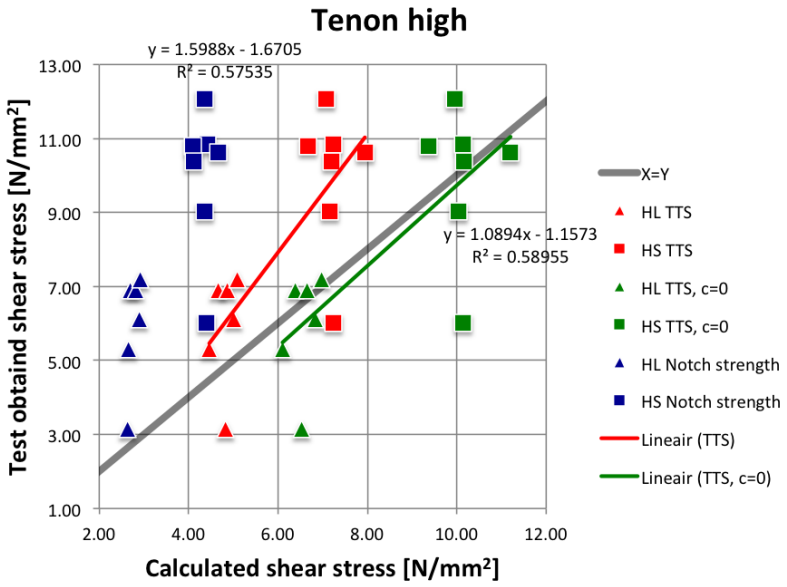

Figure 7.19: The high tenon locations combined in a calculated stress and fail stress comparison

Middle tenon
The found stresses in the tests are close to the TTS model, when the tenon is located in the middle of the beam for MS and ML. The average and 5^{th} percentile are close to the TTS method. The regression line in figure 7.20 shows that the inclinations of the TTS method is 0.94 this is close to inclination of the $x = y$ line. This is the regression line that is nearest tot the $x = y$ line of all set-ups and combined set-ups. All the COV's are close to each other.

Short cantilever
The tests of the short cantilevers MS and HS are between the TTS and TTS $c = 0$ method. The regression lines of figure 7.21 are not close to the $x = y$ line. The COV's of the TTS methods and the test results match better than the COV of the notch strength calculation. Figure 7.21 shows that HS $c = 0$ match better with the $x = y$ line. In paragraph 7.5. will be HS $c = 0$ and MS c calculated combined to compare the results.

Long cantilever
The found stresses by the test of the long cantilevers ML and HL are larger than the TTS method. In figure 7.22 is shown that the regression line is close to the $x = y$ line. The slope of the regression line for the TTS is 0.82 this is lower than the slope 1,00 of the $x = y$ line, but is closer than the TTS $c = 0$ regression line. The COV's of the TTS method match with the COV of the test results. Figure 7.22 shows that HL $c = 0$ match better with the $x = y$ line. In paragraph 7.5. will be HL $c = 0$ and ML c calculated be combined to compare the results

7.4.3. Total test results compared theoretic tenon strength
All the individual test set-ups are combined, this leads to the table 7.6.

Figure 7.23 shows that all the combined test results lead to an result in-between the TTS and TTS $c = 0$ methods. The lower found stresses are closer to the TTS method. When the stresses increase, they are going to the middle of both methods. The regression line of the TTS model in figure 7.23 is close to the $x = y$ line. The inclination of the TTS regression line is 0,84 this is more compared to the 0,61 for the TTS $c = 0$ method. The COV's of the TTS method match with the test results.

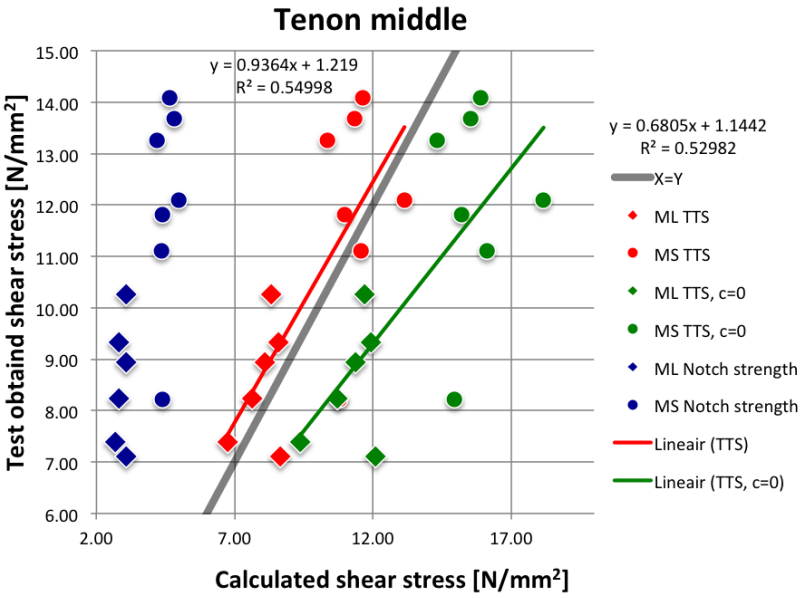

Figure 7.20: The middle tenon locations combined in a calculated stress and fail stress comparison

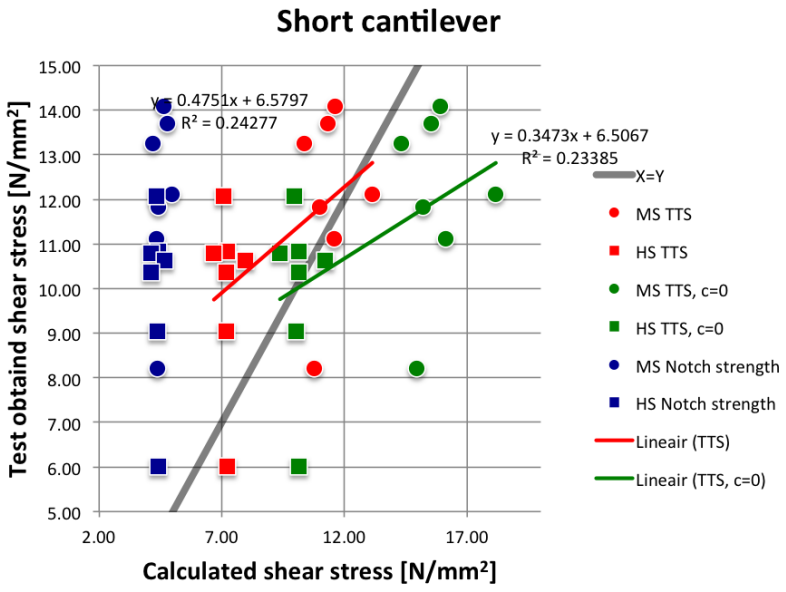

Figure 7.21: The short cantilevers combined in a calculated stress and fail stress comparison

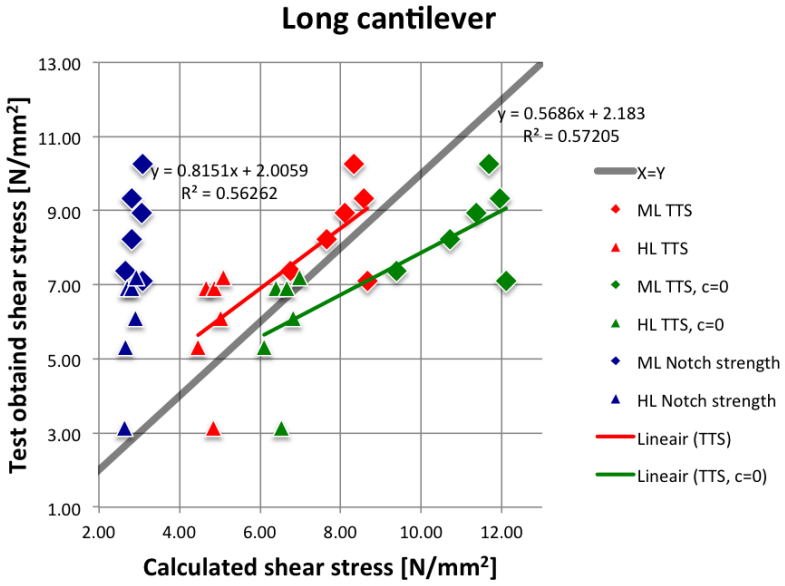

Figure 7.22: The long cantilevers combined in a calculated stress and fail stress comparison

Table 7.6: Reduced shear stress failure of a azobé tenon beam $[N/mm^2]$ for the total set-ups

		Total
Tests	Average	9,3
	COV	0,30
	5^{th} percentile	4,7
TTS	Average	8,0
	COV	0,31
	5^{th} percentile	3,9
TTS $c = 0$	Average	11,0
	COV	0,31
	5^{th} percentile	5,4
Notch strength	Average	3,7
	COV	0,23
	5^{th} percentile	2,3

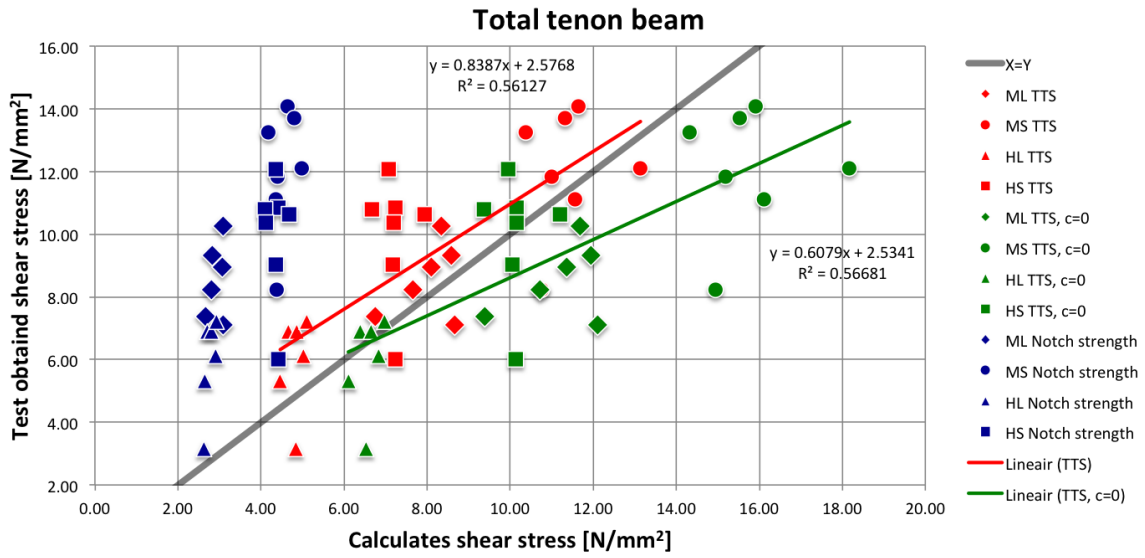

Figure 7.23: All combined in a calculated stress and fail stress comparison

7.5. The best calculation model combination

the previous paragraphs shown that the middle tenon geometry matches the best with the TTS method. The high geometry match with the TTS $c = 0$. Three graphs are replotted in this paragraph where the best calculation method is plotted for the geometry.

Short cantilever

Figure 7.24 shows that all the data points are close to the $x = y$ line. The regression line of the combined data has an inclination of 0,88 this closer to 1,00 than one of the inclinations of the separate models. Forcing the regression line through the origin will lead to the $x = y$ line.

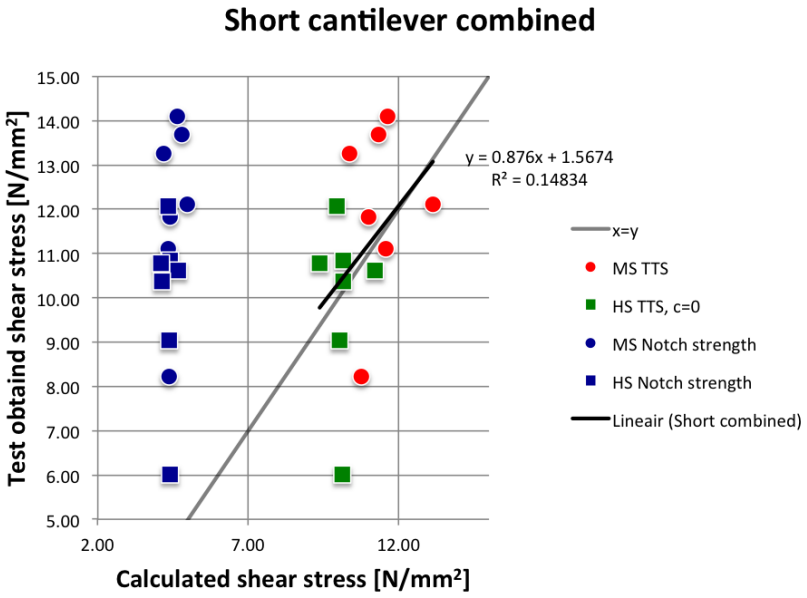

Figure 7.24: Combined short cantilevers in a calculated stress and fail stress comparison

Long cantilever

Figure 7.25 shows that all the data point are close to the $x = y$ line. The regression line of the combined data has an inclination of 1,50 this is further away to 1,00 than one of the inclinations of the separate models. But the regression line is closer to the $x = y$ line than the regression lines in figure 7.22. When the regression line in figure 7.25 is forced through the origin the line will be on top of $x = y$.

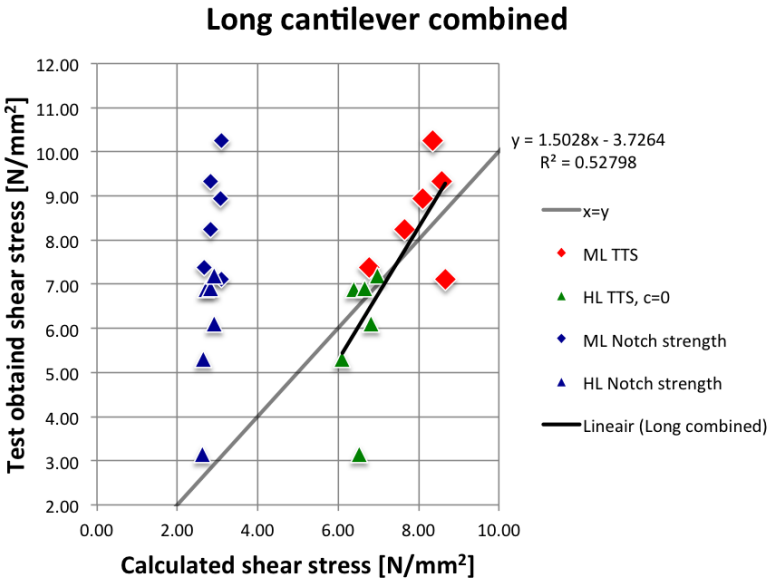

Figure 7.25: Combined long cantilevers in a calculated stress and fail stress comparison

Total
Combining the TTS methods for the middle tenon and the TTS $c = 0$ model for the high tenon, leads to data points close to the $x = y$ line as shown in figure 7.26. The formula given by this regression line $y = 1,0974x - 0,7947$, is the closest found formula to the $x = y$ line of al made combinations. Figures 7.26 shows that using TTS and the TTS $c = 0$ leads to good calculations for these set-ups.

7.6. Conclusions on the comparisons

Conclusions regarding Vermeij (2011)

- The stresses found in the tests of the spruce tenon beams come close to the theoretic tenon strength. The ratio for TTS / test results is 0,97. While the notch strength /test result is 0,40
- The theoretic tenon strength calculated with $G_{f,y}$ for azobé found by van Otterloo (2013), leads to better calculated tenon strength than when the $G_{f,y}$ of Larsen and Gustafsson (1992) is used.

Conclusions regarding van Otterloo (2013)

- The expression found trough the least square method for azobé for the fracture energy by van Otterloo (2013), $G_{f,y}[N/mm] = 5,364 \cdot 10^{-4} \rho[kg/m^3] + 4,150 \cdot 10^{-5} E_0[N/mm^2]$ is an improvement over the equation for European spruce and by Larsen and Gustafsson (1992), $G_{f,y} = -146 + 1,04\rho$.
- The ration TTS / test results for the MS, ML, HS and HL are respectively 0,95, 0,94, 0,73 and 0,81. TTS is an good approximation for MS and ML.
- The ration TTS $c = 0$ / test results for the MS, ML, HS and HL are respectively 1,31, 1,31, 1,02 and 1,11. TTS $c = 0$ is an good approximation for HS and HL.
- The test set-ups with the tenon located in the middle of the beam match close with the theoretic tenon strength, the slope of the found regression line is 0,94 close to 1,00.
- The test set-up with the tenon located high on the beam match close with the theoretic tenon strength with a rotational spring stiffness of $c = 0$, the slope of the found regression line is 1,09 close to 1,00.
- Combining the theoretic tenon strength of the middle set-up with the theoretic tenon strength $c = 0$ of the high set-up, lead to the best calculated theoretic tenon strengths.

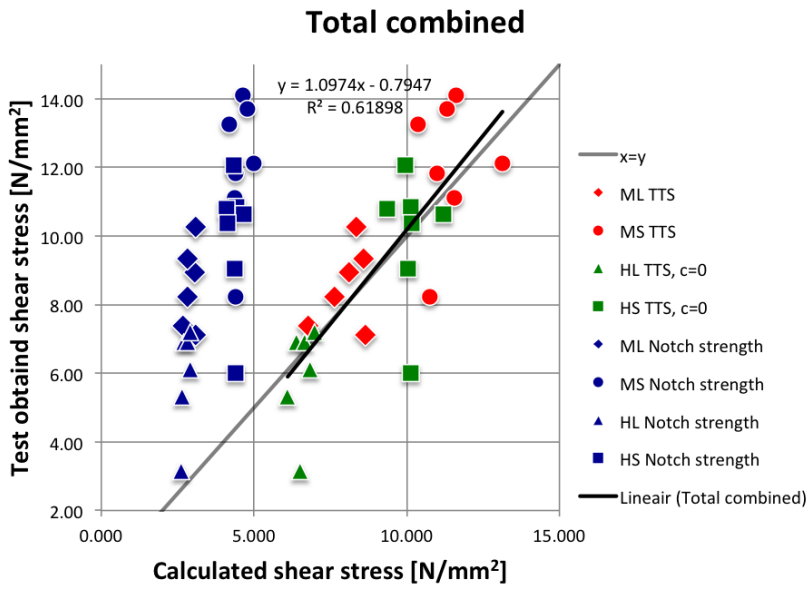

Figure 7.26: Total combined methods in a calculated stress and fail stress comparison

- The rotational spring stiffness of the tenon to beam interface is an important parameter in the tenon stiffness that is not understood.

There are remarks on the rotational spring stiffness c $[1/Nm]$. There is no mechanical of beam theory or research behind de values for c. That the middle tenon and the high tenon match with the two assumed c values is a stroke of luck. Why the middle tenon match with the c tenon value and why the high tenon match with the $c = 0$ remains unknown.

8

Conclusions and recommendations

The water pressure acts on the girder of the gate. Almost half of the force on the girder is transferred to the heel post, the other half to the mitre post. Due to the mitre a normal force in the girder is present. The normal force is dependent on the angle of the gate. With an increasing gate angle the normal force in the girder decreases. The biggest part of the normal force is transferred, via compression at the outside chest. Half of the shear force is transferred through the heel post. The mortise and tenon joint at the heel side transverse the shear stress through clamping of the tenon, shear stress through the seal strip support and through the 3D effect where the shear stress is transferred via the sides of the mortise. The other half of the force is transferred through the mitre post. The mortise and tenon joint in the mitre post transverse the shear stress through the 3D effect. The contact stresses along the length of the tenon are unevenly distributed. The contact stress along the width of the tenon are unevenly distributed and differ depending on the transfer mode. There is no existing verification for the mortise and tenon joint. The reduced shear strength for notch beams is used but is not sufficient for mt joints. This verification is too conservative when compared to the tests and not suitable for this case. In the next paragraphs a more detailed explanation is given on the stress distribution and the strength of the tenon.

8.1. Conclusions on the stress distribution

The stress distribution of the mortise and tenon joint is studied using a rough calculation and an elastic finite element model. The results of the models are verified by doing a force equilibrium calculation. The stress values in the conclusion do not include safety factors. The conclusions considering the stress distribution are:

- The biggest part of the stress transfers happens via contact pressure. The contribution of contact friction is small in comparison with the contact pressure.
- The contact pressures are unevenly distributed along the length and width of the tenon, this is shown in figure 8.1 for the heel joint and in figure 8.2 for the mortise joint.
- There are three different shear transverse modes in the joint: shear transfer through clamping, shear transfer through the seal strip support and shear transfer through the 3D effect. The 3D effect is that the shear stress is transferred via the sides of the mortise.
- The shear transfer through clamping occurs in the heel joint and in a small amount in the mitre joint, depending on the angle of the gate. The contact pressure due to clamping at the top of the tenon is evenly distributed over the width of the tenon. This clamping results in an tension stress behind the mortise.
- The shear transfer through the seal strip only occurs in the heel joint. There is no seal strip at the mitre joint. The seal strip result in a local increase of contact pressure at the bottom of the heel tenon. This pressure is evenly distributed over the width of the tenon.
- The shear transfer though the 3D effect occurs at the entrance of the mortise in both joints. A second area is present when clamping occurs, this is located more to the end of the mortise. The contact pressures depend on the location on the width of the tenon. On the edges of the tenon a higher pressure is present than in the middle of the tenon. This transfer mode results in tension stresses on the sides of mortise.
- The tension stress perpendicular to the fibre in the post at the entrance of the mortise for an gate angel of $18,5^\circ$ are around 4 N/mm^2 at the heel side and 5 N/mm^2 at the mitre side.
- The tension stress perpendicular to the fibre in the girder at the tenon pit for an gate angle of $18,5^\circ$ are around $1,6$ N/mm^2 at the heel side and 2 N/mm^2 at the mitre side.

- The heel joint and mitre joint transfer the shear stress different. The heel joint has all the three transfer modes, while the mitre joint has the 3D effect transfer and clamping only the gate is at a bigger angle.
- The difference between the heel and mitre joint results in different tenon moments resulting from the shear. In the heel joint the moment is twice the size of the moment at the mitre joint.
- The biggest part of the normal stress is transferred through the outside chests of the girder. The size of the normal stress is dependent on the angle of the gate. When the normal force is the biggest, at a small gate angle then stresses are present at the inside chest. When the normal force is small, at a big gate angle than there is no contact at the inside chest. The bolted steel connection in the gate can have an influence on the normal stress transfer, because its capability of transferring tension stresses. This connection can probably prevent opening of the joint and thus can probably maintain surface to surface contact at the inside chest.

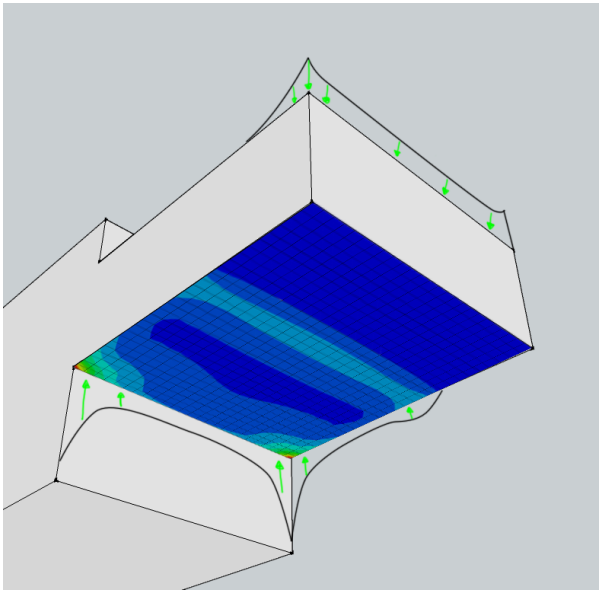

Figure 8.1: Contact pressure at the tenon at the heel post at a gate angle of 18,5° degrees

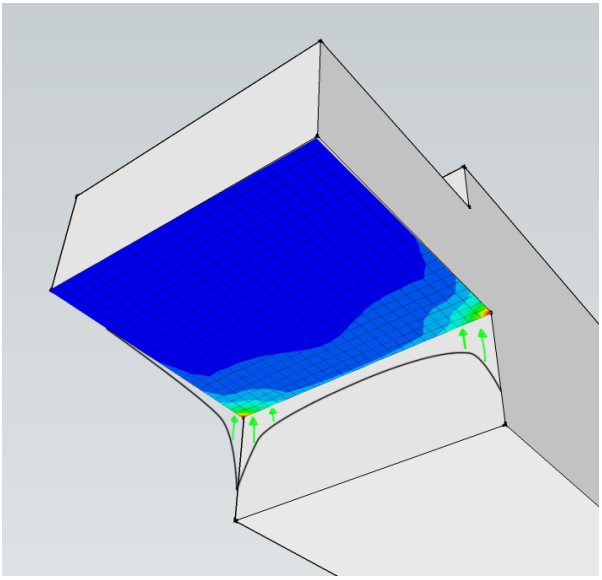

Figure 8.2: Contact pressure at the tenon at the mitre post at a gate angle of 18,5° degrees

8.2. Conclusions on the notch and tenon beam strength

This part contains the conclusions regarding the strength. The conclusions regarding the strength calculations in this paragraph are not valid for the mortise and tenon joint. All the strength calculations assume a point load at the cantilever, in previous paragraph 8.1. is concluded the stress at the tenon is unevenly distributed along the length and width of the cantilever as shown in the figures 8.1 and 8.2. The stress values in the conclusion do not include safety factors. The conclusions on the strength are written below.

The strength of the bolted steel strip and timber peg connections are studied for a constant stress distribution. In this study contact pressure is neglected, only failure of the connections is studied. The conclusions on the connections are:

- The bolted steel strip connection is able to transverse tension force at the heel side, while at the mortise side tension and compression forces are possible. The size of the strength can be calculated according Eurocode 5 pagagraph 8.2.2. The size of the strength of the bolted steel strip is so high that probably, it will contribute to the strength of the overall connection.
- The strength of the timber peg is low and is used for pre tensioning the mt joint in the construction. The size of the strength is so low, that it probably can contribute little to non to the complete connection.
- The strength for both the timber peg and bolted strip can be calculated for a constant stress distribution. The strength of the connections, when there is a no constant stress distribution is unknown.
- The contribution of both connection methods to the total strength of the mt joint remains unknown.

The strength calculation for the notch beam is explained and studied. This is done to see if this method is suitable for a tenon beam. The conclusions on the notch beam calculation are:

- The calculation method that today is used for a tenon beam is the reduced shear stress method in EC 5 for a notch beam.

- The reduced shear stress method in EC 5 for a notch beam is derived for a point load at the notch. This method is obtained trough linear crack growth using the displacement of the notch. The notch displacement contains three displacements: the bending displacement, the shear displacement and displacement due to a fictional rotational spring at the notch beam interface.
- The bending and shear displacements are obtained via a Euler beam and shear beam differential equation for a point load, with the geometry of a notch beam.
- Tests shown that fictional rotational spring stiffness it was not zero in a notch beam. Gustafsson (1988) obtained a fictional rotational spring stiffness mathematical, to make writing the equation simpler. The fictional rotational spring stiffness is $c = \frac{12}{b\alpha^2 d^2}\sqrt{\frac{(1-\alpha)(1-\alpha^3)}{10G_{xy}E_x}}$.
- The reduced shear stress method is suitable for European softwood beams, because this method uses the fracture energy of European softwoods. As the fracture energy of hardwood is unknown, this method not suitable for hardwoods.
- The reduced shear stress method for a notch beam is not suitable for a tenon beam due to the geometrical differences.

The derivation steps of the notch beam are used, to obtain a strength equation for a tenon beam. The conclusions regarding the tenon strength are:

- The theoretic tenon beam strength (TTS) is obtained using the same steps as for the strength of the notch beam. The difference is that the differential equations use 3 areas instead of 2 areas for a notch beam. This resulted in three transformation factors for the displacements, considering only the parts dependent on the location of the point force β. Multiplying the transformation factor to the notch displacement dependent of β will obtain the tenon displacement dependent on β. The shear transformation factor is $C_{v,t}$ shown in equations 8.1 and 8.2. The bending transformation factor is $C_{e,t}$ shown in equations 8.1 and 8.2. The rotation transformation factor is $C_{r,t} = \sqrt{C_{v,t}C_{e,t}}$.
- Two TTS equations are found, one with a mathematical obtained c equation 8.1 The other equation has a $c = 0$ this is equation 8.2

$$\begin{aligned}\frac{V_f}{b\alpha_1 d} &= \frac{\sqrt{\frac{G_{f,y}}{d}}}{\sqrt{\frac{0{,}6C_{v,t}\left(\alpha_1-\alpha_1^2\right)}{G_{xy}}}+\beta\sqrt{\frac{6C_{e,t}\left(\frac{1}{\alpha_1}-\alpha_1^2\right)}{E_x}}} \\ C_{v,t} &= \frac{(\alpha_1+\alpha_2-1)\alpha_1}{(\alpha_1+\alpha_2)(\alpha_1-1)} \\ C_{e,t} &= \frac{\left((\alpha_1+\alpha_2)^3-1\right)\alpha_1^3}{(\alpha_1+\alpha_2)^3\left(\alpha_1^3-1\right)}\end{aligned} \tag{8.1}$$

$$\begin{aligned}\frac{V_f}{b\alpha_1 d} &= \sqrt{\frac{5G_{f,y}}{3d\left(\frac{C_{v,t}\left(\alpha_1-\alpha_1^2\right)}{G_{xy}}+10\beta^2\frac{C_{e,t}\left(1/\alpha_1-\alpha_1^2\right)}{E_x}\right)}} \\ C_{v,t} &= \frac{(\alpha_1+\alpha_2-1)\alpha_1}{(\alpha_1+\alpha_2)(\alpha_1-1)} \\ C_{e,t} &= \frac{\left((\alpha_1+\alpha_2)^3-1\right)\alpha_1^3}{(\alpha_1+\alpha_2)^3\left(\alpha_1^3-1\right)}\end{aligned} \tag{8.2}$$

  where V_f $[N]$ is the shear force, $G_{x,y}$ $[N/mm]$ is the fracture energy in pure tensile splitting perpendicular to the fibre, G_{xy} $[N/mm^2]$ is he shear modulus, E_x $[N/mm^2]$ is the modulus of elasticity parallel to the grain b $[mm]$ is the width of the beam and d $[mm]$ the height of the beam. α_1 $[-]$, α_2 $[-]$ and β $[-]$ are shown in figure 8.3.
- The TTS average shear stress is $5,0$ N/mm^2 calculated by 8.1 with the tested spruce tenon beams, is close to the average found shear stress $5,1$ N/mm^2.
- The used fracture energy of hardwood equation 8.3 is obtained by van Otterloo (2013). This is an improvement over the equation used for softwoods.

$$G_{f,y} = 5.36\cdot 10^{-4}\rho + 4.15\cdot 10^{-5}E_x \tag{8.3}$$

  with ρ $[kg/m^3]$ and E_x $[N/mm^2]$ both obtained for individual test specimen.
- The TTS average shear stress is $9,8$ N/mm^2 calculated by 8.1 for the tested azobé tenon beams. With $\alpha_1 = \alpha_2 = 1/3$ for tenon height and location factor. The found average shear stress is $10,4$ N/mm^2.

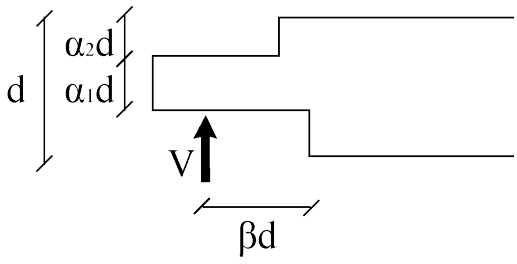

Figure 8.3: Geometric properties of a tenon beam

- The TTS with a fictional rotational spring stiffness of $c = 0$ 8.2 has the average calculated shear stress of $8,5\ N/mm^2$. The tested azobé tenon beams, have the tenon located at the $\alpha_2 = 1/5$ of the top of the beam. This tenon has a height of $\alpha_1 = 2/5$ of the girder height. The found average shear stress is $8,1\ N/mm^2$.
- The TTS equation 8.1 corresponds the best with $\alpha_1 = \alpha_2 = 1/3$ for the tenon height and location factor. The TTS $c = 0$ equation 8.1 corresponds the best with the $\alpha_1 = 2/5$ for the hight located at $\alpha_2 = 1/5$.

The problematic verification is the reduced shear strength method, this method attempts to calculate tension strength perpendicular to the fibre at the tenon pit. The in the FEM model maximum found tension stress perpendicular to the fibre is $5\ N/mm^2$. The tension strength perpendicular to the fibre for azobé is unknown, the strength of a hardwood species (American white oak) $5,5\ N/mm^2$ is assumed for azobé. Comparing the strength and the stress shows that this is presumable safe, this does not include any safety factors.

These conclusions and the conclusions of previous paragraphs indicate that it is a safe connection, even without completely understanding the mortise and tenon joint. These conclusions and the notion of no observed failure of mt joints, indicates that the centuries of lock gate building resulted in a presumable safe connection. The consequence of not completely understanding the joint, results in missing suitable verifications methods to quantify the safety. Quantifying the safety is only possible when the connection is more understood. More knowledge is needed, to get more understanding about this connection.

8.3. Recommendations

After doing this research a couple of recommendations are made regarding: additional research in the stress distribution and additional research in the strength of this joint.
Some recommendations considering the stress distribution are:

- A FEM model that includes the behaviour of the other connection methods (the timber peg and steel bolted strips) and uses the real support conditions will probably result in a more realistic stress distribution of the mt joint.
- A more realistic material model with the possibility of cracking and using plasticity, can be used for research on possible failure mechanisms.
- Differed load cases can be used to give a bigger knowledge on how the stress distribution in the mt joint occurs.
- Parametric research can be used to study the influence of different parameters, on how they influence the stress distribution.

Some recommendations considering the strength are:

- In the Eurocode 5 should be added that the existing equation for the reduced shear strength for a notched beams is only valid for softwoods. This equation should be expanded to include hardwoods.
- Large scale tests on the strength of softwood and hardwood notch and tenon beams should be performed. The tests in this thesis are small scale tests that can only be used as an indication on the strength. Final conclusions regarding the strength can only be made after large scale tests.
- Parametric research can be used, to study the influence of different parameters, on how they influence the strength of the tenon beam.
- A bigger understanding of the material is needed. An important material property to test for the mt joint will be the fracture energy. In this test different fracture modes should be considered like pure tensile splitting perpendicular to the fibre, pure parallel splitting to the fibre and possible combinations of both.

- A study in the transition conditions, between the beam and notch or tenon interface will be valuable. In this thesis the mathematical obtained rotational spring stiffness c obtained by Gustafsson (1988) is used. In this thesis a c value for a tenon beam is found following the same mathematical method. But the tests in this thesis have show that this c value is not right for all conditions. The c factor cannot be understood on the basis of the beam theory, and it is an important factor.

A

Notch and tenon differential equations

This appendix contains the differential equations. The four differential equations are: the notch beam shear displacement, the notch beam bending displacement, the tenon beam shear displacement and the tenon beam bending displacement. The used differential equation used for the shear beam is equation A.1. The used differential equation used for the bending beam is equation A.2.

$$GA\frac{d^2v}{dx^2} = 0 \tag{A.1}$$

$$EI\frac{d^4v}{dx^4} = 0 \tag{A.2}$$

The notch shear beam differential equations

Figure A.1 shows the notch beam with the coordinate system the force and the supports. The cross sections A that are used are: $A_1 = b\alpha d$ and $A_2 = bd$. The two differential equations are a result of substituted A_1 and A_2 in equation A.1. The boundary conditions that are used are shown in table A.1.

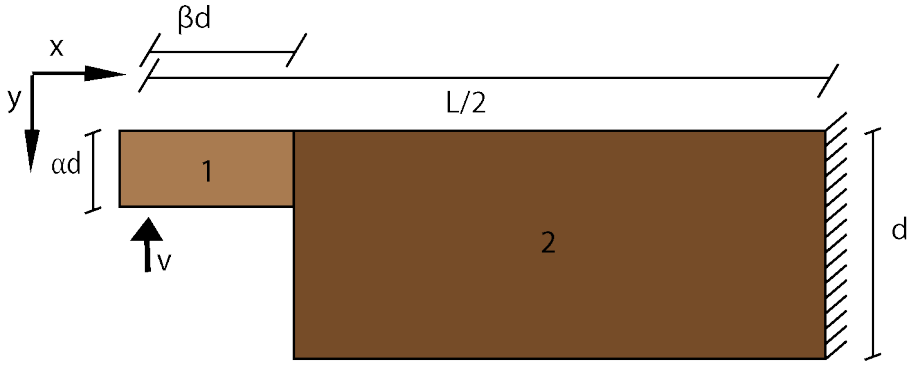

Figure A.1: The notch beam

Table A.1: Boundary conditions notch shear beam

$x = 0$	$x = \beta d$	$x = L/2$
$V_1 = -V$	$V_1 = V_2$	$v_2 = 0$
	$v_1 = v_2$	

The notch bending beam differential equations
Figure A.1 shows the notch beam with the coordinate system the force and the supports. The second moment of area I that are used are: $I_1 = b(\alpha d)^3/12$ and $I_2 = bd^3/12$. The two differential equations are a result of substituted I_1 and I_2 in equation A.2. The boundary conditions that are used are shown in table A.2.

Table A.2: Boundary conditions notch bending beam

$x = 0$	$x = \beta d$	$x = L/2$
$M_1 = 0$	$M_1 = M_2$	$\varphi_2 = 0$
$V_1 = -V$	$V_1 = V_2$	$\upsilon_2 = 0$
	$\varphi_1 = \varphi_2$	
	$\upsilon_1 = \upsilon_2$	

The tenon shear beam differential equations
Figure A.2 shows the notch beam with the coordinate system the force and the supports. The cross sections A that are used are: $A_1 = b\alpha_1 d$, $A_2 = b(\alpha_1 + \alpha_2)d$ and $A_3 = bd$. The three differential equations are a result of substituted A_1, A_2 and A_3 in equation A.1. The boundary conditions that are used are shown in table A.3.

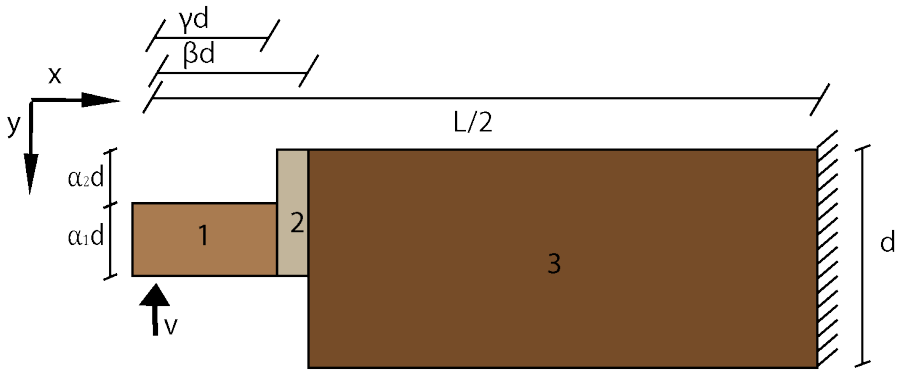

Figure A.2: The tenon beam

Table A.3: Boundary conditions tenon shear beam

$x = 0$	$x = \gamma d$	$x = \beta d$	$x = L/2$
$V_1 = -V$	$V_1 = V_2$	$V_2 = V_3$	$\upsilon_3 = 0$
	$\upsilon_1 = \upsilon_2$	$\upsilon_2 = \upsilon_3$	

The tenon bending beam differential equations
Figure A.2 shows the notch beam with the coordinate system the force and the supports. The second moment of areas I that are used are: $I_1 = b(\alpha_1 d)^3/12$ $I_2 = b(\alpha_1 + \alpha_2)^3/12$ and $I_3 = bd^3/12$. The three differential equations are a result of substituted I_1, I_2 and I_3 in equation A.2. The boundary conditions that are used are shown in table A.4.

Table A.4: Boundary conditions tenon bending beam

$x = 0$	$x = \gamma d$	$x = \beta d$	$x = L/2$
$M_1 = 0$	$M_1 = M_2$	$M_2 = M_3$	$\varphi_3 = 0$
$V_1 = -V$	$V_1 = V_2$	$V_2 = V_3$	$\upsilon_3 = 0$
	$\varphi_1 = \varphi_2$	$\varphi_2 = \varphi_3$	
	$\upsilon_1 = \upsilon_2$	$\upsilon_2 = \upsilon_3$	

B

Obtaining the shear strength of a tenon beam with c=0

In this appendix, the tenon beam stress with $c = 0$ is derived. The found total displacement equation B.1 is differentiated to β. The differentiation is shown in equation B.2. Substituting the differentiated equation B.2 in equation B.3 results in B.4.

$$\begin{aligned} \delta_{t,t} &= D\beta d + F\left(\beta d\right)^3 + constant \\ D &= \frac{1{,}2VC_{v,t}(1/\alpha_1 - 1)}{G_{xy}bd} \\ F &= \frac{12VC_{e,t}\left(1/\alpha^3 - 1\right)}{3E_x bd^3} \\ C_{v,t} &= \frac{(\alpha_1+\alpha_2-1)\alpha_1}{(\alpha_1+\alpha_2)(\alpha_1-1)} \\ C_{e,t} &= \frac{\left((\alpha_1+\alpha_2)^3-1\right)\alpha_1^3}{(\alpha_1+\alpha_2)^3\left(\alpha_1^3-1\right)} \end{aligned} \tag{B.1}$$

$$\frac{\Delta\left(\frac{\delta_{t,t}}{V}\right)}{\Delta\beta} = \frac{Db}{V} + \frac{3Fd^3\beta^2}{V} \tag{B.2}$$

$$\frac{V_f}{b\alpha d} = \sqrt{\frac{2G_c}{b\alpha^2 d} / \frac{\Delta\left(\frac{\delta_{t,t}}{V}\right)}{\Delta\beta}} \tag{B.3}$$

$$\frac{V_f}{b\alpha_1 d} = \sqrt{\frac{2G_c}{b\alpha_1^2 d \cdot \frac{1{,}2}{b}\left(\frac{C_{v,t}(1/\alpha_1 - 1)}{G_{xy}} + \beta^2 \frac{10C_{e,t}\left(1/\alpha_1^3 - 1\right)}{E_x}\right)}} \tag{B.4}$$

The final equation B.5 is obtained by cleaning up equation B.4 with B.6 and B.7.

$$\frac{V_f}{b\alpha_1 d} = \sqrt{\frac{5G_c}{3d\left(\frac{C_{v,t}\left(\alpha_1 - \alpha_1^2\right)}{G_{xy}} + \beta^2 \frac{10C_{e,t}\left(1/\alpha_1 - \alpha_1^2\right)}{E_x}\right)}} \tag{B.5}$$

$$C_{v,t} = \frac{(\alpha_1 + \alpha_2 - 1)\,\alpha_1}{(\alpha_1 + \alpha_2)\,(\alpha_1 - 1)} \tag{B.6}$$

$$C_{e,t} = \frac{\left((\alpha_1 + \alpha_2)^3 - 1\right)\alpha_1^3}{(\alpha_1 + \alpha_2)^3\left(\alpha_1^3 - 1\right)} \tag{B.7}$$

C

Tables of test data Vermeij and van Otterloo

The three tables in figures C.1, C.2 and C.3 show the used data from previous studies Vermeij (2011) and van Otterloo (2013). This data is used for the theory comparison in this thesis.

Test pieces	Width (mm)	Height (mm)	Specific weight (kg/m^3)	Dynamic MOE (N/mm^2)	Frac energy (Nmm/mm^2)	Shear modulus (N/mm^2)	Width tenon (mm)	Height tenon (mm)	Length tenon (mm)	Height lower notch (mm)	X test (mm)	Failure shear force (N)
VN1S_1	30	144	473.0	13600	0.35	850.00	30	48	80	48	40	6.81
VN2S_1	30	144	436.6	11500	0.31	718.75	30	48	80	48	40	4.47
VN3S_1	30	144	466.9	13900	0.34	868.75	30	48	80	48	40	4.16
VN4S_1	30	144	485.1	15300	0.36	956.25	30	48	80	48	40	5.24
VN5S_1	30	144	367.5	9500	0.24	593.75	30	48	80	48	40	3.84
VN6S_1	30	144	466.2	14500	0.34	906.25	30	48	80	48	40	3.92
VN1S_2	30	144	473.0	13600	0.35	850.00	30	48	80	48	40	5.40
VN2S_2	30	144	436.6	11500	0.31	718.75	30	48	80	48	40	6.06
VN3S_2	30	144	466.9	13900	0.34	868.75	30	48	80	48	40	4.39
VN4S_2	30	144	485.1	15300	0.36	956.25	30	48	80	48	40	5.29
VN5S_2	30	144	367.5	9500	0.24	593.75	30	48	80	48	40	3.72
VN6S_2	30	144	466.2	14500	0.34	906.25	30	48	80	48	40	5.88

Test pieces	Width (mm)	Height (mm)	Specific weight (kg/m^3)	Dynamic MOE (N/mm^2)	Frac energy (Nmm/mm^2)	Shear modulus (N/mm^2)	Width tenon (mm)	Height tenon (mm)	Length tenon (mm)	Height lower notch (mm)	X test (mm)	Failure shear force (N)
AN1S_1	30	144	1006.7	17300	1.26	1081.25	30	48	80	48	40	9.75
AN2S_1	30	144	1008.6	17900	1.28	1118.75	30	48	80	48	40	13.16
AN3S_1	30	144	1010.9	18800	1.32	1175.00	30	48	80	48	40	10.37
AN4S_1	30	144	1097.9	19300	1.39	1206.25	30	48	80	48	40	16.90
AN5S_1	30	144	1009.7	17600	1.27	1100.00	30	48	80	48	40	18.73
AN6S_1	30	144	1014.5	17500	1.27	1093.75	30	48	80	48	40	13.70
AN1S_2	30	144	1006.7	17300	1.26	1081.25	30	48	80	48	40	22.85
AN2S_2	30	144	1008.6	17900	1.28	1118.75	30	48	80	48	40	21.19
AN3S_2	30	144	1010.9	18800	1.32	1175.00	30	48	80	48	40	25.77
AN4S_2	30	144	1097.9	19300	1.39	1206.25	30	48	80	48	40	19.38
AN5S_2	30	144	1009.7	17600	1.27	1100.00	30	48	80	48	40	17.56
AN6S_2	30	144	1014.5	17500	1.27	1093.75	30	48	80	48	40	16.50

Figure C.1: Test data Vermeij (2011)

Test pieces Middle Long	Width (mm)	Height (mm)	Specif weight (kg/m^3)	Dynami c MOE (N/mm ^2)	Frac energy (Nmm/ mm^2)	Gxy (N/mm ^2)	Width tenon (mm)	Height tenon (mm)	Length tenon (mm)	Height lower notch (mm)	X test (mm)	a1 (mm)	b +a2 (mm)	a (mm)	b (mm)	Fjack (N)
A1-1	27	146	1023	19495	1.36	1218	27	51	150	47	58	148	333	423	58	48.25
A2-1	26	146	1074	19036	1.37	1190	26	50	150	47	50	148	333	431	50	79.27
A2-3	25	147	1074	18939	1.36	1184	25	51	151	47	56	149	333	426	56	64.31
A3-1	26	148	1033	20196	1.39	1262	26	52	151	49	51	149	333	431	51	77.62
A4-1	25	146	1033	17821	1.29	1114	25	51	150	47	55	149	333	427	55	70.64
A5-1	25	145	1072	22256	1.50	1391	25	48	149	47	55	149	333	427	55	61.68
A6-1	27	139	1084	19129	1.38	1196	27	42	150	50	55	149	333	427	55	53.30
Test pieces Middle Long	Width (mm)	Height (mm)	Specif weight (kg/m^3)	Dynami c MOE (N/mm ^2)	Frac energy (Nmm/ mm^2)	Gxy (N/mm ^2)	Width tenon (mm)	Height tenon (mm)	Length tenon (mm)	Height lower notch (mm)	X test (mm)	a1 (mm)	b +a2 (mm)	a (mm)	b (mm)	Fjack (N)
A1-2	25	147	1023	19055	1.34	1191	25	50	150	52	124	148	395	419	124	44.97
A2-2	25	147	1074	20086	1.41	1255	25	51	150	48	111	148	395	433	111	55.57
A2-4	21	147	1074	20680	1.43	1293	21	51	150	47	113	148	395	430	113	53.84
A4-2	25	145	1033	18500	1.32	1156	25	50	150	47	112	148	395	432	112	50.38
A5-2	25	143	1072	21261	1.46	1329	25	48	150	47	114	148	395	430	114	41.32
A6-2	22	138	1084	19825	1.40	1239	22	42	150	47	114	148	395	429	114	42.47

Figure C.2: Test data of the middle set-ups van Otterloo (2013)

Test pieces Middle Long	Width (mm)	Height (mm)	Specif weight (kg/m^3)	Dynami c MOE (N/mm ^2)	Frac energy (Nmm/ mm^2)	Gxy (N/mm ^2)	Width tenon (mm)	Height tenon (mm)	Length tenon (mm)	Height lower notch (mm)	X test (mm)	a1 (mm)	b +a2 (mm)	a (mm)	b (mm)	Fjack (N)
A1-1	27	146	1023	19495	1.36	1218	27	51	150	47	58	148	333	423	58	48.25
A2-1	26	146	1074	19036	1.37	1190	26	50	150	47	50	148	333	431	50	79.27
A2-3	25	147	1074	18939	1.36	1184	25	51	151	47	56	149	333	426	56	64.31
A3-1	26	148	1033	20196	1.39	1262	26	52	151	49	51	149	333	431	51	77.62
A4-1	25	146	1033	17821	1.29	1114	25	51	150	47	55	149	333	427	55	70.64
A5-1	25	145	1072	22256	1.50	1391	25	48	149	47	55	149	333	427	55	61.68
A6-1	27	139	1084	19129	1.38	1196	27	42	150	50	55	149	333	427	55	53.30

Test pieces Middle Long	Width (mm)	Height (mm)	Specif weight (kg/m^3)	Dynami c MOE (N/mm ^2)	Frac energy (Nmm/ mm^2)	Gxy (N/mm ^2)	Width tenon (mm)	Height tenon (mm)	Length tenon (mm)	Height lower notch (mm)	X test (mm)	a1 (mm)	b +a2 (mm)	a (mm)	b (mm)	Fjack (N)
A1-2	25	147	1023	19055	1.34	1191	25	50	150	52	124	148	395	419	124	44.97
A2-2	25	147	1074	20086	1.41	1255	25	51	150	48	111	148	395	433	111	55.57
A2-4	21	147	1074	20680	1.43	1293	21	51	150	47	113	148	395	430	113	53.84
A4-2	25	145	1033	18500	1.32	1156	25	50	150	47	112	148	395	432	112	50.38
A5-2	25	143	1072	21261	1.46	1329	25	48	150	47	114	148	395	430	114	41.32
A6-2	22	138	1084	19825	1.40	1239	22	42	150	47	114	148	395	429	114	42.47

Figure C.3: Test data of the high set-ups van Otterloo (2013)

Bibliography

[1] Picture of jones falls locks. `https://commons.wikimedia.org/wiki/File:Jones_Falls_Locks.jpg`. Accessed: 26-05-2017.

[2] NEN-EN 14081-1. *Timber structures - Strength graded structural timber with rectangular cross section - Part 1: General requirements*, 2016.

[3] NEN-EN 1995-1-1. *Eurocode 5 - Design of timber structures - Part 1-1: General - Common rules and rules for buildings*, 2005.

[4] NEN-EN 338. *Structural timber - Strength classes*, 2016.

[5] NEN-EN 384. *Structural timber - Determination of characteristic values of mechanical properties and density*, 2016.

[6] NEN-EN 408. *Structural Timber- Structural Timber and Glued Laminated Timber- Determination of some physical and mechanical properties.*, 2012.

[7] H.J. Blaß, R. Görlacher, and al. Rolling shear in structural bonded timber elements. In *Annales GC Bois*, volume 5, pages 1–5. IRABOIS, 2000.

[8] L Da Vinci. Codex atlanticus. folio 656 a. Drawing from: "Il Codice Atlantico di Leonardo da Vinci nella biblioteca Ambrosiana di Milano, Editore Milano Hoepli 1894-1904'.

[9] J. Ehlbeck and M. Kromer. Carpentry joints. *H. Blass, P., Aune, BS, Choo, R. Görlacher, DR, Griffiths, BO Hilson, et al.(Eds.), Timber Engineering-STEP*, 1:7, 1995.

[10] P.J. Gustafsson. A study of strength of notched beams. *Proc. of CIB-W18 Paper*, pages 21–10, 1988.

[11] P.J. Gustafsson and B. Enquist. Träbalks hållfasthet vid rätvinklig urtagning (timber beam strenght with right angles resesses). Technical report, 1988.

[12] J.P. Judd, F.S. Fonseca, C.R. Walker, and P.R. Thorley. Tensile strength of varied-angle mortise and tenon connections in timber frames. *Journal of Structural Engineering*, 138(5):636–644, 2011.

[13] H.J. Larsen and P.J. Gustafsson. The fracture energy of wood in tension perpendicular to the grain: Results from a joint testing project. *International Council for Research and Innovation in Building and Construction, Working Commission CIB-W18*, 1990.

[14] H.J. Larsen, H. Riberholt, and P.J. Gustafsson. Annex to paper cib-w18/25-102-1—eurocode 5-design of notched beams. In *Meeting of the International Council for Building Research Studies and Documentation Working Commission W*, volume 18, 1992.

[15] W.M. McKenzie and H. Karpovich. The frictional behaviour of wood. *Wood science and technology*, 2(2):139–152, 1968.

[16] Drs. P and M. Kool. *Wis en natuur lyriek met chemisch supplement.* Nijgh & Van Ditmar, 2000.

[17] D. Porter. *The Civil Engineering of Canals and Railways before 1850 Mike Chrimes.* Ashgate Publishing, 2000.

[18] G. Ravenshorst, N. Gamper, P. De Vries, and J.W.G. Van de Kuilen. Determination of the shear strength of tropical hardwood timber. In *World Conference on Timber Engineering*, pages 677–684, 2016.

[19] C. Sandhaas. *Mechanical behaviour of timber joints with slotted-in steel plates.* PhD thesis, TU Delft, 2012.

[20] I. Smith and G. Springer. Consideration of gustafsson's proposed eurocode 5 failure criterion for notched timber beams. *Canadian Journal of Civil Engineering*, 20(6):1030–1036, 1993.

[21] S. Stevin. *Nieuwe maniere van sterctebou, door spilsluysen*, volume 1. by Bonaventuer ende Abraham Elzevier, 1617.

[22] Forest Products Laboratory (US). *Wood handbook: wood as an engineering material.* Number 72. United States Government Printing, centennial edition edition, 2010.

[23] J.W.G. Van de Kuilen and H.J. Blass. Mechanical properties of azobé (lophira alata). *Holz als Roh-und Werkstoff*, 63 (1):1–10, 2005.

[24] J.W.G. Van de Kuilen and A. Leijten. Schuifsterkte bepaling van zeven houtsoorten voor de toepassing in verkeersbruggen. Technical report, Report 2001-4/HE43. Delft University of Technology, 2002.

[25] B. Van Leusen. *Duikers en sluizen*. Stam Techniek, Culemborg, the Netherlands, 1989.

[26] J.R. Van Otterloo. Force distribution and connection strength in timber lock gates. Master's thesis, TU Delft, Delft University of Technology, 2013.

[27] D.A.A.N. Vermeij. Pen gat verbinding (mortis and tenon joint). Master's thesis, TU Delft, 2011.

[28] A. Vierlingh, J. de Hullu, and A.G. Verhoeven. *Tractaet van dyckagie*. Nijhoff, 1920.